Talita de Sousa Laurentino

Análise do papel funcional de LOXL3 em glioblastoma

São Paulo

2023

Talita de Sousa Laurentino

Análise do papel funcional de LOXL3 em glioblastoma

Tese apresentada à Faculdade de Medicina da Universidade de São Paulo para obtenção do título de Doutor em Ciências

Programa de Neurologia
Orientadora: Dra. Sueli Mieko Oba Shinjo

São Paulo

2023

Dados Internacionais de Catalogação na Publicação (CIP)

Preparada pela Biblioteca da
Faculdade de Medicina da Universidade de São Paulo

©reprodução autorizada pelo autor

Laurentino, Talita de Sousa
Análise do papel funcional de LOXL3 em glioblastoma / Talita de Sousa Laurentino. -- São Paulo, 2023.
Tese(doutorado)--Faculdade de Medicina da Universidade de São Paulo.
Programa de Neurologia.
Orientadora: Sueli Mieko Oba Shinjo.

Descritores: 1.Glioblastoma 2.Astrocitoma 3. Lisil oxidase tipo 3 4.Proliferação celular 5.Morte celular 6.Ciclo celular 7.Senescência 8.Matriz extracelular 9.Tubulina 10.Microtúbulo

USP/FM/DBD-513/23

Responsável: Erinalva da Conceição Batista, CRB-8 6755

Dedicatória

Dedico essa tese ao meu Deus, meu quase marido Otavio Henrique e a minha família.
Muitíssimo obrigada! Sem vocês eu não teria chegado até aqui.

AGRADECIMENTOS

Chegou o final de uma parte muito importante da minha vida. E nessa caminhada, de vários altos e baixos, grandes conquistas, ganhei muitas amizades, e tive o apoio de pessoas que se tornaram essenciais para que eu pudesse chegar até aqui.

Primeiramente, e mais importante, gostaria de glorificar, e honrar ao meu Deus! Tudo é dEle, para Ele, por Ele! Sem o auxílio do meu conselheiro, Espirito Santo, não seria possível suportar o processo, cair e levantar, não seria o que sou hoje, portanto, toda honra e glória ao meu Senhor Jesus.

Agradeço ao meu quase marido Otavio, por todo cuidado, mão estendida, e por me incentivar a prosseguir tentando quando as coisas não saiam como esperado. Agradeço por meu ouvir com entusiasmo sobre o LOXL3 (acho que você já pode responder algumas perguntas por mim!). Agradeço, de verdade, por não ter deixado eu desistir, quando eu achava que esse negócio de ciência não era pra mim!

A minha família por todo amor e apoio durante essa jornada. Por comemorar comigo as minhas conquistas e me ajudar nas minhas dificuldades. Agradeço a minha irmã Jennifer por também por me ouvir falar sobre LOXL3, e por sem saber, me estimular e me incentivar através de suas palavras de admiração. Agradeço a minha mãe por toda preocupação e compreensão nos momentos mais complicados.

Agradeço a Dra. Sueli Oba que me confiou este trabalho. Agradeço por todo apoio, e incentivo a continuar sempre tentando. Com sua tranquilidade e força, pude aprender a lidar com as pressões que a vida traz. Agradeço por compartilhar comigo um pouco desse enorme e doce coração. Agradeço todo apoio e toda ajuda que me ofereceu.

Agradeço a Prof. Dra. Suely Marie, que também abriu as portas do seu laboratório para que pudesse aprender um pouco a fazer ciência. Agradeço pelas perguntas certeiras, e por estimular os seus alunos na construção de um raciocínio linear.

Agradeço a Dra. Roseli, que desde o mestrado, se mostrou uma grande amiga, e que com certeza quero levá-la pra minha vida. Agradeço por não ter medido esforços para me passar os seus conhecimentos, e por sempre estar por perto, e me ajudar quando precisava. Você é uma amiga que quero levar pra vida! Agradeço pelos conselhos certeiros sobre ciência e sobre a vida. E claro, agradeço pelo LOXL3!

Agradeço a todas as meninas do LIM15 com quem pude compartilhar cada dia. Com elas, longos dias puderam ser transformados em lembranças de altos papos e grandes risadas. Agradeço a Isabele, por toda ajuda e por toda paciência com as dúvidas em matemática. Dali, por dançar e cantar comigo. A Stella, por me acompanhar todos os dias no bandejão, e por nossas conversas sobre o nosso Deus. A Paula, por toda ajuda e pelos puxões de orelha. A Chris, por todo auxilio, mesmo que por pouco tempo.

Agradeço a Dra Kátia Carvalho, pelo carinho, pela risada leve, por me emprestar tantas coisas, sem a sua ajuda, esse trabalho, teria sido mais difícil!

Agradeço aos funcionários Luiz, Rosa, Nice, Camila, Mônica, Thais, e Eliene por toda ajuda no laboratório.

Agradeço ao Ricardo Cintra por me ajudar com a construção do sistema CRISPR-Cas9.

Agradeço ao Dr Antônio Marcondes Lerário, da Universidade de Michigan, pelas análises do transcriptoma.

Agradeço ao LIM60, pelo auxílio na citometria de fluxo.

Agradeço ao LIM50, pela utilização do equipamento de leitura de fluorescência.

Agradeço ao CEFAP e ao INFAR pelo auxílio com o Confocal. Ao CTO do ICESP, e ao LIM 58 por permitir o uso do revelador de Western Blot.

Agradeço ao SELA pela utilização dos equipamentos de sequenciamento e análise de qualidade de RNA.

Agradeço a todos que cooperaram para realização desse trabalho.

Agradeço a Fundação de Amparo à Pesquisa do Estado de São Paulo (Processo 2021/01207-4, bolsa de doutorado) por fomentar este trabalho.

RESUMO

Laurentino TS. Análise do papel funcional de LOXL3 em glioblastoma [tese]. São Paulo: Faculdade de Medicina, Universidade de São Paulo; 2023.

Os astrocitomas, são tumores que se originam das células astrocíticas do sistema nervoso central. Os astrocitomas foram classificados pela Organização Mundial da Saúde com base na malignidade, considerando características histológicas. Recentemente, essa classificação foi incluiu características moleculares, como mutações e outras alterações cromossômicas. O glioblastoma (GBM), categorizado como grau 4 entre os astrocitomas difusos e caracterizado por IDH selvagem, é o glioma mais prevalente e apresenta o prognóstico mais desfavorável. Com o intuito compreender os processos de gliomagênese, nosso laboratório realizou uma comparação dos genes mais expressos no GBM em relação ao astrocitoma grau 1, visando potenciais alvos terapêuticos. O gene responsável pela codificação da enzima lisil oxidase (LOX) foi identificado com uma expressão elevada no GBM. Esta enzima faz parte de uma família composta por cinco membros - LOX, LOXL1, LOXL2, LOXL3 e LOXL4 - desempenhando um papel crucial na catalisação das ligações cruzadas do colágeno e da elastina. Sua atuação é essencial para conferir rigidez à matriz extracelular (MEC). Neste presente estudo, foram realizadas análises para compreender melhor o papel de LOXL3 em astrocitomas. Análises *in silico* mostraram que *LOXL3* é altamente expresso em GBM, com maior expressão no subtipo molecular de pior prognóstico, o mesenquimal. Além disso, a expressão de *LOXL3* influenciou no prognóstico dos pacientes com GBM. Pacientes com maior expressão de *LOXL3* apresentaram menor sobrevida do que àqueles com menor expressão do gene. O silenciamento transitório de *LOXL3* na linhagem celular de GBM humano U87MG levou a uma diminuição da proliferação, adesão e invasão celular, e um aumento de apoptose e da superfície celular. Análises de transcriptoma mostraram um aumento da expressão de genes que codificam proteínas relacionadas a MEC, adesão celular, e componentes do citoesqueleto. Análises *in sílico* no banco de dados do TCGA mostraram correlação dos níveis de expressão de *LOXL3* e de genes que codificam tubulinas no subtipo mesenquimal. A expressão dos genes da família LOX aumenta de acordo com malignidade dos astrocitomas. Com base na influência de LOXL3 na estabilidade da MEC, foram realizadas análises *in silico* em banco de dados públicos para avaliar a correlação dos genes da família LOX e os que codificam componentes da MEC nos astrocitomas diferentes graus de malignidade e com e sem mutação de *IDH*. Foi observado um aumento progressivo na expressão dos cinco membros da família LOX conforme o aumenta o grau de malignidade. Os níveis de expressão de *LOX*, *LOXL1* e *LOXL3* correlacionaram-se positivamente com os de genes do matrissoma. Foram observadas correlações específicas, como *LOXL1* em gliomas de baixo grau (LGG) com mutação no IDH (IDH^{mut}), *LOXL3* em LGG com tipo selvagem de IDH (IDH^{wt}) e forte correlação de LOX em GBM. Essas associações podem explicar o aumento na rigidez da MEC e na agressividade tumoral de LGG-IDH^{mut} para LGG-IDH^{wt} até GBM. Além disso, a expressão do fator de transcrição sensível à mecanotransdução, β-catenina, aumentou com o grau de malignidade e correlacionou-se com *LOXL1* e *LOXL3*, sugerindo seu envolvimento na via de sinalização. Para dar continuidade a análises do papel

funcional de LOXL3 em GBMs, foi realizado um nocaute gênico através do sistema de CRISPR-Cas9 nas linhagens celulares de GBM humano, U87MG e U251. A análise do transcriptoma mostrou uma diminuição de expressão de genes relacionados à acetilação da tubulina nas células U87MG, confirmada por Western blot, corroborando com as correlações observadas anteriormente em análises *in silico*. Além disso, observou-se uma redução de expressão de genes ligados ao ciclo celular em ambas as linhagens celulares. Também foram observados através de ensaios funcionais atraso na progressão do ciclo celular e alterações marcantes no fuso mitótico durante as fases de metáfase-anáfase. A análise da morfologia nuclear indicou alterações associadas à catástrofe mitótica em células U87MG e à senescência em células U251. Corroborando com dados obtidos anteriormente, observou-se uma diminuição nos processos de adesão e migração celular nas células nocauteados para *LOXL3*. A análise do banco de dados do TCGA revelou uma correlação entre a expressão do *LOXL3* e genes relacionados ao ciclo celular, morte celular e senescência em casos GBM com *TP53* mutado. Além disto, observou-se que a coexpressão de *LOXL3* e *CCNE1* impactou a sobrevivência de pacientes com GBM com mutação no *TP53*, sugerindo um potencial alvo terapêutico combinado para casos de GBM com essa mutação. Esses dados corroboram para descrever o papel funcional de LOXL3 em GBM envolvendo a organização do citoesqueleto, principalmente relacionado a tubulina e microtúbulos. Ainda, LOXL3 está relacionado a processos como invasão tumoral e rigidez da MEC. Esses resultados sugerem a relevância de LOXL3 nos astrocitomas, reforçando que pode ser um potencial alvo terapêutico.

Palavras-chave: Glioblastoma. Astrocitoma. Lisil oxidase tipo 3. Proliferação celular. Morte celular. Ciclo celular. Senescência. Matriz extracelular. Tubulina. Microtúbulo

ABSTRACT

Laurentino TS. The functional role of LOXL3 in glioblastoma [thesis]. São Paulo: “Faculdade de Medicina, Universidade de São Paulo”; 2023.

Astrocytomas are tumors originating from the astrocytic cells of the central nervous system. The World Health Organization has classified astrocytomas based on malignancy, considering histological characteristics. Recently, this classification has incorporated molecular features such as mutations and chromosomal alterations. Glioblastoma (GBM), categorized as grade 4 among diffuse astrocytomas and characterized by wild-type IDH, is the most prevalent glioma with the poorest prognosis. In order to understand gliomagenesis processes, our laboratory compared the most expressed genes in GBM to grade 1 astrocytoma, aiming to identify potential therapeutic targets. The gene encoding the lysyl oxidase enzyme (LOX) was identified with elevated expression in GBM. This enzyme, part of a family of five members—LOX, LOXL1, LOXL2, LOXL3, and LOXL4—plays a crucial role in catalyzing collagen and elastin cross-linking, essential for conferring stiffness to the extracellular matrix (ECM). In this study, analyses were conducted to better understand the role of LOXL3 in astrocytomas. In silico analyses showed that LOXL3 is highly expressed in GBM, with higher expression in the mesenchymal molecular subtype associated with worse prognosis. Furthermore, LOXL3 expression influenced the prognosis of GBM patients, with higher LOXL3 expression correlating with reduced survival. Transient silencing of LOXL3 in the human GBM cell line U87MG resulted in decreased cell proliferation, adhesion, and invasion, increased apoptosis, and altered cell surface characteristics. Transcriptome analyses revealed increased expression of genes encoding ECM-related proteins, cell adhesion, and cytoskeletal components. In silico analyses using TCGA database showed a correlation between LOXL3 expression and tubulin-encoding genes in the mesenchymal subtype. The expression of LOX family genes increased with astrocytoma malignancy. Based on LOXL3's influence on ECM stability, in silico analyses were performed on public databases to assess the correlation between LOX family genes and those encoding ECM components in astrocytomas of different malignancy grades and with or without IDH mutation. A progressive increase in the expression of all five LOX family members was observed with increasing malignancy grade. LOX, LOXL1, and LOXL3 expression positively correlated with matrisome genes. Specific correlations were noted, such as LOXL1 in low-grade gliomas (LGG) with IDH mutation (IDHmut), LOXL3 in LGG with wild-type IDH (IDHwt), and a strong correlation of LOX in GBM. These associations may explain the increased ECM stiffness and tumor aggressiveness from LGG-IDHmut to LGG-IDHwt to GBM. Additionally, the expression of the mechanotransduction-sensitive transcription factor β-catenin increased with malignancy grade and correlated with LOXL1 and LOXL3, suggesting its involvement in signaling pathways. To further analyze the functional role of LOXL3 in GBMs, CRISPR-Cas9 gene knockout was performed in the human GBM cell lines U87MG and U251. Transcriptome analysis revealed a decrease in tubulin acetylation-related gene expression in U87MG cells, confirmed by Western blot, supporting previous in silico correlations. Moreover, a reduction in the expression of cell cycle-related genes was observed in both cell lines. Functional assays demonstrated delayed

cell cycle progression and significant alterations in the mitotic spindle during metaphase-anaphase phases. Nuclear morphology analysis indicated changes associated with mitotic catastrophe in U87MG cells and senescence in U251 cells. Consistent with previous data, knockdown of LOXL3 resulted in decreased cell adhesion and migration processes. TCGA database analysis revealed a correlation between LOXL3 expression and genes related to cell cycle, cell death, and senescence in GBM cases with mutated TP53. Furthermore, coexpression of LOXL3 and CCNE1 impacted the survival of GBM patients with TP53 mutation, suggesting a potential combined therapeutic target for such cases. These findings contribute to describing the functional role of LOXL3 in GBM, involving cytoskeleton organization, particularly related to tubulin and microtubules. Additionally, LOXL3 is associated with processes such as tumor invasion and ECM stiffness. These results suggest the relevance of LOXL3 in astrocytomas, emphasizing its potential as a therapeutic target.

Keywords: Glioblastoma. Astrocytoma. Lysyl oxidase like 3. Cell proliferation. Cell death. Cell cycle. Senescence. Extracellular matrix. Tubulin. Microtubule.

SUMÁRIO

Introdução

LOXL3 e astrocitomas

1 INTRODUÇÃO

1.1. LOXL3

Lisil oxidase 3 (LOXL3) é uma amino oxidase que pertence a uma família denominada lisil oxidase (LOX), composta por cinco membros, LOX, LOXL1, LOXL2, LOXL3 e LOXL4. A família LOX é responsável pela catalização das ligações cruzadas no colágeno e na elastina, contribuindo para a rigidez da matriz extracelular (MEC). Os membros da família LOX apresentam similaridades na porção C-terminal, bem como domínios semelhantes aos receptores de citocinas (CRL), os domínios conservados de ligação ao cobre e o cofator lisil-tirosil-quinona (LTQ) são elementos fundamentais para a conformação da proteína e para a atividade catalítica necessária. (1). No entanto, a região N-terminal é variável nessas proteínas; LOX e LOXL1 possuem sequências dos seus pró-peptídeos, enquanto que, LOXL2, LOXL3 e LOXL4 abriga quatro domínios conhecidos como SRCR (receptores scavenger ricos em cisteína). Com base nessas semelhanças estruturais de domínios, a família se divide em dois grupos: uma subfamília composta por LOX e LOXL1, e outra por LOXL2, LOXL3 e LOXL4 (2).

LOXL3 está localizado no cromossomo 2p13.3, apresentando 23.462 nucleotídeos e 14 exons (Figura 1a) (3). Codifica uma proteína de 753 aminoácidos com peso molecular de 80,3 kDa. A porção N-terminal de LOXL3, abrangendo os exons 2 a 9, inclui quatro domínios SRCR e um sítio potencial de clivagem para o peptídeo sinal extracelular (4). Com base em sua estrutura predita, é possível que LOXL3 seja secretado e processado no espaço extracelular pela proteína óssea morfogenética 1 (BMP-1). (Figura 1b) (3). LOXL3 já foi descrito desempenhando um papel no espaço extracelular em fibrosarcoma, em cardiomiócitos, na reticulação do colágeno e na junção miotendínea na oxidação da fibronectina na matriz extracelular (3, 5). No citoplasma, a LOXL3 foi observada na região perinuclear em células HeLa com superexpressão da LOXL3, bem como em células de melanoma. (6, 7). Adicionalmente, LOXL3 também pode ser translocado para o núcleo, devido à presença de sinal de localização nuclear na região N-terminal LOXL3 foi descrito no núcleo em células HeLa e em células de baço de ratos (8). A localização citoplasmática e nuclear concomitante foi descrita em câncer gástrico (9). A localização nuclear de LOXL3 foi confirmada pela demonstração de sua interação com a telomerase transcriptase reversa humana (hTERT) (10).

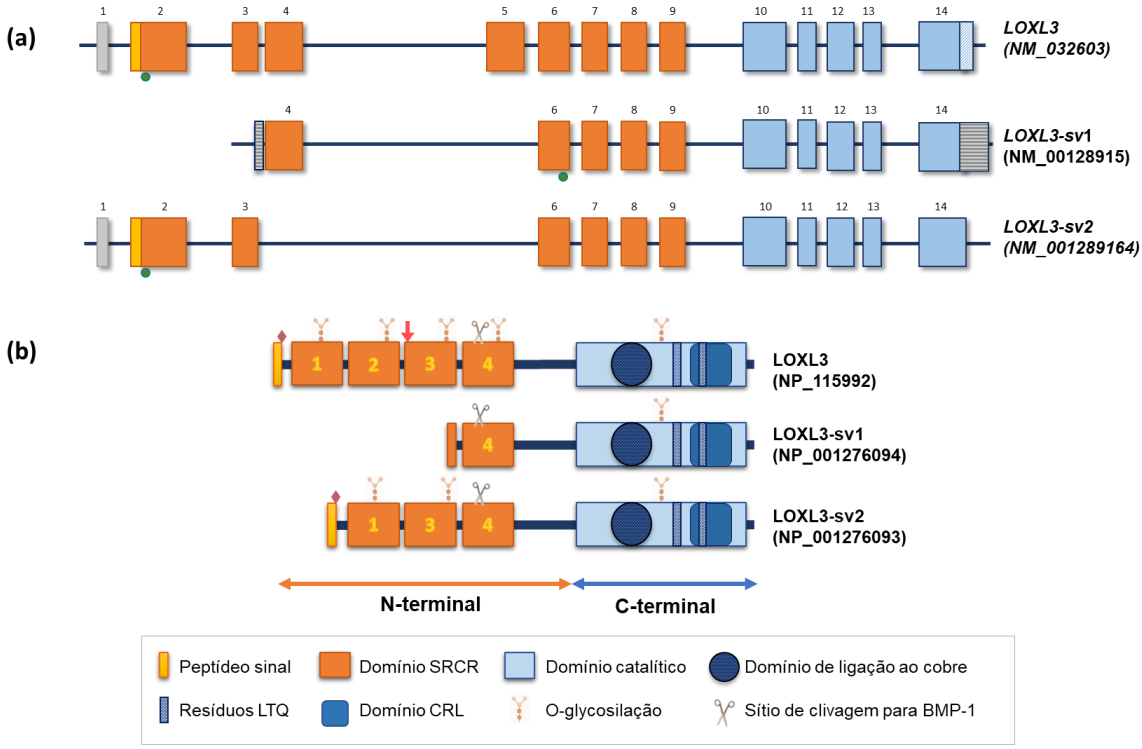

Figura 1. Sequências de RNAs mensageiros e proteínas de LOXL3 e variantes. **(a)** Esquemas da estrutura exon-intron dos transcritas de *LOXL3* humano, com exons representados por caixas e introns por linhas. O principal transcrito de *LOXL3* apresenta 14 exons, (região 5'- caixa cinza) e (3' região não codificada - caixa azul claro). O transcrito *LOXL3*-sv1 não possui os exons 1, 2, 3 e 5 (regiões não codificada - caixas cinza escuro). O transcrito *LOXL3*-sv2 diverge do transcrito principal pela ausência dos exons 4 e 5. As cores laranja e azul representam os exons que codificam as regiões N-terminal e C-terminal, respectivamente, e a cor amarela a região que codifica a sequência peptídeo sinal. Os pontos verdes indicam a localização do codon inicial de tradução. **(b)** Esquemas das estruturas variantes da proteína LOXL3, com domínios de peptídeos sinais, receptores *scavenger* ricos em cisteína (SRCR) na região N-terminal, e domínio catalítico (azul) na região C-terminal. Diamantes vermelhos sinalizam os locais putativos de O-glicosilação; setas vermelhas representam o sinal de localização nuclear. Todas as variantes proteicas compartilham um domínio catalítico comum, que engloba a região de ligação ao cobre, o resíduo lisil-tirosil-quinona (LTQ) e o domínio semelhante ao receptor de citocinas (CRL). Figura utilizada com permissão (11).

1.2. Astrocitomas

Os gliomas são tumores originados da glia, e representam 26,3% de todos os tumores. Dentre eles, os tumores astrocíticos, incluindo glioblastoma (GBM), representam 78,5% de todos os gliomas (12).

Os astrocitomas seguem a classificação da Organização Mundial de Saúde (OMS) quanto ao grau de malignidade, determinado pela presença de indicadores de neoplasias atipia celular, proliferação endotelial, atividade mitótica e necrose (13). As mutações nos genes que codificam a isocitrato desidrogenase 1 e 2 (IDH1/2) são predominantemente identificadas em astrocitomas de baixo grau, abrangendo cerca de 70% a 80% dos casos, e também em glioblastomas (GBM) secundários, que eventualmente se desenvolvem a partir de astrocitomas de menor grau, representando aproximadamente 5% dos casos.(14, 15). Em

glioblastoma (GBM) primário, as mutações recorrentes em IDH1/2 são menos comuns, ocorrendo em apenas 2,5% dos casos (16). Recentemente, os gliomas astrocíticos difusos adultos foram reclassificados de acordo com a presença da mutação de *IDH1/2*, sendo divididos segundo a presença ou não da mutação (Tabela 1). Os astrocitomas difusos com *IDH* mutante são considerados de apenas um único grupo, astrocitoma IDH-mutado, e estes, divididos em graus 2, 3 ou 4, segundo a OMS. O astrocitoma grau 4 IDH-mutado é definido pela presença de uma deleção em homozigoze de *CDKN2A/B* mesmo na ausência de indicativos histológicos, ou seja, parâmetros moleculares podem muitas vezes ser decisivos na classificação do tumor. Já para os astrocitomas difusos grau 4, IDH-selvagem, ou GBM, o critério para classificação molecular é a presença de uma ou mais alterações genéticas (mutação na região promotora de *TERT*, amplificação do gene do receptor do fator de crescimento epidermal (*EGFR*) e alterações nos cromossomos 7 e 10), além de apresentar pelo menos um característica histológica (proliferação microvascular e/ou necrose) (17). Isso permite que tumores com IDH-selvagem sejam classificados como tumores de grau 4, mesmo em casos que, de outra forma, pareçam histologicamente de grau menor (17). As mutações nos genes IDH1/2 estão correlacionadas a um prognóstico mais favorável para os pacientes, além de conferirem uma maior sensibilidade ao tratamento com temozolomida (TMZ) (18), quimioterápico padrão no tratamento de gliomas (19).

Tabela 1. Classificação e principais características dos astrocitomas difusos adultos

Nome	IDH	Grau OMS	Genes com alterações
Astrocitoma, IDH mutado	Mutado	2	Mutação de *IDH1* ou *IDH2*
		3	Mutação de *IDH1* ou *IDH2*
		4	Mutação *IDH1* ou *IDH2*, deleção *CDKN2A/B*
Astrocitoma, IDH selvagem	Selvagem	4	Mutação do promotor *TERT*, amplificação *de EGFR*, alterações do número de cópias (cromossomos +7/-10)

IDH: isocitrato desidrogenase; OMS: Organização Mundial de Saúde; *IDH1*: gene da isocitrato desidrogenase 1, *IDH2*: gene da isocitrato desidrogenase 2, *CDKN2A/B*: gene do inibidor de quinase dependente de ciclina 2A/B; TERT: gene da transcriptase reversa da telomearase; *EGFR:* gene do receptor do fator de crescimento epidermal

1.3. Glioblastomas (grau 4)

Os GBMs são os tumores mais frequentes do tumores malignos cerebrais e do sistema nervoso central (SNC) (ocupando 14.2% de todos tumores, e 50.9% de todos os tumores malignos) e são mais comuns dentre os tumores malignos (49,1%) (20). Adicionalmente à

classificação dada pela OMS, o programa Atlas do Genoma do Câncer (TCGA) descreveu alterações genômicas recorrentes em GBM e propôs uma classificação em subtipos moleculares: clássico, mesenquimal, proneural (21, 22) (Tabela 2).

Tabela 2. Classificação do subtipo molecular dos GBM

Subtipos	Sobrevida (meses)	Características genéticas
Proneural	13-17	Amplificação de *PDGFRA*, mutação de *IDH1* e *TP53*
Clássico	9-14	Amplificação de *EGFR*, *EGFRvIII*, mutação de *PTEN*
Mesenquimal	8-11	Deleção de *NF1* e *RB1*

EGFR: gene do receptor do fator de crescimento epidermal, *EGFRvIII*: variante vIII de *EGFR*, *PTEN*: gene da fosfatase homóloga a tensina, *PDGFRA*: gene do receptor alfa do fator de crescimento derivado de plaquetas, *IDH1*: gene da isocitrato desidrogenase 1, *TP53*: gene de p53, *NF1*: gene da neurofibromina, *RB1*: gene do correpressor transcricional RB1

O subtipo clássico foi caracterizado principalmente pela amplificação e mutações de *EGFR*, mutações de *PTEN* e a presença da variante *EGFRvIII*. Já o subtipo mesenquimal apresenta majoritariamente mutações nos genes *NF1* e *RB1*. Já o subtipo proneural é caracterizado principalmente por uma amplificação focal na região do locus 4q12, onde se encontra o PDGFRA, acompanhada por uma expressão elevada do gene (21). O prognóstico varia conforme o subtipo molecular, destacando-se o subtipo proneural, que exibe uma sobrevida média mais prolongada (Tabela 2) (22, 23).

1.4. LOXL3 e astrocitomas

Os membros da família lisil oxidase têm sido objeto de estudo como potenciais alvos terapêuticos para diversas doenças, incluindo fibrose e tumores (11, 24-27). Em câncer, LOXL3 desempenha um papel na transição epitélio-mesênquima (EMT) em vários tipos de tumores (28, 29), na tumorigenese e progressão em melanoma (7, 30), invasão tumoral e no pior no prognóstico dos pacientes com carcinoma gátrico (9), efusão pleural em câncer de mama e ovário (31, 32), e outros tipo de tumores, como neoplasmas mieloproliferativos (33). Além disso, a expressão de *LOXL3* foi correlacionada com câncer colorretal, com impacto no prognóstico do tratamento (34, 35). Em astrocitomas, particularmente, seu papel funcional ainda é pouco explorado. Num estudo conduzido por nosso laboratório, com o intuito de identificar novos alvos terapêuticos para astrocitomas, investigamos os genes com expressão aumentada no glioblastoma (GBM) em comparação com o astrocitoma pilocítico, anteriormente classificado como grau 1. Entre os genes mais expressos, notamos que o gene

que codifica a enzima LOX estava 11 vezes mais expresso no GBM. (36). Nossas investigações revelaram que a hiperexpressão de *LOXL3* pode ser um indicador de prognóstico desfavorável para pacientes com glioblastoma (GBM), enfatizando seu potencial papel crucial no desenvolvimento e progressão desses tumores.

2 JUSTIFICATIVA

O objetivo deste trabalho foi investigar o papel funcional da enzima LOXL3 em astrocitomas, devido à carência de dados na literatura sobre sua função e expressão em tumores, especialmente em astrocitomas.

3 DESENHO EXPERIMENTAL E VISÃO GERAL DOS ARTIGOS

Foram realizados ensaios *in silico* e *in vitro* para analisar o papel funcional de LOXL3 em astrocitomas. Inicialmente, foi realizado um silenciamento transitório com siRNA na linhagem celular U87MG de GBM, seguido da avaliação por ensaios funcionais e transcriptoma (publicação 1). Além disso, foi realizada uma avaliação da expressão gênica, proteica e *in silico* dos membros da família LOX e genes relacionados à MEC, em astrocitomas de diferentes graus malignidade, com e sem mutação de *IDH1*/2 (publicação 2). Por fim, para dar continuidade às análises do papel de LOXL3 em GBM, foi realizado um nocaute gênico de *LOXL3* através do sistema CRISPR-Cas9 (publicação 3 submetido).

Publicação 1

LOXL3 Silencing Affected Cell Adhesion and Invasion in U87MG Glioma Cell

4 Publicação 1 - LOXL3 Silencing Affected Cell Adhesion and Invasion in U87MG Glioma Cells

Objetivo geral: Analisar o papel funcional de LOXL3 através do silenciamento transitório da expressão gênica em linhagem celular de GBM humano, U87MG

a) Analisar a expressão *in silico* de *LOXL3* em câncer, principalmente em astrocitomas, linhagens celulares, e nos diferentes subtipos moleculares de GBM e avaliar o impacto da sobrevida nos pacientes com GBM com hipo e hiperexpressão de *LOXL3*
b) Realizar o silenciamento da expressão gênica de LOXL3 por meio de siRNA na linhagem celular U87MG e avaliar a eficácia desse procedimento por meio de técnicas como PCR em tempo real, Western blot e imunofluorescência
c) Realizar o sequenciamento do transcriptoma e a análise de enriquecimento dos genes diferencialmente expressos nas células silenciadas para *LOXL3* em relação ao controle, a fim de identificar as vias de sinalização nas quais LOXL3 esteja envolvido;
d) Avaliar o efeito do silenciamento de *LOXL3* na viabilidade, adesão, invasão e morte celular.
e) Avaliar possíveis alterações na morfologia celular nas células silenciadas.
f) Avaliar se os efeitos do silenciamento são célula-dependente
g) Analisar, *in silico*, os genes e proteínas das vias de sinalização associadas ao *LOXL3* por meio da exploração de bancos públicos de dados de transcriptoma específicos para astrocitomas..

International Journal of *Molecular Sciences*

MDPI

Article

LOXL3 Silencing Affected Cell Adhesion and Invasion in U87MG Glioma Cells

Talita de S. Laurentino [1,*], Roseli da S. Soares [1], Antonio M. Lerario [2], Suely K. N. Marie [1] and Sueli M. Oba-Shinjo [1,*]

[1] Cellular and Molecular Biology Laboratory (LIM 15), Neurology Department, Faculdade de Medicina (FMUSP), Universidade de Sao Paulo, Sao Paulo 01246-000, SP, Brazil; roselicem@yahoo.com.br (R.d.S.S.); sknmarie@usp.br (S.K.N.M.)

[2] Department of Internal Medicine, Division of Metabolism, Endocrinology and Diabetes, University of Michigan, Ann Arbor, MI 48109, USA; amlerario@gmail.com

* Correspondence: talitalaurentino@usp.br (T.d.S.L.); suelimoba@usp.br (S.M.O.-S.); Tel.: +55-11-3061-8310 (T.d.S.L. & S.M.O.-S.)

Abstract: Lysyl oxidase-like 3 (LOXL3), belonging to the lysyl oxidase family, is responsible for the crosslinking in collagen or elastin. The cellular localization of LOXL3 is in the extracellular space by reason of its canonical function. In tumors, the presence of LOXL3 has been associated with genomic stability, cell proliferation, and metastasis. In silico analysis has shown that glioblastoma was among tumors with the highest *LOXL3* expression levels. *LOXL3* silencing of U87MG cells by siRNA led to the spreading of the tumor cell surface, and the transcriptome analysis of these cells revealed an upregulation of genes coding for extracellular matrix, cell adhesion, and cytoskeleton components, convergent to an increase in cell adhesion and a decrease in cell invasion observed in functional assays. Significant correlations of *LOXL3* expression with genes coding for tubulins were observed in the mesenchymal subtype in the TCGA RNA-seq dataset of glioblastoma (GBM). Conversely, genes involved in endocytosis and lysosome formation, along with MAPK-binding proteins related to focal adhesion turnover, were downregulated, which may corroborate the observed decrease in cell viability and increase in the rate of cell death. Invasiveness is a major determinant of the recurrence and poor outcome of GBM patients, and downregulation of LOXL3 may contribute to halting the tumor cell invasion.

Keywords: LOXL3; lysyl oxidase; glioblastoma; cytoskeleton; extracellular matrix; cell death; endocytosis

check for updates

Citation: Laurentino, T.d.S.; Soares, R.d.S.; Lerario, A.M.; Marie, S.K.N.; Oba-Shinjo, S.M. LOXL3 Silencing Affected Cell Adhesion and Invasion in U87MG Glioma Cells. *Int. J. Mol. Sci.* **2021**, *22*, 8072. https://doi.org/10.3390/ijms22158072

Academic Editor: Giovanni Luca Gravina

Received: 23 April 2021
Accepted: 22 July 2021
Published: 28 July 2021

Publisher's Note: MDPI stays neutral with regard to jurisdictional claims in published maps and institutional affiliations.

Copyright: © 2021 by the authors. Licensee MDPI, Basel, Switzerland. This article is an open access article distributed under the terms and conditions of the Creative Commons Attribution (CC BY) license (https://creativecommons.org/licenses/by/4.0/).

1. Introduction

Glioblastoma (GBM), the most aggressive and common type of malignant brain tumor [1], is characterized by rapid growth and invasion, neovascularization, and necrosis [2]. Initially, gliomas were classified based only on their histologic characteristics. However, in 2016, the World Health Organization restructured the classification of central nervous system tumors, dividing astrocytomas into two groups: diffuse astrocytic tumors (including GBM) and other astrocytic tumors. In addition, molecular features, including isocitrate dehydrogenase (NADP(+)) 1/2 (IDH1/2) mutations, have been incorporated into the classification of gliomas [3]. In addition to the World Health Organization classification, The Cancer Genome Atlas (TCGA) network presented the genetic signatures of GBM. Based on molecular alterations, GBMs were subdivided into classical, mesenchymal, and proneural molecular subtypes [4,5]. Maximal tumor resection, followed by radiotherapy and chemotherapy with temozolomide (TMZ), is currently the standard treatment for patients with GBM. Nonetheless, a high recurrence rate and resistance to TMZ frequently occur in patients with GBM, resulting in a median overall survival of 15 months [6].

Lysyl oxidase-like 3 (LOXL3), a copper-dependent amine oxidase, belongs to the lysyl oxidase family which comprises four other members (LOX, LOXL1, LOXL2, and LOXL4).

These proteins are responsible for the oxidative deamination of the amine group of lysine residues in tropocollagen, converting collagen or elastin monomers into insoluble fibers [7]. The lysyl oxidase family is divided into two subgroups according to the similarities in the N-terminal region. LOX and LOXL1 present pro-sequences in the N-terminal, thereby leading to their secretion as inactive pro-enzymes. In contrast, LOXL2, LOXL3, and LOXL4 contain four scavenger receptor cysteine-rich domains [8]. The C-terminal domain presents catalytic activity and is conserved across the lysyl oxidase family proteins. This region contains a copper-binding motif, lysyl-tyrosyl-quinone cofactor residues, and a cytokine receptor-like domain. Conversely, the N-terminal region varies among the members of the lysyl oxidase family [9,10].

Owing to its amine oxidase activity, LOXL3 is localized in the extracellular space. Based on its predicted structure, LOXL3 can be secreted in the extracellular matrix (ECM) and is processed by bone morphogenetic protein 1 (BMP1) [11]. Conversely, LOXL3 can also be translocated to the nucleus due to a bipartite nuclear localization signal (residues 293–311), suggesting additional roles [11–13]. Other functions beyond amine oxidase activity have been attributed to LOXL3, such as oxidation of fibronectin and consequently activation of the integrin pathway [14]. Moreover, it may act as a dual enzyme with deacetylation and deacetylimination activities of STAT3 to control the inflammatory response [15]. In tumors, LOXL3 interacts with SNAIL, a transcription factor involved in the epithelial–mesenchymal transition process, thereby contributing to metastasis and tumor progression [16]. Furthermore, LOXL3 maintains genomic stability in melanoma by association with oncogenic BRAF in melanogenesis and promotes sustained proliferation [17]. It is also upregulated in various tumors, such as gastric cancer cells, breast cancer, myeloproliferative neoplasms, ovarian carcinoma, and colorectal cancer [13,18–22], suggesting that it may be a target candidate for the treatment of tumors.

Although LOXL3 plays different roles in tumorigenesis and in tumor progression, there are no studies investigating the expression of LOXL3 expression in GBM. Therefore, we analyzed the contribution of LOXL3 to the pathogenesis and aggressiveness of GBM through in silico analysis and cellular assays using the U87MG glioma cell line as a model system.

2. Results

2.1. LOXL3 Is Overexpressed in Human GBM

Initially, we investigated the expression of LOXL3 in 32 different types of cancer using 10,967 samples from the TCGA RNA-seq database. High LOXL3 expression levels were detected in 10 types of cancer, including GBM (Figure 1A, in red). The cell lines derived from gliomas (U138MG and U87MG) were in the top five cell lines presenting the highest LOXL3 expression levels among the 64 human cell lines of the HPA study (Figure 1B). The GEPIA2 web tool was used to compare the levels of LOXL3 in normal brain samples and GBM cases according to the molecular mesenchymal, classical, and proneural subtypes (Figure 1C). All three GBM subtypes presented a significantly higher expression of LOXL3 compared with the normal brain. Although the differences detected among the GBM subtypes were not statistically significant, the mesenchymal subtype presented the highest LOXL3 expression levels compared with the classical and proneural subtypes. Moreover, the levels of LOXL3 expression affected the outcome of patients with GBM. Patients who presented an upregulation LOXL3 by $\leq$40% of its highest expression level were associated with reduced overall survival versus those who exhibited downregulation of the same range ($p = 0.039$, Kaplan–Meier survival analysis) (Figure 1D). Additionally, the impact of the expression levels of LOXL3 on survival at 20 months was clear, as only 20% and 35% of patients survived in the high- and low-expression groups, respectively. Collectively, these results suggest that LOXL3 is overexpressed in GBM, impacting overall survival and playing a still unexplored role in this tumor type.

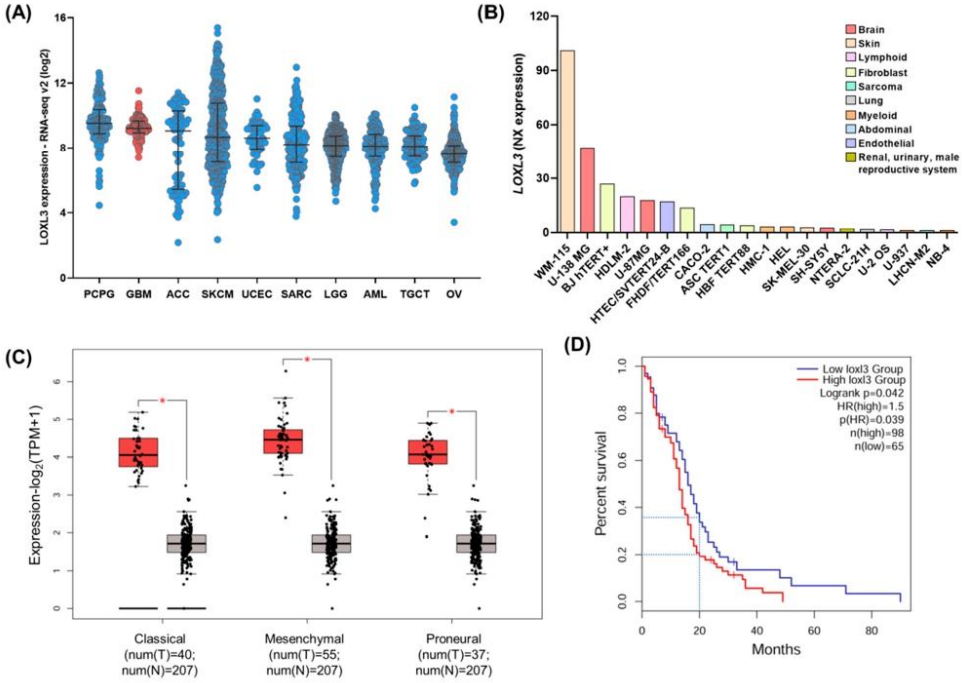

Figure 1. *LOXL3* expression in cancer tissues and cell lines. (**A**) *LOXL3* expression levels in 10 different types of cancer using data obtained from of The Cancer Genome Atlas (TCGA) database of Pan-cancer Atlas. The graph represents the log2 scale of the RPKM of tumors with higher median values. Bars indicate the median and interquartile ranges of each group. (**B**) *LOXL3* expression in different cell lines using data obtained from The Human Protein Atlas. The results are reported as normalized expression (NX) values ≥ 1 of immortalized cancer cells. (**C**) Boxplots illustrating *LOXL3* expression in GBM molecular subtypes and normal brain tissues in TCGA and GTEx, respectively, based on GEPIA2 analysis. The *Y*-axis represents the log2 (TPM+1) of *LOXL3* expression levels. Statistical differences between GBM (T) and normal brain (N) are represented by asterisk: * $p < 0.05$ denotes statistically significant differences. (**D**) Overall survival rate by Kaplan–Meier analysis in GBM cases separated according to *LOXL3* expression (40% with higher and lower levels). Analysis was performed using GEPIA2. Abbreviations: ACC, adrenocortical carcinoma; AML, acute myeloid leukemia; GBM, glioblastoma; GEPIA2, Gene Expression Profiling Interactive Analysis 2; GTEx, Genotype-Tissue Expression; LGG, low-grade gliomas; *LOXL3*, lysyl oxidase-like 3; OV, serous ovarian cancer; PCPG, pheochromocytoma; RPKM, reads per kilobase per million; SARC, sarcoma; SKCM, cutaneous melanoma; TGCT, testicular germ cell tumor; TPM, transcripts per million.

2.2. *LOXL3* Silencing by siRNA

The role of LOXL3 in GBM was investigated using the U87MG cell model. As these cells express high levels of *LOXL3* (according to the HPA study) and display tumorigenic capacity, this may allow testing of selected targets using animal models in future studies. Two different siRNAs (siRNA1 and siRNA2) were used to silence *LOXL3*. Four days after transfection with these siRNAs, the cells exhibited only 15.3% and 49.1% *LOXL3* mRNA expression, respectively, versus NTC (Figure 2A). There was no difference in expression levels of LOXL3 protein analyzed by Western blotting (41.5% and 39.2% for siRNA1 and siRNA2 versus NTC, respectively) (Figure 2B). However, immunofluorescence staining of LOXL3 showed expression of 13.5% and 25.1% for siRNA1 and siRNA2, respectively (Figure 2C and 2D), relative to NTC, at day 4 after transfection. Moreover, a morphological change was observed after *LOXL3* silencing characterized by an enlargement of the tumor

cell surface, which was more prominent with siRNA1 (Figure 2D). As more efficient downregulation of *LOXL3* was obtained with siRNA1, all functional analyses were conducted on day 4 after transfection with this siRNA1.

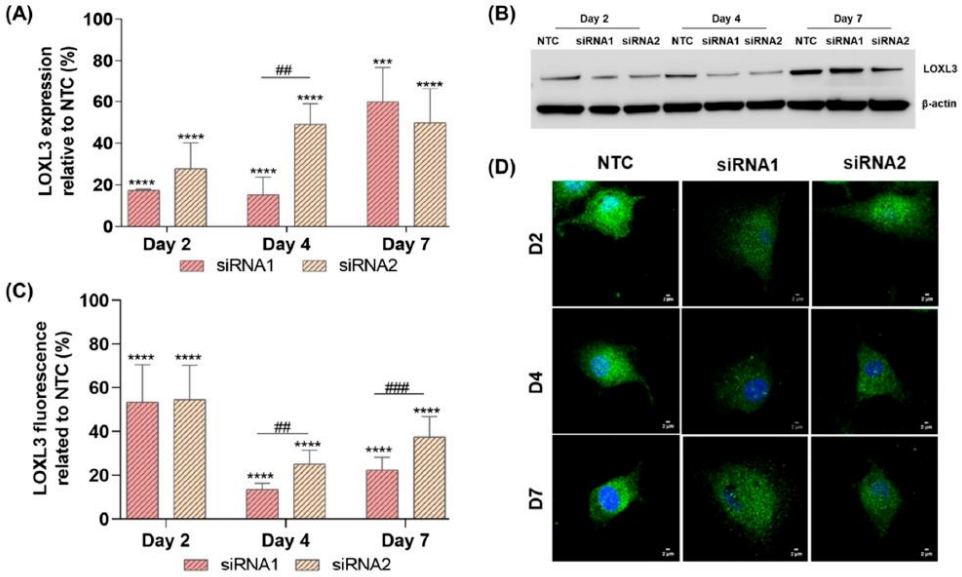

Figure 2. Downregulation of *LOXL3* expression by siRNA in U87MG cells. (**A**) RT-qPCR analysis of *LOXL3* expression relative to control (NTC) at 2, 4, and 7 days after transfection with two different siRNA sequences (siRNA1 and siRNA2). (**B**) Western blotting analysis of LOXL3 expression in the control (NTC) group and after silencing with siRNA1 and siRNA2. β-actin was used as loading control. LOXL3: 83 kDa; β-actin: 42 kDa. (**C**) Quantification of LOXL3 fluorescence in control (NTC) and siRNA1- and siRNA2-transfected U87MG cells. Fluorescence was measured per cell. (**D**) Immunofluorescence for LOXL3 (green) and nucleus (DAPI, blue) was evaluated in control (NTC) and siRNA1- and siRNA2-treated U87MG cells at 2 (D2), 4 (D4), and 7 (D7) days after transfection. Bars represent the means ± standard deviations of independent experiments. Statistically significant differences between control (NTC) and siRNA1- and siRNA2-transfected U87MG cells are represented by asterisks: **** $p < 0.00001$, *** $p < 0.0001$. Statistically significant differences between siRNA1- and siRNA2-transfected cells are represented by hashes: ### $p < 0.0001$, ## $p < 0.001$. Abbreviations: DAPI, 4′,6-diamidino-2-phenylindole; LOXL3, lysyl oxidase-like 3; NTC, nontarget control; RT-qPCR, real-time quantitative polymerase chain reaction; siRNA, small interfering RNA.

2.3. Transcriptome Analysis

Transcriptome analysis of *LOXL3*-siRNA1 and NTC-siRNA U87MG cells was performed to analyze the signaling pathways involved in GBM cells. In total, 15,036 genes were mapped (Table S1), and 433 differentially expressed genes (DEGs) were identified between *LOXL3*-silenced and control cells (log2 fold change ≥ 0.7 and ≤ -0.7 and adjusted $p \leq 0.05$ by Benjamin–Hochberg correction). Among those, 220 and 213 genes were upregulated and downregulated, respectively. The efficiency of *LOXL3* silencing was confirmed by a log2 fold change of −0.46, corresponding to 40% downregulation induced by siRNA1. The enrichment analysis of the upregulated DEGs showed a set of genes related to ECM organization (GO:0043062 and GO:0030198, both with false discovery rate (FDR) = 0 and p = 0) and collagen metabolism (GO:0032963, FDR = 4.28×10^{-4}, $p = 1.47 \times 10^{-7}$) within the biological processes category. Enrichment of the ECM of DEGs was confirmed in the cellular component category, with the highest enrichment ratio (56.4) observed for microfibril (GO:0001527, FDR = 1.63×10^{-6}, $p = 1.25 \times 10^{-4}$), followed by ECM (GO:0044420,

FDR = 4.03×10^{-9}, $p = 1.37 \times 10^{-7}$; GO:0062023, FDR = 6.37×10^{-7}, $p = 4.34 \times 10^{-5}$) and adhesion processes (GO:00005924, FDR = 1.11×10^{-7}, $p = 4.99 \times 10^{-6}$; GO:0005925, FDR = 1.11×10^{-7}, $p = 5.6 \times 10^{-6}$). Analysis of molecular function also confirmed the differential expression of ECM genes (GO: 0005201, FDR = 1.32×10^{-6}, $p = 7.05 \times 10^{-10}$) (Figure 3A). In fact, several genes coding for components of ECM microfibril, such as collagens (*COL5A1*, *COL6A1*, *COL7A1*, *COL27A1*), fibrillins (*FBN1*, *FBN2*), fibronectin (*FN1*), tenascin (*TNC*), and microfibril-associated glycoproteins (*MFAP2*, *MFAP4*), were significantly upregulated. Moreover, genes coding for enzymes, such as lysyl hydroxylases (*PLOD1*, *PLOD2*), lysyl oxidases (*LOX*, *LOXL2*), and *BMP1*, were also upregulated. Furthermore, genes coding for the intracytoplasmic focal adhesion complex, such as caveolins (*CAV1*, *CAV2*), talin 2 (*TLN2*), and calponin 2 (*CNN2*), were upregulated. This was accompanied by the upregulation of genes related to stress fibers such as CNN2 and FAP. Moreover, genes coding for caveolae plasma membrane caveolins (CAVs: *CAV1*, *CAV2*) and several tubulins, components of the cellular cytoskeleton, were upregulated (Figure 3C,D).

Downregulated DEGs were conversely enriched in cellular components corresponding to vacuoles (GO:0005774, FDR = 3.25×10^{-4}, $p = 1.84 \times 10^{-6}$) and endosomes (GO:0044440, FDR = 3.25×10^{-4}, $p = 1.94 \times 10^{-6}$; GO:0010008, FDR = 3.65×10^{-4}, $p = 2.48 \times 10^{-6}$) (Figure 3B). The downregulated genes coded for endosomal vesicle formation, such as tumor necrosis factor receptor-associated factor 6 (*TRAF6*) and secretory carrier membrane protein 1 (*SCAMP1*); for multivesicular formation, such as components of the endosomal sorting complex required for transport II (ESCRT-II) complexes (*VPS25*, *VPS36*); and for components of vacuolar ATPases (*ATP6V1C1*, *ATP6V1B2*). Members of the RAS oncogene family involved in endosome recycling (*RAB3D*, *RAB22A*) were also downregulated. Moreover, genes coding for proteins involved in the fusion of these membrane-bound organelles, such as phosphoinositide kinase and FYVE-type zinc finger containing (*PIKFYVE*), and chaperones, such as heat shock protein family A (Hsp70) member 8 (*HSPA8*), were similarly downregulated. Additionally, the highest enrichment ratio (19.61) of downregulated genes on molecular function was associated with the mitogen-activated protein kinase (MAPK) kinase kinase binding (GO:0031435, FDR = 1.03×10^{-2}, p = 4.39×10^{-5}) (Figure 3B), which included four genes coding for binding proteins: mitogen-activated protein kinase 1 (*MAPK1*), serine/threonine kinase 38 (*STK38*), *TRAF6*, and mitogen-activated protein kinase 8 interacting protein 1 (*MAPK8IP1*).

We focused on the analysis of processes related to the ECM and cell adhesion for upregulated DEGs (red boxes in Figure 3A) and to endosome/vacuoles and MAPK-binding proteins for downregulated DEGs (red boxes in Figure 3B). Furthermore, the protein–protein interaction map of upregulated and downregulated DEGs was significantly connected as shown in the network constructed using the Cytoscape STRING plugin (Figure 3C). Figure 3D,E presents upregulated and downregulated DEGs connected in the protein–protein interaction network in the heatmaps.

2.4. LOXL3 Downregulation in U87MG Cells Decreased Viability and Invasion, Induced Death, and Increased Adhesion

Downregulation of *LOXL3* in U87MG cells significantly reduced cell viability compared with that observed in NTC cells at day 4 after transfection with siRNA (Figure 4A). A significant increase in annexin V-positive cells was detected by flow cytometry, indicating early cell death (Figure 4B). This response was enhanced by the costimulatory effect of TMZ, the alkylating agent used in standard care of patients with GBM. An increase of approximately 20% was observed with the combined treatment versus TMZ monotherapy (Figure 4B). Although a slight increment in late cell death, measured in cells double-stained with annexin V-FITC and propidium iodide, was observed after the downregulation of *LOXL3* and following treatment with TMZ, the differences did not reach statistical significance. Cell adhesion was also increased (Figure 4C) and cell invasion (Figure 4D) was decreased following LOXL3 downregulation versus NTC at day 4 after transfection.

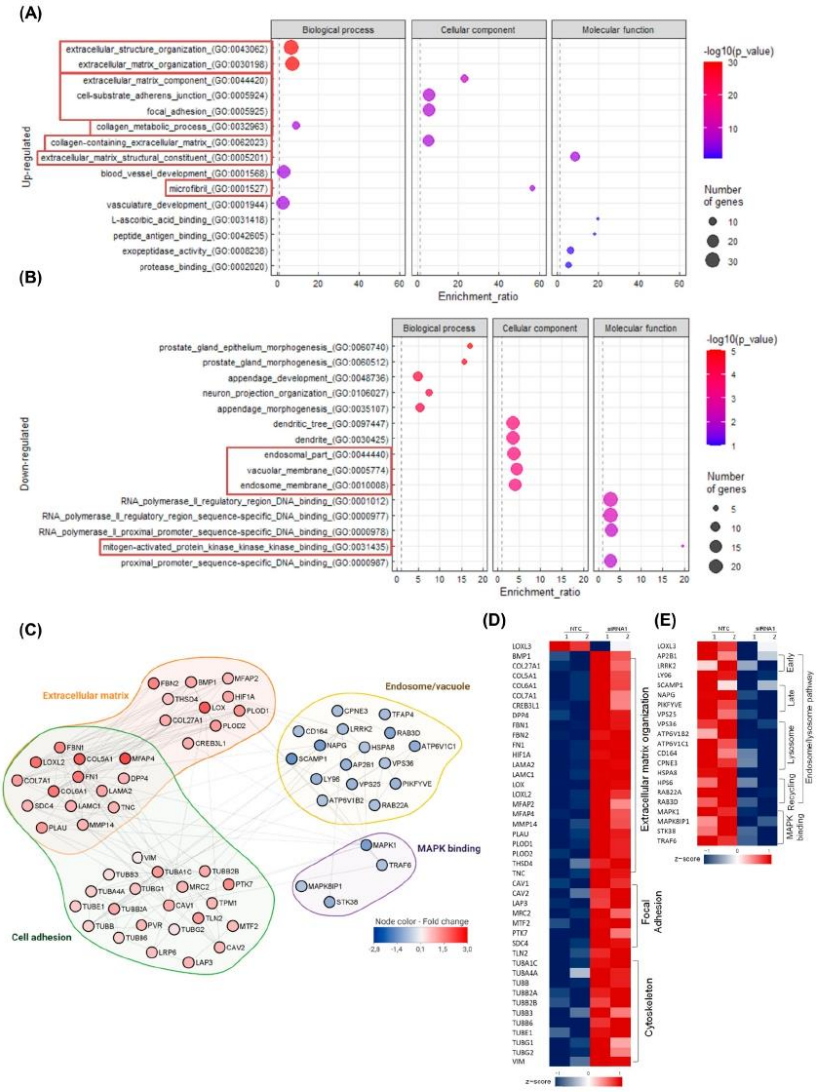

Figure 3. Transcriptome analysis of U87MG cell line with *LOXL3* expression knocked down by siRNA. Dot plots illustrating the top five most enriched Gene Ontology (GO) terms (biological process, cellular component, and molecular function) of differentially expressed genes (**A**) upregulated and (**B**) downregulated in siRNA1-transfected U87MG cells compared with control. Red rectangles indicate the GO processes identified in the protein–protein interaction (PPI) analysis. (**C**) The PPI network of proteins related to pathways identified in the WebGestalt analysis performed using the STRING app of the Cytoscape software. The proteins are represented by nodes, and the interactions are represented by edges (score value ≥ 0.5). Heatmaps representing the RNA-seq expression of key genes coding for proteins involved in the extracellular matrix, focal adhesion, and cytoskeleton (**D**) and endosome/lysosome and MAPK-binding proteins (**E**) in NTC and siRNA1-transfected cells. Each line represents the z-score of RPKM values. Abbreviations: LOXL3, lysyl oxidase-like 3; MAPK, mitogen-activated protein kinase; NTC, nontarget control; RNA-seq, RNA sequencing; RPKM, reads per kilobase per million; siRNA, small interfering RNA; WebGestalt, Web-Based Gene Set Analysis Toolkit.

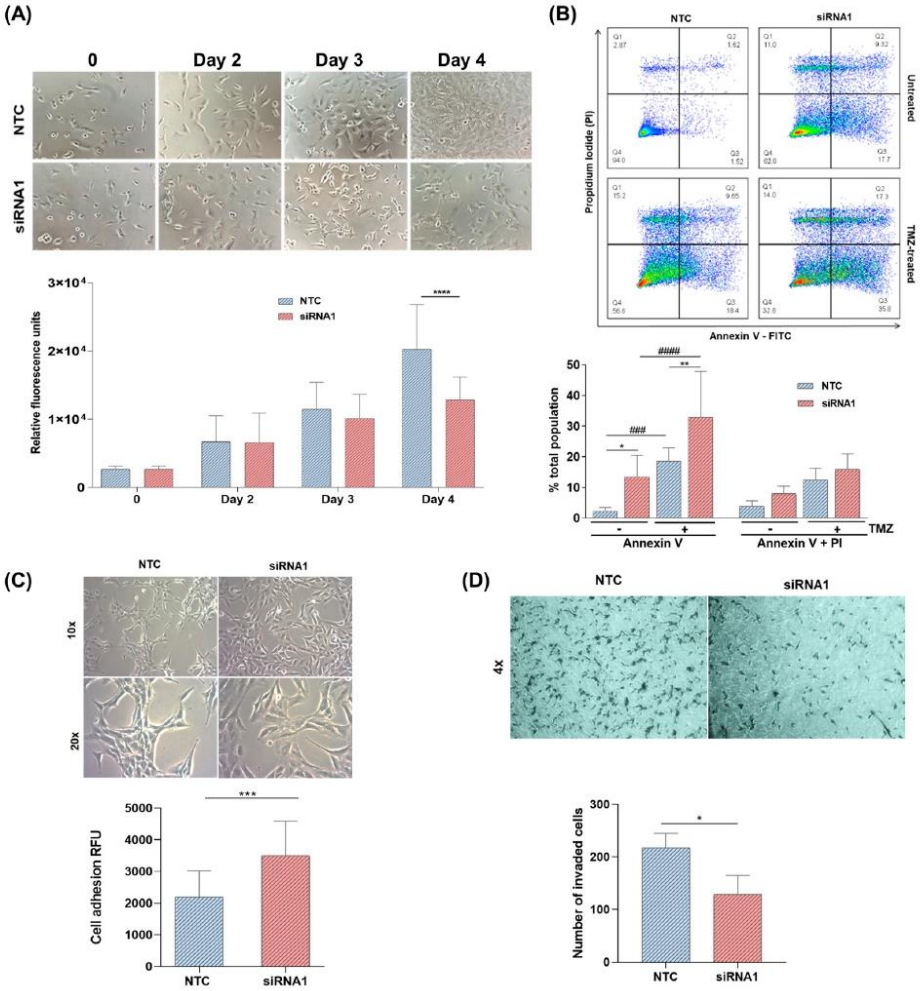

Figure 4. Effect of LOXL3 downregulation on cell viability and apoptosis of U87MG cells. (**A**) Representative images (magnification of 10×) and analysis of viability assay. (**B**) Flow cytometry charts and analysis of apoptosis assay using annexin V-FITC and propidium iodide staining of LOXL3-siRNA1 silenced cells compared to NTC. Apoptosis assays were performed with temozolomide (TMZ)-treated cells and compared with untreated cells. (**C**) Representative images (magnification of 10× and 20×) and analysis of cell adhesion assay of LOXL3-siRNA1 cells in comparison to control (NTC) cells. (**D**) Representative images (magnification of 4×) and analysis of cell invasion assay of LOXL3-siRNA1 cells in comparison to control (NTC) cells. Bars represent the means ± standard deviations of replicates of independent experiments. Statistically significant differences between control (NTC) and siRNA1 cells are represented by asterisks: **** $p < 0.00001$, *** $p < 0.0001$, ** $p < 0.001$, * $p < 0.05$. Statistically significant differences between cells with no treatment and cells with TMZ treatment are represented by hashes: #### $p < 0.0001$, ### $p < 0.001$.

2.5. LOXL3 Downregulation in U87MG Cells Altered Morphology and Cytoskeletal Rearrangement

Additionally, when the cell cytoskeleton was visualized by actin and tubulin immunofluorescent staining 4 days after transfection with siRNA, clear morphological differences were observed between the cells with downregulated LOXL3 and NTC cells (Figure 5A). LOXL3-siRNA U87MG cells presented an increased cell surface, as demonstrated in Figure 5B, exhibiting a reorganization of the cytoskeleton with actin fibers extending to the periphery of the cells and a nonpolarized tubulin rearrangement.

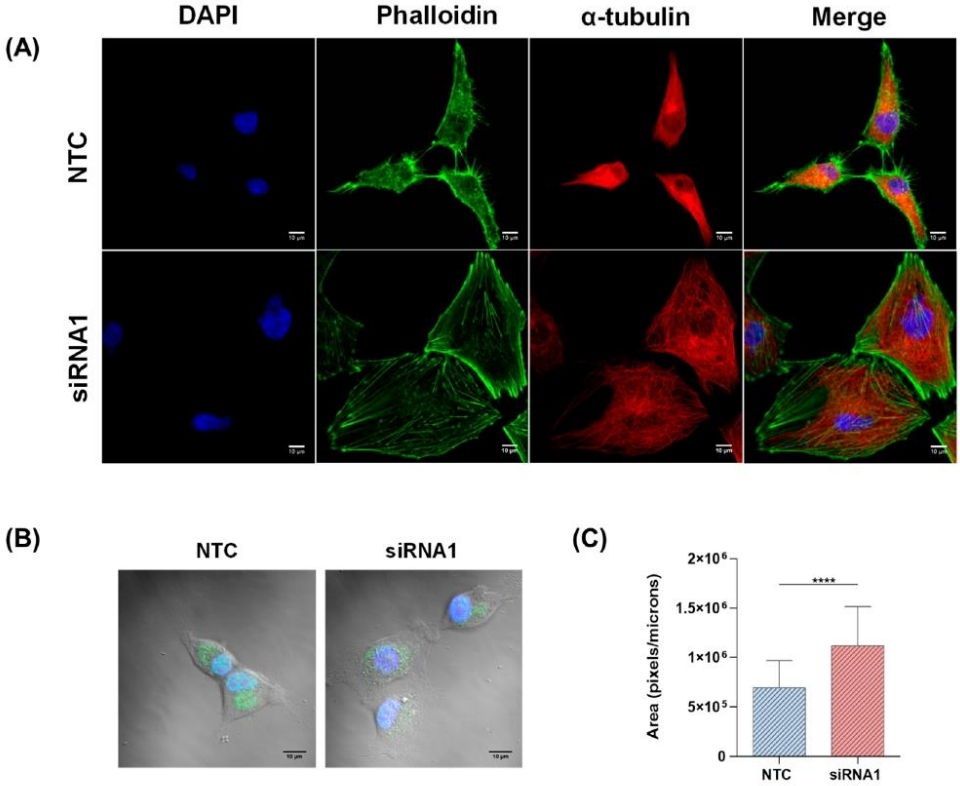

Figure 5. Effect of LOXL3 downregulation on cell morphology of U87MG cell line. (**A**) Representative images (magnification of 20×) of immunofluorescence staining patterns for nucleus (DAPI, blue), phalloidin (green), and α-tubulin (red) evaluated in control (NTC) and siRNA1-transfected cells after 4 days in U87MG cells. Scale bar, 10 μm. (**B**) Overlay of bright-field and fluorescence (LOXL3 and nucleus staining) representative images of control (NTC) and LOXL3-siRNA1. Scale bar, 10 μm. (**C**) Total surface area of cells presented in (**B**). Bars represent the means ± standard deviations of replicates of independent experiments. Statistically significant differences between control (NTC) and siRNA1 cells are represented by asterisks: **** $p < 0.0001$.

2.6. LOXL3 Silencing in T98G Cells and Human Glioblastoma Samples

T98G glioma cell line was also silenced for LOXL3 with siRNA1, with efficacy confirmed by RNA expression and protein analysis 4 days after transfection (Figure 6A). Morphological changes occurred in *LOXL3*-silenced T98G cells (Figure 6B), which exhibited enlarged cell surfaces. However, the tubulin rearrangement was not prominent compared to the observed alteration in U87MG-*LOXL3*-silenced cells (Figure 6C). Inter-

estingly, the TCGA RNA-seq dataset of different molecular subtypes of GBM showed a significant correlation in expression between *LOXL3* and tubulin alpha (*TUBA1C* and *TUBA4A*) in the mesenchymal subtype, which was not detected in classical and proneural subtypes (Figure 6D,E).

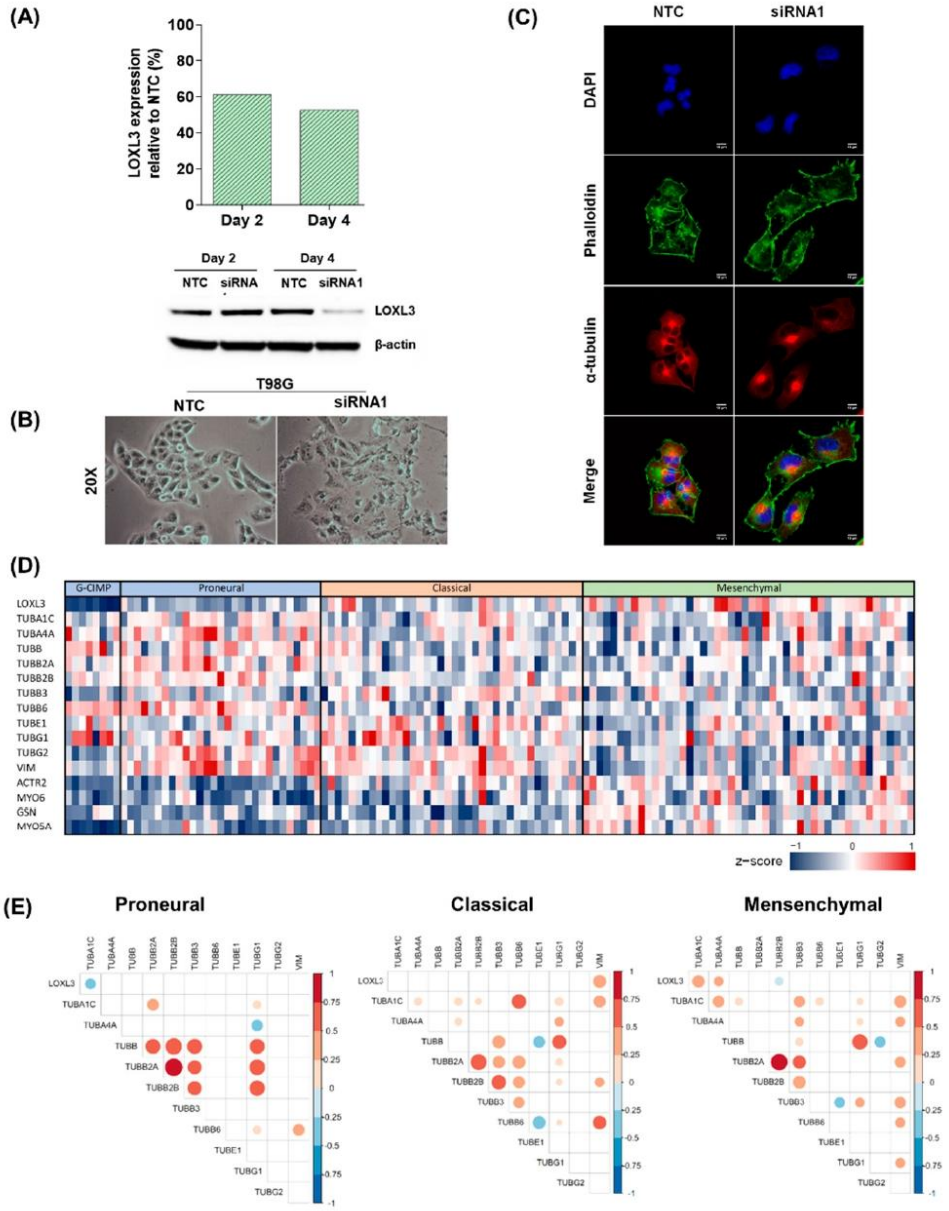

Figure 6. Downregulation of LOXL3 expression by siRNA in T98G cells. (**A**) LOXL3 expression relative to control (NTC) after 2 and 4 days of siRNA1 transfection analyzed by qRT-PCR and by Western blot. β-actin was used as loading control.

LOXL3: 83 kDa; β-actin: 42 kDa. (**B**) Representative images (magnification of 20×) and analysis of LOXL3-siRNA1 and control (NTC) cells. (**C**) Representative images (magnification of 20×) of immunofluorescence staining patterns for phalloidin (green), α-tubulin (red), and nucleus (DAPI, blue) evaluated in control (NTC) and siRNA1-transfected cells after 4 days in T98G cells. Scale bar, 10 µm. (**D**) Heatmaps representing RNA-seq expression of GBM samples in the TCGA database for the same key genes. (**E**) Spearman correlation matrix among expression levels of genes involved in actin dynamics of GBM molecular subtypes of the TCGA database. The color bars on the right indicate the levels of correlation ranging from blue (negative correlation) to orange (positive correlation). The color intensiveness and the circle sizes are proportional to the values of r. Only the correlations with $p < 0.05$ are plotted. Abbreviations: DAPI, 4′,6-diamidino-2-phenylindole; LOXL3, lysyl oxidase-like 3; NTC, nontarget control; RT-qPCR, real-time quantitative polymerase chain reaction; siRNA, small interfering RNA; TCGA, The Cancer Genome Atlas.

3. Discussion

LOXL3, known for its function as a lysyl oxidase, has been associated with embryonic development [23,24] and diverse pathologies, including collagenopathies [25,26] and fibrosis [27]. In cancer, upregulation of LOXL3 has been detected in several tumor types such as gastric, breast, ovarian, and colorectal carcinomas and myeloproliferative tumors [14,19–22]. In fact, our in silico analyses of the TCGA transcriptome database confirmed the previously reported high expression of *LOXL3* in such tumors. These findings were also supported by a recently reported similar analysis [28]. Interestingly, GBM, the most frequent and malignant type of brain tumor in adults, was among the top 10 tumors presenting *LOXL3* overexpression. Notably, the expression levels of *LOXL3* in GBM were higher than those detected in normal brain tissue, independently of the GBM molecular subtype. Moreover, the expression levels of *LOXL3* affected the patient outcomes; higher *LOXL3* expression was associated with poorer overall survival. A similar clinical impact has been observed in patients with gastric cancer [13].

Previous studies investigating the role of LOXL3 in cancer have found an association with tumor progression and metastasis through physical interaction with SNAIL, a transcription factor involved in the epithelial–mesenchymal transition process [17] and cell proliferation [29]. Additionally, in melanoma, LOXL3 maintains genomic stability through an association with oncogenic BRAF and promotes sustained proliferation [18]. We sought to further understand the function of LOXL3 in brain tumors. Therefore, we treated the U87MG-GBM cells with *LOXL3*-siRNA to analyze the intracellular distribution and gene expression profile associated with the downregulation of *LOXL3*.

We noted a significant morphological change of U87MG cells after *LOXL3* downregulation, with enlargement of the tumor cell surface. Interestingly, the transcriptomic analysis of *LOXL3*-silenced U87MG cells showed an upregulation of genes involved in cellular focal adhesion and genes coding for cytoskeleton organization.

In fact, genes coding for the intracellular components of the focal adhesion complex and the cytoskeleton, such as *TLN2*, were upregulated with LOXL3 silencing. *TLN2* codes for a key cytoplasmic mediator of integrin adhesion to the ECM [30–32], while the other two genes are related to the regulation of actin filament assembly (*ENAH*) and filament organization (*CCN2*) for the modulation of cell adhesion. Furthermore, genes coding for tubulins, which polymerize into microtubules, a major component of the cell cytoskeleton, were upregulated. Microtubules act as force generators for cell protrusion, and they are involved in intracellular transport [33]. In migratory cells, the microtubule-organizing center is polarized and symmetric in front of the nucleus [34,35]. However, such characteristics were lost in the *LOXL3*-silenced U87MG cells, and a significant decrease in the invasion capacity was demonstrated in these cells. Interestingly, the TCGA RNA-seq dataset analysis demonstrated a significant correlation between the gene expression levels of *LOXL3* and two genes coding for α-tubulin *(TUBA1C*, *TUBA4A*) in the mesenchymal subtype, suggesting a prominent role of LOXL3 in the most aggressive GBM molecular subtype.

Genes related to ECM components were also upregulated following downregulation of *LOXL3*, indicating an increase in the stiffness of the cell microenvironment. Particularly,

the upregulation of collagen genes (*COL5A1*, *COL6A1*, *COL7A1*, *COL27A1*), fibrillins (*FBN1*, *FBN2*), and microfibril-associated glycoproteins (*MFAP2*, *MFAP4*) pointed towards a reinforcement of the ECM microfibrillar mesh. In addition, enzymes that stabilize the cross-linking of collagen fibers, such as *PLOD1*, *PLOD2*, *BMP1*, *LOX*, and *LOXL2*, were upregulated.

Moreover, the upregulation of *FN1*, *TNC*, and plasma membrane components (e.g., *ITGAV* and *SDC4*) indicated the strengthening of the connection between the intracellular focal adhesion complex and ECM components. FN1 interacts with collagens, while ITGAV and SDC4 are associated with focal adhesion formation and FBN1 assembly, thereby contributing to microfiber deposition and subsequent elastic fiber assembly [36–39]. TNC is also involved in the interaction of FN1 and SDC4 [40]. Taken together, these results suggest that the upregulation of constituents of a highly organized elastic microfibrillar ECM provides sites for cell adhesion.

Cellular movement is a continuous and coordinated process that requires the formation and turnover of focal adhesion at the leading edge of the cell body, as well as the release of this attachment at the body and rear of the cell [41]. In fact, the focal adhesion components are continuously recycled during cell motility. Integrins are recycled by endocytosis and exocytosis through clathrin-mediated and CAV-dependent processes [42,43]. *CAV1* and *CAV2*, which code for the major components of the caveolar membrane, are upregulated DEGs. CAV1-dependent endocytosis has also been associated with FN1 turnover and negatively regulates extracellular signal-regulated kinases (i.e., ERK1 and ERK2). Interestingly, LOXL3 silencing led to the downregulation of the MAPK/ERK cascade, which is essential for focal adhesion disassembly through the FAK–paxillin complex [44–46]. In our LOXL3-siRNA experiment, the expression levels of paxillin were not altered. Future studies are warranted to investigate its activation through phosphorylation. Collectively, the upregulated genes after *LOXL3* silencing corroborate the observed U87MG phenotype alteration with cell spreading, increased cellular adhesion, and decreased tumor cell invasion.

Several other genes associated with the following different steps of protein recycling by endocytic trafficking and protein degradation were also downregulated in response to the silencing of *LOXL3* expression:

(1) The early step of endosomal vesicle formation (i.e., *TRAF6* and *SCAMP1*);
(2) Retrograde transport of proteins from the endosome to the trans-Golgi network (i.e., vacuolar protein sorting (*VPS25*, *VPS36*) members of the ESCRT-II complex);
(3) Endosome recycling, involving members of the RAS oncogene family (i.e., *RAB3D*, *RAB22A*);
(4) Endosome fusion to the lysosome, associated with phosphoinositide kinase (i.e., *PIKFYVE*);
(5) Maintenance of the lysosome membrane (i.e., *ATP6V1C1*, *ATP6V1B2*);
(6) Chaperone-mediated autophagy by lysosomal translocation for protein degradation (i.e., *HSPA8*).

These results may indicate that cell adhesion complex turnover through endosome vesicle trafficking, recycling, and protein degradation by the Golgi and lysosome pathways were suppressed after *LOXL3* silencing. Moreover, dysfunctional protein recycling and degradation systems may lead to the accumulation of autophagosomes and late endosomes, thereby affecting cell viability and inducing autophagy-dependent cell death [47,48].

The downregulation of the MAPK/ERK cascade may also be involved in focal adhesion disassembly through dysregulation of endosomal dynamics [49]. In fact, the expression levels of *MAPK1* (also termed ERK2), *STK38*, and *MAPK8IP1* were downregulated upon *LOXL3* silencing. These genes are related to cell growth and survival by regulation of transcription, translation, and cytoskeletal rearrangements. Upon cell detachment, STK38 is necessary for the clearance of damaged mitochondria, prevention of an increase in the levels of reactive oxygen species, and protection of cancer cells [50,51]. Moreover, STK38 regulates MYC turnover, thus extending the MYC half-life [52]. Similarly, JNK-interacting protein 1 (JIP1, also termed MAPK8IP1) is involved in JNK regulation and, consequently,

in the stabilization of c-MYC protein [53,54]. Furthermore, *MAPK8IP1* is also involved in autophagosome trafficking [55], which has an impact on cell proliferation and survival. Thus, the downregulated gene expression profile of our study might be associated with the increased cell adhesion, decreased cell viability, and increased early-phase apoptosis observed in *LOXL3*-silenced U87M cells. However, further studies are necessary to confirm our hypothesis.

GBM is a very heterogeneous tumor, and in addition to the findings in U87MG, a mesenchymal subtype of GBM cell line, we also observed similar morphological change in a less aggressive GBM cell line, T98G. Further, an in-depth analysis of the role of LOXL3 in different molecular subtypes of GBM would be worthwhile to better assess its potential as a therapeutical target.

4. Materials and Methods

4.1. Public Dataset Analyses

LOXL3 mRNA expression data of different types of cancer were downloaded from the cBioPortal for Cancer Genomics (http://www.cbioportal.org, accessed on 22 July 2020) generated by RNA-seq v2 analyses of the Pan-cancer Atlas of TCGA. LOXL3 (ENSG00000115318) and its expression levels obtained by RNA-seq of cell lines from different organs were downloaded from The Human Protein Atlas (HPA) project (https://www.proteinatlas.org/, accessed on 22 July 2020). The HPA data are expressed by normalized expression values, and values ≥ 1 were considered detectable for plotting analysis. LOXL3 expression levels in GBM cases (from TCGA) and normal brain tissues (from Genotype-Tissue Expression (GTEx)), as well as the overall survival of patients with GBM, were investigated using the Gene Expression Profiling Interactive Analysis 2 (GEPIA2) online database [56].

4.2. Cell Culture

The glioma cell lines U87MG and T98G were obtained from the American Type Culture Collection (Manassas, VA, USA). The cells were maintained in Dulbecco's modified Eagle's medium (Thermo Fisher Scientific, Waltham, MA, USA), supplemented with 10% heat-inactivated fetal bovine serum (FBS) (Cultilab, Campinas, Brazil) and antibiotics (100 units/mL penicillin, 100 µg/mL streptomycin), in a humidified atmosphere with 5% CO_2 at 37 °C. Cell line authentication was performed by short tandem repeat DNA analysis with the GenePrint 10 System (Promega, Fitchburg, WI, USA).

4.3. LOXL3 Silencing

Two sequences of small interfering RNA (siRNA) duplexes for LOXL3 knockdown, namely siRNA1 (5′-CGGCATGACATTGACTGTCAGTGGA-3′) and siRNA2 (5′-CTAGTTTCTGTCTCGAAGACACTGA-3′), as well as nontarget control (NTC) siRNA, were synthesized by Integrated DNA Technologies (Coralville, IA, USA). The oligonucleotides were diluted in RNase-free duplex buffer provided by Integrated DNA Technologies. U87MG and T98G cells (1×10^5 cells/well) were seeded in a six-well plate and transfected with Lipofectamine RNAiMax (Thermo Fisher Scientific) after 24 h. The siRNAs for LOXL3 and NTC were used at a final concentration of 10 nM for both U87MG and T98G. LOXL3 knockdown was evaluated at 2, 4, and 7 days after transfection. The mRNA and protein levels were determined by real-time quantitative polymerase chain reaction (RT-qPCR) and Western blotting, respectively.

4.4. RNA Extraction and cDNA Synthesis

Extraction of RNA and DNA was performed using the RNeasy Mini Kit (Qiagen, Valencia, CA, USA) according to the protocol provided by the manufacturer. The concentration and purity of RNA were evaluated using the NanoDrop device (Thermo Fisher Scientific), and values ranging from 1.8 to 2.0 for 260:280 nm absorbance ratio denoted satisfactory purity. For cDNA synthesis, 1 µg of total RNA was required. The Maxima First Strand cDNA Synthesis Kit (Thermo Fisher Scientific) was used for the amplification,

according to the instructions provided by the manufacturer. Finally, cDNA was diluted in Tris/EDTA buffer for analysis by RT-qPCR.

4.5. Gene Expression Analysis

The expression levels of *LOXL3* were analyzed by RT-qPCR performed on the ABI 7500 apparatus (Thermo Fisher Scientific). The primers used in this experiment were synthesized by Integrated DNA Technologies: LOXL3 (forward: CTGGAACAGGCCGCATCT; reverse: CCCCAGCATCCTCATCGT), hypoxanthine phosphoribosyltransferase (HPRT) (forward: TGAGGATTTGGAAAGGGTGT; reverse: GAGCACACAGAGGGCTACAA). These primers were designed to amplify a region containing 80–120 bp. Reactions were performed in triplicate, and the final volume was 12 µL per reaction, containing 3 µL of cDNA, 3 µL of primers (final concentration: 200 nM), and 6 µL of Power SYBR Green PCR Master Mix (Thermo Fisher Scientific). The amplification conditions included an initial incubation for 2 min at 50 °C, 10 min at 95 °C, 40 cycles of 15 s at 95 °C, and 1 min at 60 °C. The expression levels of *LOXL3* were normalized to those of the housekeeping gene HPRT. Single product amplification was confirmed by analyzing the dissociation curves. The amplification efficiencies were calculated using serial cDNA dilutions [57]. Assays were performed in duplicates and in two independent experiments. Additionally, expression levels of *LOXL3* were determined for all transfections with siRNA.

4.6. Western Blotting

Cell protein extracts were obtained using radioimmunoprecipitation assay (Tris-HCl 50 mM, NP-40 1%, Na-deoxycholate 0.25%, NaCl 150 mM, EDTA 1 mM) lysis buffer and a protease inhibitor cocktail (Sigma–Aldrich, St. Louis, MO, USA). Total protein concentrations were determined by the Bradford method. Cell lysates (20 µg of proteins) were separated by 4–12% gradient polyacrylamide gel electrophoresis (Thermo Fisher Scientific) in NuPAGE 3-(N-morpholino)propanesulfonic acid–sodium dodecyl sulfate electrophoresis buffer (Thermo Fisher Scientific) and transferred to a polyvinylidene difluoride membrane using the iBLOT system (Thermo Fisher Scientific). The membrane was incubated with rabbit polyclonal anti-LOXL3 (1:1000; Aviva Antibody Corporation, San Diego, CA, USA) and mouse monoclonal anti-β-actin (1:20,000; Sigma–Aldrich) as control for protein loading. Anti-rabbit and anti-mouse IgG secondary antibodies conjugated to peroxidase (1:1000; Sigma–Aldrich) and the chemiluminescence detection system Clarity Western ECL Blotting Substrate (BioRad Laboratories, Hercules, CA, USA) were used to visualize proteins in the membrane on the ImageQuant LAS4000 apparatus (GE Healthcare, Pittsburgh, PA, USA).

4.7. Immunofluorescence

LOXL3 localization in U87MG cells before and after transfection with siRNA was analyzed by immunofluorescence. Cells were cultured in a monolayer on poly-L-lysine-coated glass coverslips. Cells were fixed with 4% paraformaldehyde. The membrane was permeabilized with 0.1% Triton X-100, and blocking was performed with 4% goat serum. Subsequently, the membrane was incubated with the primary antibody anti-LOXL3 (1:200, Aviva Antibody Corporation) and anti-α-tubulin (1:1000, Abcam, Cambridge, UK) overnight at 37 °C, followed by incubation with the anti-rabbit IgG secondary antibody conjugated to Alexa Fluor 488 and 568 (1:400; Thermo Fisher Scientific) overnight at 4 °C. Actin filaments were stained with phalloidin conjugated to Alexa Fluor 488 (1:400; Thermo Fisher Scientific) overnight at 4 °C. Nuclei were stained with 4′,6-diamidino-2-phenylindole (DAPI; Thermo Fisher Scientific). The preparations were analyzed under Zeiss 510 LSM META and Zeiss 780-NLO confocal microscopes (Carl Zeiss Microscopy, Thornwood, NY, USA). Fluorescence quantification was performed by integrated density via the selection of regions of interest. Measurement of the total area was performed by selection in the regions of interest using bright-field microscopy. ImageJ (National Institutes of Health, Bethesda, MD, USA) software was used to perform the analyses.

4.8. High-Throughput Sequencing for Transcriptome Analysis

RNA-seq libraries were constructed with SureSelect Strand-Specific RNA Library Prep for Illumina Multiplexed Sequencing according to the instructions provided by the manufacturer (Agilent Technologies, Santa Clara, CA, USA). Total RNA of each sample in duplicates was used to prepare the libraries. The mean size of each library was determined on TapeStation 2200 (Agilent Technologies) with D1000 ScreenTape, and quantification was performed by RT-qPCR using Kapa Library Quantification Kit (Kapa Biosystems, Roche, Pleasanton, CA, USA). DNA libraries were pooled and sequenced on a HiSeq 2500 (Illumina, San Diego, CA, USA) with 100 bp pair-ended reads in the SELA Facility Core of School of Medicine, University of Sao Paulo. Sequencing generated an average of 51 million reads per sample. Quality control analysis was performed by FASTQC software [58]. Raw reads were aligned to the hg38 through STAR software [59]. Quantification of the gene expression data was performed using featureCounts software [60]. Data normalization was performed with edgeR software using the trimmed mean method. Expression levels were calculated using two methods: reads per kilobase per million (RPKM) and counts per million [61]. Differential expression analysis was performed using the limma framework [62]. Differentially expressed genes (DEGs; genes differentially expressed in LOXL3-knockdown U87MG cells compared with control NTC cells) were analyzed with WebGestalt (Web-Based Gene Set Analysis Toolkit), using Over-Representation Analysis and the Gene Ontology (GO) functional database [63]. RPKM data of the four samples and those of the differential expression analysis are presented in the Supplementary Material. Additionally, an enrichment map of GO terms was analyzed using the STRING plugin in Cytoscape software [64]. Functional analyses of altered genes related to processes were also performed. RPKM values were transformed to z-scores for heatmap visualization.

4.9. Viability Assay

A total of 1×10^3 U87MG cells/well were seeded in a 96-well plate and transfected with siRNA for LOXL3 and control NTC. The cells were incubated with the PrestoBlue Cell Viability Reagent (Thermo Fisher Scientific) once daily for 4 days. Fluorescence intensity (excitation at 540 nm; emission at 560 nm) was measured using a GloMax-96 Microplate Luminometer (Promega). The background consisting of Dulbecco's modified Eagle's medium with 10% FBS was measured for each plate and subtracted from each measurement value. Assays were performed in octuplicate in three independent experiments.

4.10. Apoptosis Analysis

U87MG cells (5×10^3/well) were seeded in six-well plates and transfected with siRNA for LOXL3 and NTC as previously described. On the second day post-transfection, cells were treated with 1 mM TMZ or control. Cells were labeled on the fourth day with Annexin V-FITC and propidium iodide using the Dead Cell Apoptosis kit (Thermo Fisher Scientific). A total of 30,000 events were acquired for each condition. Detection and quantification of apoptotic cells (siRNA-silenced and control) were performed by flow cytometric analysis (FACS Canto II; BD Biosciences, San Jose, CA, USA). Three independent experiments including duplicate measurements were performed.

4.11. Cell Adhesion and Invasion Analysis

U87MG cells (5×10^3/well) were seeded in six-well plates and transfected with siRNA for LOXL3 and NTC as previously described. On the fourth day post-transfection, Dulbecco's modified Eagle's medium supplemented with 1% FBS was added, and cells were incubated for 2 h. Cells (5×10^4/well) were seeded in 96-well plates and incubated for 3 h at 37 °C in an atmosphere containing 5% CO_2 for the cell adhesion analysis. After three washes with phosphate-buffered saline, the cells were incubated with PrestoBlue Cell Viability Reagent (Thermo Fisher Scientific). The attached cells were quantified by measuring the fluorescence intensity at 525 nm (excitation at 560 nm) using the GloMax-96 Microplate Reader (Promega) [65,66]. Assays were performed in octuplicates in two independent

experiments. Cells (1×10^5/well) were seeded in transwell inserts (8 µm pore size, BD Falcon, Franklin Lakes, NJ, USA) previously prepared with Geltrex (Thermo Fisher Scientific) and rehydrated with 1% FBS for the invasion assay. Cells were seeded and incubated with 1% FBS for 20 h, using 10% FBS as chemoattractant. Invading cells were fixed with 4% paraformaldehyde and stained with 0.2% crystal violet. Invading cells were analyzed by inverted microscopy. Quantification was performed by counting all the invading cells in the inserts. Assays were performed in duplicates in two independent experiments.

4.12. In Silico GBM RNA-Seq Data Analyses

GBM gene expression data from the RNA-seq dataset of The Cancer Genome Atlas (TCGA) were downloaded from Genomics Data Commons Data Portal (https://portal.gdc.cancer.gov/, accessed on November 2017) and normalized by DEseq R software. Normalized read counts were converted to a z-score for heatmap visualization.

4.13. Statistical Analyses

For gene expression, colocalization through fluorescence intensity, cell viability, and apoptosis assays, the two-way analysis of variance test was used to compare multiple groups, followed by Tukey's post hoc test. Student's t-test was used to compare the groups for fluorescence quantification, cell adhesion, cell invasion, and the total surface area of cell assays. Correlation analyses between gene expression values were assessed by the nonparametric Spearman's rho correlation test. Normality testing was performed using the Kolmogorov–Smirnov test. SPSS version 20.0 (IBM Corporation, Armonk, NY, USA) and GraphPad Prism 8 (GraphPad Software, San Diego, CA, USA) were used for statistical analysis. A p-value < 0.05 denoted statistical significance.

5. Conclusions

In summary, the DEG profile induced by LOXL3 silencing was associated with increased cell attachment, ECM stiffness, decreased cell invasion, and dysfunctional endosomal dynamics preventing cell motility. This finding suggested that dysregulation of LOXL3 interrupted the energy source needed to maintain cellular focal adhesion in sprawling tumor cells. Tumor cell invasiveness is a major characteristic of GBM. Hence, lowering LOXL3 expression may increase tumor resectability and decrease the rate of tumor recurrence, thereby improving the outcomes of patients with GBM.

Supplementary Materials: The following are available online at https://www.mdpi.com/article/10.3390/ijms22158072/s1.

Author Contributions: T.d.S.L., S.K.N.M., and S.M.O.-S. conceptualized the study. T.d.S.L. and R.d.S.S. performed the experiments and the interpretation and analysis of data. S.K.N.M. and S.M.O.-S. supervised the work. A.M.L. analyzed the next-generation sequencing data. T.d.S.L. and S.M.O.-S. wrote the original draft of the manuscript. All authors revised the content and approved the final version of the manuscript.

Funding: This research was supported by Conselho Nacional de Pesquisa (CNPq), grant 140482/2020-2; Sao Paulo Research Foundation (FAPESP, grants #2015/03614-5, #2016/05777-1, #2020/02988-9); Fundação Faculdade de Medicina (FFM); and Faculdade de Medicina da USP (FMUSP).

Institutional Review Board Statement: Not applicable.

Informed Consent Statement: Not applicable.

Acknowledgments: The authors thank the SELA Facility Core of School of Medicine, University of Sao Paulo (Fapesp grant #2014/50137-5), for assistance with sequencing.

Conflicts of Interest: The authors declare that the research was conducted in the absence of any commercial or financial relationships that could be construed as a potential conflict of interest.

References

1. Ostrom, Q.T.; Gittleman, H.; Truitt, G.; Boscia, A.; Kruchko, C.; Barnholtz-Sloan, J.S. CBTRUS Statistical Report: Primary Brain and Other Central Nervous System Tumors Diagnosed in the United States in 2011–2015. *Neuro. Oncol.* **2018**, *20* (Suppl. 4), iv1–iv86. [CrossRef]
2. Nørøxe, D.S.; Poulsen, H.S.; Lassen, U. Hallmarks of glioblastoma: A systematic review. *ESMO Open* **2016**, *1*, e000144. [CrossRef]
3. Louis, D.N.; Perry, A.; Reifenberger, G.; von Deimling, A.; Figarella-Branger, D.; Cavenee, W.K.; Ohgaki, H.; Wiestler, O.D.; Kleihues, P.; Ellison, D.W. The 2016 World Health Organization Classification of Tumors of the Central Nervous System: A summary. *Acta Neuropathol.* **2016**, *131*, 803–820. [CrossRef]
4. Wang, Q.; Hu, B.; Hu, X.; Kim, H.; Squatrito, M.; Scarpace, L.; de Carvalho, A.C.; Lyu, S.; Li, P.; Li, Y.; et al. Tumor Evolution of Glioma-Intrinsic Gene Expression Subtypes Associates with Immunological Changes in the Microenvironment. *Cancer Cell* **2017**, *32*, 42–56.e6. [CrossRef]
5. Verhaak, R.G.; Hoadley, K.A.; Purdom, E.; Wang, V.; Qi, Y.; Wilkerson, M.D.; Miller, C.R.; Ding, L.; Golub, T.; Mesirov, J.P.; et al. An integrated genomic analysis identifies clinically relevant subtypes of glioblastoma characterized by abnormalities in PDGFRA, IDH1, EGFR and NF1. *Cancer Cell* **2010**, *17*, 98. [CrossRef]
6. Alifieris, C.; Trafalis, D.T. Glioblastoma multiforme: Pathogenesis and treatment. *Pharmacol. Ther.* **2015**, *152*, 63–82. [CrossRef] [PubMed]
7. Barker, H.E.; Cox, T.R.; Erler, J.T. The rationale for targeting the LOX family in cancer. *Nat. Rev. Cancer* **2012**, *12*, 540–552. [CrossRef]
8. Mayorca-Guiliani, A.; Erler, J.T. The potential for targeting extracellular LOX proteins in human malignancy. *OncoTargets Ther.* **2013**, *6*, 1729–1735.
9. Grau-Bové, X.; Ruiz-Trillo, I.; Rodriguez-Pascual, F. Origin and evolution of lysyl oxidases. *Sci. Rep.* **2015**, *5*, 10568. [CrossRef] [PubMed]
10. Laurentino, T.d.S.; Soares, R.d.S.; Marie, S.K.N.; Oba-Shinjo, S.M. LOXL3 Function Beyond Amino Oxidase and Role in Pathologies, Including Cancer. *Int. J. Mol. Sci.* **2019**, *20*, 3587. [CrossRef] [PubMed]
11. Jourdan-Le Saux, C.; Tomsche, A.; Ujfalusi, A.; Jia, L.; Csiszar, K. Central nervous system, uterus, heart, and leukocyte expression of the LOXL3 gene, encoding a novel lysyl oxidase-like protein. *Genomics* **2001**, *74*, 211–218. [CrossRef]
12. Zhou, L.; Chen, B.; Hua, X.; Zhou, P.; Guo, L.; Peng, Y.; Qiu, K. Effect of newly identified hTERT-interacting proteins on telomerase activity. *Acta Biochim. Biophys. Sin.* **2013**, *45*, 674–682. [CrossRef]
13. Kasashima, H.; Yashiro, M.; Okuno, T.; Miki, Y.; Kitayama, K.; Masuda, G.; Kinoshita, H.; Morisaki, T.; Fukuoka, T.; Hasegawa, T.; et al. Significance of the Lysyl Oxidase Members Lysyl Oxidase Like 1, 3, and 4 in Gastric Cancer. *Digestion* **2018**, *98*, 238–248. [CrossRef]
14. Mäki, J.M.; Kivirikko, K.I. Cloning and characterization of a fourth human lysyl oxidase isoenzyme. *Biochem. J.* **2001**, *355 Pt 2*, 381–387. [CrossRef]
15. Kraft-Sheleg, O.; Zaffryar-Eilot, S.; Genin, O.; Yaseen, W.; Soueid-Baumgarten, S.; Kessler, O.; Smolkin, T.; Akiri, G.; Neufeld, G.; Cinnamon, Y.; et al. Localized LoxL3-Dependent Fibronectin Oxidation Regulates Myofiber Stretch and Integrin-Mediated Adhesion. *Dev. Cell* **2016**, *36*, 550–561. [CrossRef] [PubMed]
16. Ma, L.; Huang, C.; Wang, X.J.; Xin, D.E.; Wang, L.S.; Zou, Q.L.C.; Zhang, Y.N.S.; Tan, M.D.; Wang, Y.M.; Zhao, T.C.; et al. Lysyl Oxidase 3 Is a Dual-Specificity Enzyme Involved in STAT3 Deacetylation and Deacetylimination Modulation. *Mol. Cell* **2017**, *65*, 296–309. [CrossRef] [PubMed]
17. Peinado, H.; Del Carmen Iglesias-de la Cruz, M.; Olmeda, D.; Csiszar, K.; Fong, K.S.; Vega, S.; Nieto, M.A.; Cano, A.; Portillo, F. A molecular role for lysyl oxidase-like 2 enzyme in snail regulation and tumor progression. *EMBO J.* **2005**, *24*, 3446–3458. [CrossRef]
18. Santamaria, P.G.; Floristan, A.; Fontanals-Cirera, B.; Vazquez-Naharro, A.; Santos, V.; Morales, S.; Yuste, L.; Peinado, H.; Garcia-Gomez, A.; Portillo, F.; et al. Lysyl oxidase-like 3 is required for melanoma cell survival by maintaining genomic stability. *Cell Death Differ.* **2018**, *25*, 935–950. [CrossRef] [PubMed]
19. Sebban, S.; Davidson, B.; Reich, R. Lysyl oxidase-like 4 is alternatively spliced in an anatomic site-specific manner in tumors involving the serosal cavities. *Virchows Arch.* **2009**, *454*, 71–79. [CrossRef] [PubMed]
20. Tadmor, T.; Bejar, J.; Attias, D.; Mischenko, E.; Sabo, E.; Neufeld, G.; Vadasz, Z. The expression of lysyl-oxidase gene family members in myeloproliferative neoplasms. *Am. J. Hematol.* **2013**, *88*, 355–358. [CrossRef]
21. Dufresne, J.; Bowden, P.; Thavarajah, T.; Florentinus-Mefailoski, A.; Chen, Z.Z.; Tucholska, M.; Norzin, T.; Ho, M.T.; Phan, M.; Mohamed, N.; et al. The plasma peptides of ovarian cancer. *Clin. Proteom.* **2018**, *15*, 41. [CrossRef]
22. Barbazan, J.; Muinelo-Romay, L.; Vieito, M.; Candamio, S.; Diaz-Lopez, A.; Cano, A.; Gomez-Tato, A.; de Cal, M.D.C.; Abal, M.; Lopez-Lopez, R. A multimarker panel for circulating tumor cells detection predicts patient outcome and therapy response in metastatic colorectal cancer. *Int. J. Cancer* **2014**, *135*, 2633–2643. [CrossRef] [PubMed]
23. Zhang, J.; Liu, Z.; Zhang, T.; Lin, Z.; Li, Z.; Zhang, A.; Sun, X.; Gao, J. Loss of Lysyl Oxidase-like 3 Attenuates Embryonic Lung Development in Mice. *Sci. Rep.* **2016**, *6*, 33856. [CrossRef]
24. Zhang, J.; Yang, R.; Liu, Z.; Hou, C.; Zong, W.; Zhang, A.; Sun, X.; Gao, J. Loss of lysyl oxidase-like 3 causes cleft palate and spinal deformity in mice. *Hum. Mol. Genet.* **2015**, *24*, 6174–6185. [CrossRef] [PubMed]
25. Chan, T.K.; Alkaabi, M.K.; ElBarky, A.M.; El-Hattab, A.W. LOXL3 novel mutation causing a rare form of autosomal recessive Stickler syndrome. *Clin. Genet.* **2019**, *95*, 325–328. [CrossRef] [PubMed]

26. Alzahrani, F.; Al Hazzaa, S.A.; Tayeb, H.; Alkuraya, F.S. LOXL3, encoding lysyl oxidase-like 3, is mutated in a family with autosomal recessive Stickler syndrome. *Hum. Genet.* **2015**, *134*, 451–453. [CrossRef]
27. Jones, M.G.; Andriotis, O.G.; Roberts, J.J.; Lunn, K.; Tear, V.J.; Cao, L.; Ask, K.; Smart, D.E.; Bonfanti, A.; Johnson, P.; et al. Nanoscale dysregulation of collagen structure-function disrupts mechano-homeostasis and mediates pulmonary fibrosis. *Elife* **2018**, *7*, 7. [CrossRef] [PubMed]
28. Ye, M.; Song, Y.; Pan, S.; Chu, M.; Wang, Z.; Zhu, X. Evolving roles of lysyl oxidase family in tumorigenesis and cancer therapy. *Pharmacol. Ther.* **2020**, *215*, 107633. [CrossRef]
29. Eiseler, T.; Köhler, C.; Nimmagadda, S.C.; Jamali, A.; Funk, N.; Joodi, G.; Storz, P.; Seufferlein, T. Protein Kinase D1 Mediates Anchorage-dependent and -independent Growth of Tumor Cells via the Zinc Finger Transcription Factor Snail1*. *J. Biol. Chem.* **2012**, *287*, 32367–32380. [CrossRef]
30. Calderwood, D.A.; Zent, R.; Grant, R.; Rees, D.J.; Hynes, R.O.; Ginsberg, M.H. The Talin head domain binds to integrin beta subunit cytoplasmic tails and regulates integrin activation. *J. Biol. Chem.* **1999**, *274*, 28071–28074. [CrossRef]
31. Yuan, Y.; Li, L.; Zhu, Y.; Qi, L.; Azizi, L.; Hytönen, V.P.; Zhan, C.G.; Huang, C. The molecular basis of talin2's high affinity toward β1-integrin. *Sci. Rep.* **2017**, *7*, 1–12. [CrossRef]
32. Cluzel, C.; Saltel, F.; Lussi, J.; Paulhe, F.; Imhof, B.A.; Wehrle-Haller, B. The mechanisms and dynamics of αvβ3 integrin clustering in living cells. *J. Cell Biol.* **2005**, *171*, 383–392. [CrossRef] [PubMed]
33. Meiring, J.C.M.; Shneyer, B.I.A.A. Generation and regulation of microtubule network asymmetry to drive cell polarity. *Curr. Opin. Cell Biol.* **2020**, *62*, 86–95. [CrossRef]
34. Garcin, C.; Straube, A. Microtubules in cell migration. *Essays Biochem.* **2019**, *63*, 509–520.
35. Etienne-Manneville, S. Polarity proteins in migration and invasion. *Oncogene* **2008**, *27*, 6980. [CrossRef] [PubMed]
36. Yamashita, H.; Goto, A.; Kadowaki, T.; Kitagawa, Y. Mammalian and Drosophila cells adhere to the laminin α4 LG4 domain through syndecans, but not glypicans. *Biochem. J.* **2004**, *382*, 933–943. [CrossRef] [PubMed]
37. Zeyer, K.A.; Reinhardt, D.P. Fibrillin-containing microfibrils are key signal relay stations for cell function. *J. Cell Commun. Signal.* **2015**, *9*, 309–325. [CrossRef] [PubMed]
38. Bharadwaj, M.; Strohmeyer, N.; Colo, G.P.; Helenius, J.; Beerenwinkel, N.; Schiller, H.B.; Fässler, R.; Müller, D.J. αV-class integrins exert dual roles on α5β1 integrins to strengthen adhesion to fibronectin. *Nat. Commun.* **2017**, *8*, 14348. [CrossRef]
39. Godwin, A.R.F.; Singh, M.; Lockhart-Cairns, M.P.; Alanazi, Y.F.; Cain, S.A.; Baldock, C. The role of fibrillin and microfibril binding proteins in elastin and elastic fibre assembly. *Matrix Biol.* **2019**, *84*, 17–30. [CrossRef]
40. Orend, G.; Huang, W.; Olayioye, M.A.; Hynes, N.E.; Chiquet-Ehrismann, R. Tenascin-C blocks cell-cycle progression of anchorage-dependent fibroblasts on fibronectin through inhibition of syndecan-4. *Oncogene* **2003**, *22*, 3917–3926. [CrossRef] [PubMed]
41. Broussard, J.A.; Webb, D.J.; Kaverina, I. Asymmetric focal adhesion disassembly in motile cells. *Curr. Opin. Cell Biol.* **2008**, *20*, 85–90. [CrossRef] [PubMed]
42. Ezratty, E.J.; Bertaux, C.; Marcantonio, E.E.; Gundersen, G.G. Clathrin mediates integrin endocytosis for focal adhesion disassembly in migrating cells. *J. Cell Biol.* **2009**, *187*, 733–747. [CrossRef] [PubMed]
43. Moreno-Layseca, P.; Icha, J.; Hamidi, H.; Ivaska, J. Integrin trafficking in cells and tissues. *Nat. Cell Biol.* **2019**, *21*, 122–132. [CrossRef]
44. Webb, D.J.; Parsons, J.T.; Horwitz, A.F. Adhesion assembly, disassembly and turnover in migrating cells—Over and over and over again. *Nat. Cell Biol.* **2002**, *4*, E97–E100. [CrossRef]
45. López-Colomé, A.M.; Lee-Rivera, I.; Benavides-Hidalgo, R.; López, E. Paxillin: A crossroad in pathological cell migration. *J. Hematol. Oncol.* **2017**, *10*, 1–15. [CrossRef]
46. Ishibe, S.; Joly, D.; Liu, Z.X.; Cantley, L.G. Paxillin serves as an ERK-regulated scaffold for coordinating FAK and Rac activation in epithelial morphogenesis. *Mol. Cell* **2004**, *16*, 257–267. [CrossRef] [PubMed]
47. Bialik, S.; Dasari, S.K.; Kimchi, A. Autophagy-dependent cell death—Where, how and why a cell eats itself to death. *J. Cell Sci.* **2018**, *131*, jcs215152. [CrossRef] [PubMed]
48. Liu, Y.; Shoji-Kawata, S.; Sumpter, R.M.; Wei, Y.; Ginet, V.; Zhang, L.; Posner, B.; Tran, K.A.; Green, D.R.; Xavier, R.J.; et al. Autosis is a Na+,K+-ATPase-regulated form of cell death triggered by autophagy-inducing peptides, starvation, and hypoxia-ischemia. *Proc. Natl. Acad. Sci. USA* **2013**, *110*, 20364–20371. [CrossRef] [PubMed]
49. Tanimura, S.; Takeda, K. ERK signalling as a regulator of cell motility. *J. Biochem.* **2017**, *162*, 145–154. [CrossRef]
50. Joffre, C.; Codogno, P.; Fanto, M.; Hergovich, A.; Camonis, J. STK38 at the crossroad between autophagy and apoptosis. *Autophagy* **2016**, *12*, 594–595. [CrossRef]
51. Bettoun, A.; Joffre, C.; Zago, G.; Surdez, D.; Vallerand, D.; Gundogdu, R.; Sharif, A.A.; Gomez, M.; Cascone, I.; Meunier, B.; et al. Mitochondrial clearance by the STK38 kinase supports oncogenic Ras-induced cell transformation. *Oncotarget* **2016**, *7*, 44142–44160. [CrossRef] [PubMed]
52. Bisikirska, B.C.; Adam, S.J.; Alvarez, M.J.; Rajbhandari, P.; Cox, R.; Lefebvre, C.; Wang, K.; Rieckhof, G.E.; Felsher, D.W.; Califano, A. STK38 is a critical upstream regulator of MYC's oncogenic activity in human B-cell lymphoma. *Oncogene* **2013**, *32*, 5283–5291. [CrossRef] [PubMed]
53. Morrison, D.K.; Davis, R.J. Regulation of MAP kinase signaling modules by scaffold proteins in mammals. *Annu. Rev. Cell Dev. Biol.* **2003**, *19*, 91–118. [CrossRef]

54. Alarcon-Vargas, D.; Ronai, Z. c-Jun-NH2 kinase(JNK) contributes to the regulation of c-Myc protein stability. *J. Biol. Chem.* **2004**, *279*, 5008–5016. [CrossRef] [PubMed]
55. Fu, M.M.; Holzbaur, E.L. MAPK8IP1/JIP1 regulates the trafficking of autophagosomes in neurons. *Autophagy* **2014**, *10*, 2079–2081. [CrossRef]
56. Tang, Z.; Kang, B.; Li, C.; Chen, T.; Zhang, Z. GEPIA2: An enhanced web server for large-scale expression profiling and interactive analysis. *Nucleic Acids Res.* **2019**, *47*, W556–W560. [CrossRef] [PubMed]
57. Livak, K.J.; Schmittgen, T.D. Analysis of relative gene expression data using real-time quantitative PCR and the 2(-Delta Delta C(T)) Method. *Methods* **2001**, *25*, 402–408. [CrossRef]
58. Spinozzi, G.; Tini, V.; Adorni, A.; Falini, B.; Martelli, M.P. ARPIR: Automatic RNA-Seq pipelines with interactive report. *BMC Bioinform.* **2020**, *21*, 1–14. [CrossRef]
59. Dobin, A.; Davis, C.A.; Schlesinger, F.; Drenkow, J.; Zaleski, C.; Jha, S.; Batut, P.; Chaisson, M.; Gingeras, T.R. STAR: Ultrafast universal RNA-seq aligner. *Bioinformatics* **2013**, *29*, 15–21. [CrossRef]
60. Li, B.; Dewey, C.N. RSEM: Accurate transcript quantification from RNA-Seq data with or without a reference genome. *BMC Bioinform.* **2011**, *12*, 323. [CrossRef] [PubMed]
61. Wagner, G.P.; Kin, K.; Lynch, V.J. Measurement of mRNA abundance using RNA-seq data: RPKM measure is inconsistent among samples. *Theory Biosci.* **2012**, *131*, 281–285. [CrossRef]
62. Ritchie, M.E.; Phipson, B.; Wu, D.; Hu, Y.; Law, C.W.; Shi, W.; Smyth, G.K. limma powers differential expression analyses for RNA-sequencing and microarray studies. *Nucleic Acids Res.* **2015**, *43*, e47. [CrossRef] [PubMed]
63. Liao, Y.; Wang, J.; Jaehnig, E.J.; Shi, Z.; Zhang, B. WebGestalt 2019: Gene set analysis toolkit with revamped UIs and APIs. *Nucleic Acids Res.* **2019**, *47*, W199–W205. [CrossRef] [PubMed]
64. Bindea, G.; Mlecnik, B.; Hackl, H.; Charoentong, P.; Tosolini, M.; Kirilovsky, A.; Fridman, W.H.; Pagès, F.; Trajanoski, Z.; Galon, J. ClueGO: A Cytoscape plug-in to decipher functionally grouped gene ontology and pathway annotation networks. *Bioinformatics* **2009**, *25*, 1091–1093. [CrossRef] [PubMed]
65. Humphries, M.J. Cell-substrate adhesion assays. In *Current Protocols in Cell Biology*; J. Wiley: New York, NY, USA, 2001; Chapter 9, Unit 9.1. [CrossRef]
66. Chen, Y.; Lu, B.; Yang, Q.; Fearns, C.; Yates, J.R.; Lee, J.D. Combined integrin phosphoproteomic analyses and small interfering RNA–based functional screening identify key regulators for cancer cell adhesion and migration. *Cancer Res.* **2009**, *69*, 3713–3720. [CrossRef] [PubMed]

Publicação 2

Correlation of Matrisome-Associatted Gene Expressions with LOX Family Members in Astrocytomas Stratified by IDH Mutation Status

5 Publicação 2 – Correlation of Matrisome-Associatted Gene Expressions with LOX Family Members in Astrocytomas Stratified by IDH Mutation Status

Objetivo geral: Analisar os níveis de expressão dos membros da família *LOX* e genes relacionados a MEC em astrocitomas estratificados de acordo com o grau de malignidade e status mutacional de *IDH*.

Para fins de análises, a casuística foi dividida em gliomas de baixo grau (LGG) que incluiu tumores astrocíticos difusos graus 2 e 3, estratificado em *IDH* mutante e selvagem. E casos de GBM com e sem mutação de *IDH*.

a) Avaliar a expressão dos membros da família *LOX* nos diferentes graus de astrocitomas, estratificados em *IDH* mutante e selvagem *in silico*.
b) Analisar a expressão proteica dos membros da família LOX por imunoistoquímica nos diferentes graus de astrocitoma estratificados em *IDH* mutante e selvagem, e avaliar o impacto da expressão na sobrevida livre de doença e total em LGG e GBM, respectivamente.
c) Analisar *in silico* a expressão dos genes que codificam proteínas da MEC e fatores de transcrição mecanosensitivos e correlação com os genes que codificam os membros da família LOX.

International Journal of
Molecular Sciences

MDPI

Article

Correlation of Matrisome-Associatted Gene Expressions with LOX Family Members in Astrocytomas Stratified by IDH Mutation Status

Talita de Sousa Laurentino *, Roseli da Silva Soares, Suely Kazue Nagahashi Marie and Sueli Mieko Oba-Shinjo *

Cellular and Molecular Biology Laboratory (LIM 15), Neurology Department, Faculdade de Medicina (FMUSP), Universidade de Sao Paulo, Sao Paulo 01246-903, SP, Brazil
* Correspondence: talitalaurentino@usp.br (T.d.S.L.); suelimoba@usp.br (S.M.O.-S.); Tel.: +55-11-3061-8310 (S.M.O.-S.)

Abstract: Tumor cell infiltrative ability into surrounding brain tissue is a characteristic of diffusely infiltrative astrocytoma and is strongly associated with extracellular matrix (ECM) stiffness. Collagens are the most abundant ECM scaffolding proteins and contribute to matrix organization and stiffness. LOX family members, copper-dependent amine oxidases, participate in the collagen and elastin crosslinking that determine ECM tensile strength. Common IDH mutations in lower-grade gliomas (LGG) impact prognosis and have been associated with ECM stiffness. We analyzed the expression levels of LOX family members and matrisome-associated genes in astrocytoma stratified by malignancy grade and IDH mutation status. A progressive increase in expression of all five LOX family members according to malignancy grade was found. *LOX*, *LOXL1*, and *LOXL3* expression correlated with matrisome gene expressions. LOXL1 correlations were detected in LGG with *IDH* mutation (IDH^{mut}), *LOXL3* correlations in LGG with IDH wild type (IDH^{wt}) and strong *LOX* correlations in glioblastoma (GBM) were found. These increasing correlations may explain the increment of ECM stiffness and tumor aggressiveness from LGG-IDH^{mut} and LGG-IDH^{wt} through to GBM. The expression of the mechanosensitive transcription factor, β-catenin, also increased with malignancy grade and was correlated with *LOXL1* and LOXL3 expression, suggesting involvement of this factor in the outside–in signaling pathway.

Keywords: lysyl oxidase; matrisome; glioblastoma; diffuse astrocytic; progression; LOX; LOXL1; LOXL3; extracellular matrix

check for updates

Citation: Laurentino, T.d.S.; Soares, R.d.S.; Marie, S.K.N.; Oba-Shinjo, S.M. Correlation of Matrisome-Associatted Gene Expressions with LOX Family Members in Astrocytomas Stratified by IDH Mutation Status. *Int. J. Mol. Sci.* **2022**, *23*, 9507. https://doi.org/10.3390/ijms23179507

Academic Editor: Philip C. Trackman

Received: 11 June 2022
Accepted: 16 August 2022
Published: 23 August 2022

Publisher's Note: MDPI stays neutral with regard to jurisdictional claims in published maps and institutional affiliations.

Copyright: © 2022 by the authors. Licensee MDPI, Basel, Switzerland. This article is an open access article distributed under the terms and conditions of the Creative Commons Attribution (CC BY) license (https://creativecommons.org/licenses/by/4.0/).

1. Introduction

Invasiveness, the infiltrative capacity of tumor cells into surrounding tissue, is a major characteristic of gliomas that prevents complete tumor resection, leads to inexorable tumor recurrence, and confers poor clinical outcome. Tumor extracellular matrix (ECM) stiffness has emerged as a physical hallmark of cancer that, contributes to cancer initiation, progression, metastasis and metabolic reprogramming [1,2], and resistance to drug and radiation therapy [3]. The ECM, also known as the matrisome, is composed of a complex cross-linked meshwork of over 1000 core matrisomes, including ECM glycoproteins, proteoglycans, and collagens, besides matrisome-associated proteins, including ECM-affiliated proteins, ECM regulators, and secreted factors. Collagens are the most abundant ECM scaffolding proteins and contribute to ECM organization and stiffness through crosslinking mediated by lysyl oxidase (LOX) family members [4,5]. This family comprises five cooper-dependent amine oxidases (LOX, LOXL1, LOXL2, LOXL3, and LOXL4) [6,7], which are involved in several hallmarks of cancers [8–10], such as tumor microenvironment remodeling, invasion/migration [11–13], growth [14–16], inflammatory response [17–19], genomic stability [20], and resistance to chemotherapy [21,22].

Astrocytomas, or astrocytic gliomas, are the most common brain tumor. These tumors are classified according to their histologic and molecular characteristics and, more recently, according to isocitrate dehydrogenase (IDH) mutation status, where the presence of this mutation confers a more favorable prognosis [23]. Low-grade astrocytic gliomas (LGG), encompassing grades 2 and 3, are more well-differentiated, slower-growing tumors than grade 4 glioblastoma (GBM), with a median overall survival (OS) of 15 months [24]. Therefore, tumor aggressiveness progressively increases from LGG with IDH mutation (LGG-IDH^{mut}) to LGG with IDH wild type (LGG-IDH^{wt}), through to GBM. Tumor recurrence occurs independently of other factors, but time to recurrence varies according to malignancy grade and IDH mutational status, proving shorter in IDH^{wt} than IDH^{mut} tumors [25]. A growing body of evidence indicates that denser ECM leads to more aggressive tumor progression. Recently, an association between ECM stiffness oscillation and IDH mutation status was established [26].

Our group has previously reported a correlation between increased LOX expression and higher malignancy grade in human astrocytomas, and also a correlation of LOX expression with *IDH1* mutation status [27]. In the present study, the expression of the other members of the LOX family in astrocytomas, stratified by malignancy grade and IDH mutation status, was explored. The differentially expressed LOX member genes were subsequently correlated with matrisome-associated gene expression in LGG-IDH^{mut}, LGG-IDH^{wt}, and GBM groups. Additionally, a search for mechanosensitive transcriptional factors, whose expression correlated with the group of differentially expressed genes, was performed. The study objective was to identify the LOX family members, along with matrisome components, that impact astrocytoma ECM stiffness. This knowledge can help identify LGG-IDH^{wt} that are more prone to tumor progression, together with new candidates for interventions aimed at reducing tumor invasiveness.

2. Results

2.1. LOX Family Expression Levels in Different Malignant Grades of Astrocytomas

Gene expression analysis by quantitative real-time PCR (RT-qPCR) for *LOX*, *LOXL1*, *LOXL2*, *LOXL3*, and *LOXL4* showed increased expression levels in astrocytoma samples compared to non-neoplastic (NN) samples. Moreover, these expressions increased with malignancy, proving the highest in GBM. Pairwise comparisons of NN samples and diffusely infiltrative astrocytoma grades 2, 3, and 4 (AG2, AG3, and GBM, respectively) were significant ($p < 0.0001$) for all five LOX family genes. The paired comparisons relative to GBM were also significant, except for the LOXL3-AG3 comparison (Figure 1A). The results for this cohort were confirmed in an independent larger cohort of The Cancer Genome Atlas (TCGA) and Genotype-Tissue Expression (GTEx), showing significant differences among groups for the five genes analyzed ($p < 0.0001$), with the highest significance found in the paired comparisons with GBM (Figure 1B). Expression profiles of *LOX*, *LOXL1*, *LOXL2*, *LOXL3*, and *LOXL4* in the TCGA cohort were also evaluated in low grade astrocytic glioma (LGG), encompassing AG2 and AG3, according to IDH mutation status and for GBM cases (Figure 1C). Gene expression levels were higher in LGG-IDH^{wt} than in LGG-IDH^{mut} for all genes except *LOXL2*. Comparisons for the LGG-IDH^{wt}-GBM pair showed significant differences for all members of the LOX family, with higher expression in GBM, except for LOXL4. Significant *LOX*, *LOXL1*, and *LOXL3* differential expressions were observed in both LGG-IDH^{mut} vs. LGG-IDH^{wt} and LGG-IDH^{wt} vs. GBM comparisons. Therefore, these three genes were selected for further analysis.

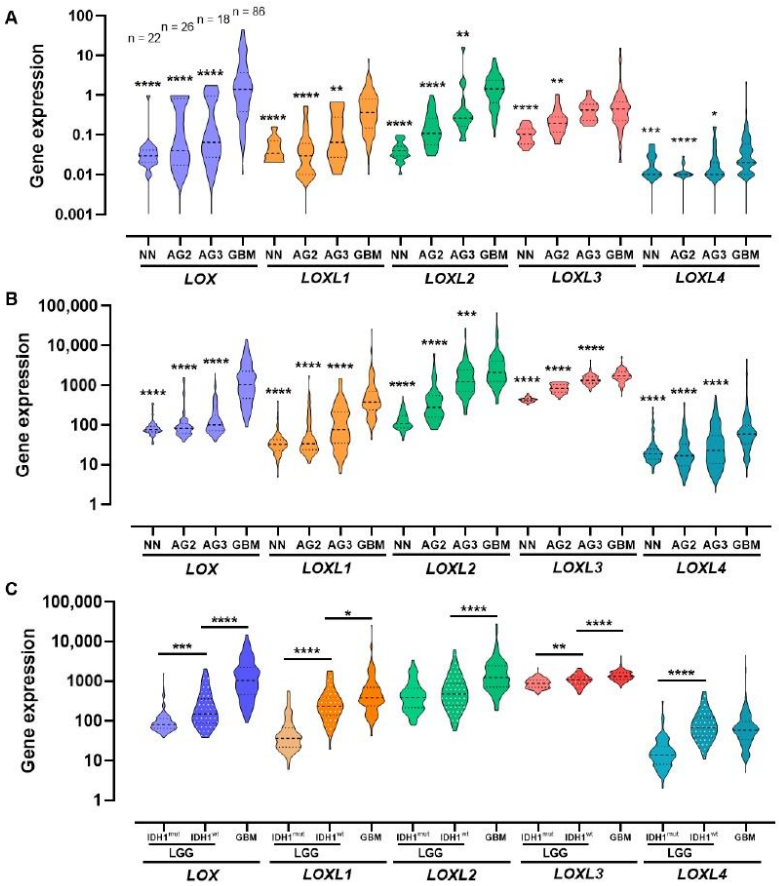

Figure 1. Violin plots showing expression distribution of genes coding for lysyl oxidase family in astrocytomas of different malignancy grades and non-neoplastic brain tissue. (**A**) Expression levels of LOX and LOXL1–4 in cohort determined by RT-qPCR. Statistical analysis was relative to GBM samples. The number of cases in each group is presented in the top of figure. (**B**) Expression levels of *LOX* and *LOXL1–4* in TCGA (astrocytoma groups) and GTEx (NN samples) RNAseq database. Expression increased with malignancy grade of astrocytomas for the four genes analyzed. Statistical analysis was relative to GBM cases. (**C**) Expression levels of *LOX* and *LOXL1–4* in TCGA RNAseq database, for LGG (AG2 and AG3) with (IDH^{mut}) and without (IDH^{wt}) IDH mutation, and GBM cases. Differences were statistically significant ($p < 0.0001$) as determined by Kruskal–Wallis test for all groups of genes in both cohorts. Middle lines represent median of groups. Top and the bottom lines represent first and third quartiles, respectively. The post-hoc Dunn's multiple comparison test was used to calculate differences between two groups (* $p < 0.05$; ** $p < 0.01$; *** $p < 0.001$; **** $p < 0.0001$). Abbreviations: AG2, low-grade astrocytoma; AG3, anaplastic astrocytoma; GBM, glioblastoma; GTEx, Genotype-Tissue Expression; IDH^{mut}, isocitrate dehydrogenase gene with mutation; IDH^{wt}, isocitrate dehydrogenase gene wild type; LGG, lower-grade astrocytic gliomas; NN, non-neoplastic; RT-qPCR, real-time quantitative polymerase chain reaction; TCGA, The Cancer Genome Atlas.

2.2. LOX, LOXL1, and LOXL3 Protein Expression Analyses and Gene Expression Impact on Prognosis

Protein expressions of LOX, LOXL1, and LOXL3 were investigated by immunohistochemistry in LGG-IDH^{mut}, LGG-IDH^{wt}, GBM-IDH^{mut}, and GBM-IDH^{wt}. A progressive increase in expression of these proteins was observed from LGG-IDH^{mut}, LGG-IDH^{wt}, and through to GBM, proving highest in GBM and confirming the results of the gene expression analyses (Figure 2).

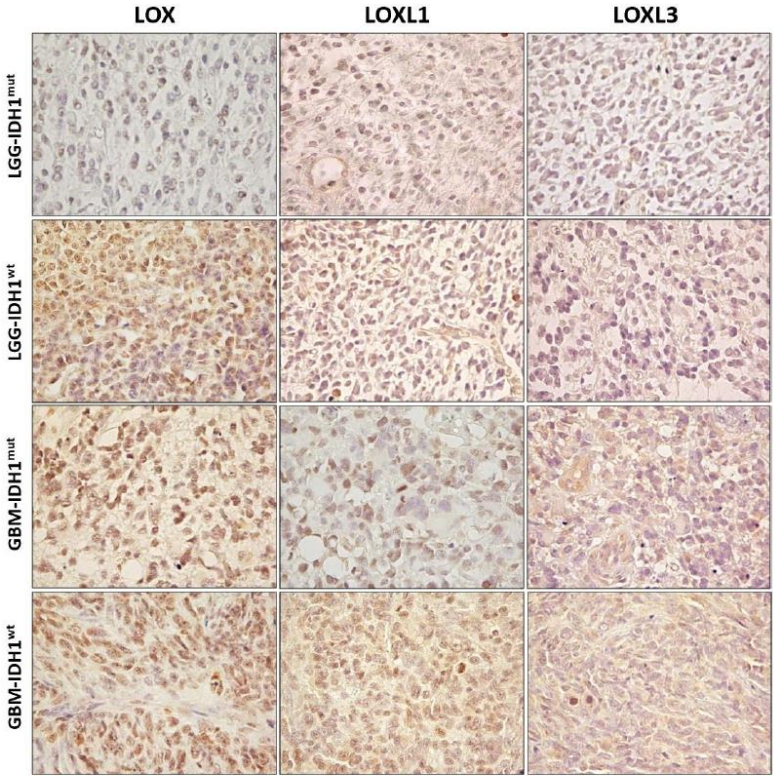

Figure 2. Protein expression levels of LOX, LOXL1, and LOXL3 in astrocytomas. Representative immunohistochemistry slides of lower-grade astrocytic glioma (LGG) and glioblastoma (GBM) with IDH1 mutated (IDH^{mut}) and wild type (IDH^{wt}). Magnification of 400×.

The impacts of *LOX*, *LOXL1*, and *LOXL3* expression levels were analyzed for OS in LGG and GBM, based on the TCGA database. In LGG, patients with higher levels of LOX (p = 0.033) and *LOXL1* (p = 0.002) expression had shorter OS than patients with lower expression (Figure 3A). LGG with highest and lowest levels of *LOX* expression had OS of 49.91 ± 7.38 months and 57.89 ± 10.59 months (p = 0.033), respectively. LGG with the highest and lowest levels of *LOXL1* expression had OS of 19.87 ± 5.25 months and 57.89 ± 8.06 months (p = 0.0034), respectively. Similarly, OS of GBM patients was analyzed using Kaplan–Meier curves. Only *LOXL1* expression levels impacted the prognosis of GBM, where patients with high expression had shorter OS (Figure 3B). GBM patients with *LOXL1* overexpression had mean survival of 10.28 ± 1.11 months, while those with lower expression had mean survival of 13.76 ± 1.09 months (p = 0.0034). Multivariate Cox regression analysis with age at diagnosis identified only *LOXL1* expression as an

independent variable for predicting prognosis in LGG (p = 0.027) (Figure 3C) and GBM patients (p = 0.032) (Figure 3D). In addition, radiotherapy was indicated to 45 (31.5%) out of 143 LGG patients presenting low *LOXL1* expression, in contrast to 55 (49.5%) indications among 111 LGG patients with high *LOXL1* expression. Nevertheless, the survival time was shorter for those with high *LOXL1* expression (Figures 3E and S1).

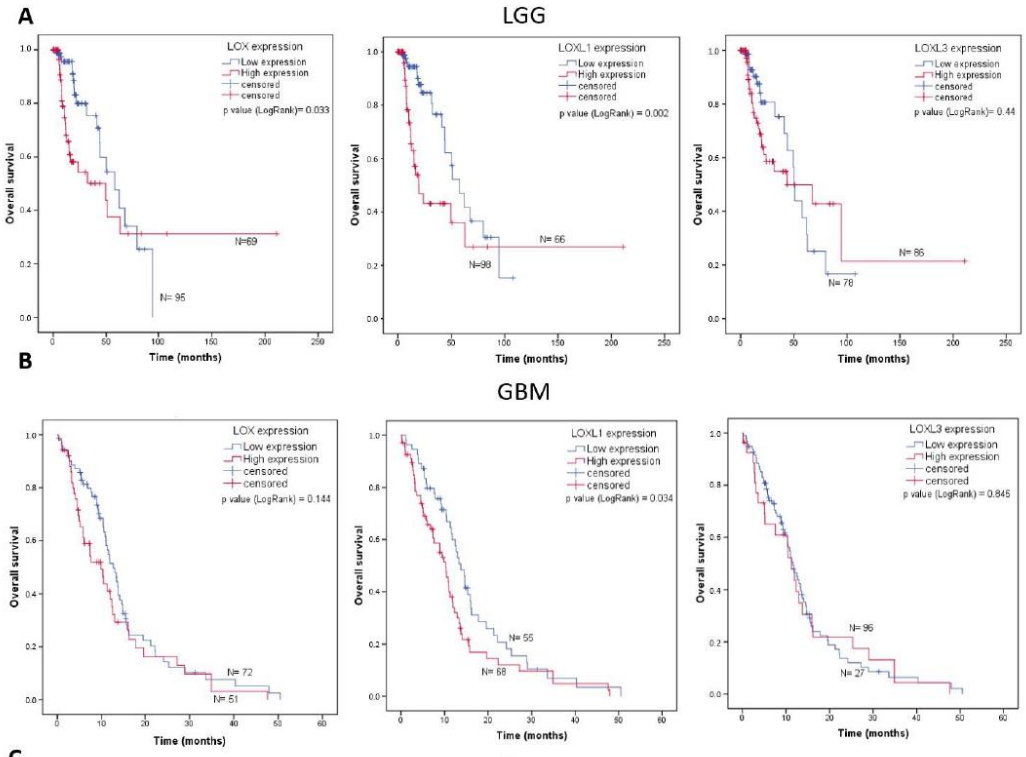

	HR (95% CI)	Sig.
Age |39| Years	3.717 (1.840 – 7.510)	0.000
LOX	1.264 (0.648-2.266)	0.492
LOXL1	2.121 (1.088 – 4.134)	0.027

	HR (95% CI)	Sig.
Age |60| Years	1.379 (0.919 – 2.069)	0.121
LOXL1	1.560 (1.038 – 2.346)	0.032

Figure 3. Overall survival curves of LOX family in LGG and GBM cohort in TCGA database. (**A**) Kaplan–Meier curves for overall survival of LGG patients. High- and low-expression groups were determined according to LGG cases with IDH mutation and IDH wild type by ROC curve. (**B**) Kaplan–Meier curve for overall survival of GBM patients. High- and low-expression groups were determined according to GBM cases with proneural and mesenchymal molecular subtypes by ROC curve. (**C**) Multivariate Cox regression of *LOX*, *LOXL1* and age in LGG cases with HR, 95% CI and

p-values. (**D**) Multivariate Cox regression of *LOXL1* and age in GBM cases with hazard ratios, 95% confidence intervals and *p*-values. (**E**) Overall survival and number of patients submitted or not to radiotherapy with high and low expression of *LOXL1* of LGG cases. Abbreviations: CI, confidence interval; GBM, glioblastoma; HR, hazard ratio; LGG, lower-grade astrocytic gliomas.

2.3. Matrisome Analysis

An in silico analysis of LOX family genes and of genes coding for matrisome proteins was performed to evaluate correlations among the expression profiles using the TCGA and GTEx databases, stratifying cases into LGG and GBM, according to IDH mutation status. Initially, the expression levels of the genes coding for the 1027 matrisome proteins and the of LOX family genes in LGG and GBM compared to NN and LGG compared to GBM, were compared using Limma-voom, as per the workflow depicted in Figure 4. Genes with a log fold change (FC) > |1| and an adjusted $p \leq 0.05$ in any of the comparisons were selected, resulting in 439 upregulated genes and 233 downregulated genes, including *LOX*, *LOXL1*, and *LOXL3*. Expression of *LOXL2* and *LOXL4* did no differ significantly on any of the comparisons. Subsequently, a total of 672 up and downregulated genes in LGG-IDH^{mut}, LGG-IDH^{wt}, and GBM groups were analyzed using Kruskal–Wallis and Dunn's post hoc tests (LGG-IDH^{wt} vs. LGG-IDH^{mut} and LGG-IDH^{wt} vs. GBM). This analysis led to the identification of 70 differentially expressed genes, comprising 9 genes coding for collagens, 17 for ECM glycoproteins, 23 for ECM regulators, 5 for ECM-affiliated proteins, 3 for proteoglycans, 10 for secreted factors, and 3 LOX genes (LOX, LOXL1, and LOXL3) (Supplementary Table S1). The workflow of the selection is presented in Figure 4. The heat map of these 70 genes is presented in Figure 5A. Higher gene expression levels were observed in LGG-IDH^{wt} than in LGG-IDH^{mut}, whereas the highest expression levels were detected in GBM cases, particularly in the mesenchymal molecular subtype.

The strength of the correlations of each of the three LOX genes with the 67 matrisome-related genes was then determined by Pearson's correlation test (Supplementary Table S2). In LGG-IDH^{mut}, 22 genes exhibited a moderate correlation ($0.7 < R < 0.4$, $p < 0.05$), 1 gene, *CTHRC1*, had strong correlation ($R = 0.7$, $p < 0.0001$) with *LOXL1*, and only 2 genes were moderately correlated with *LOXL3*. None of the genes showed a significant correlation with *LOX*. In LGG-IDH^{wt}, 15, 21, and 2 genes had moderate correlations with *LOXL1*, *LOXL3*, and *LOX*, respectively, while *S100A11* and *CTSB* showed strong correlations with *LOXL3* ($R = 0.751$, $p < 0.001$ and $R = 0.740$, $p < 0.001$, respectively). In GBM, 28, 28, and 43 genes showed moderate correlations with LOXL1, *LOXL3*, and *LOX*, respectively, while *SERPINE1* and *PLOD2* displayed strong correlations with *LOX* ($R = 0.707$, $p < 0.001$ and $R = 0.702$, $p < 0.001$, respectively). The levels of expression of the matrisome-associated genes correlated (in increasing complexity) with *LOXL1* in LGG-IDH^{mut}, *LOXL3* in LGG-IDH^{wt} and with the three LOXs, but most strongly with *LOX* in GBM (Figure 5B).

Potential involvement of mechanosensitive transcription factors (TFs) (*CTNNB1*, *HIF1A*, *JUN*, *JUNB*, *LEF1*, *NFKB1*, *SMAD2*, *SMAD3*, *SNAI1*, *SOX2*, *STAT3*, *TWIST1*, *YAP1*) in the observed expression profiles was investigated by analyzing the correlation of these TFs with *LOXL1*, *LOXL3*, and *LOX* expressions. *NFKB1* and *SOX2* were differentially expressed across the groups analyzed (LGG-IDH^{mut}, LGG-IDH^{wt}, and GBM) but correlated only with *LOXL3* and *LOX* expression levels in LGG-IDH^{wt} and GBM, respectively (data not shown). Interestingly, the level of *CTNNB1* expression was significantly higher in LGG-IDH^{wt} than in LGG-IDH^{mut} ($p < 0.0001$), and also higher in GBM related to LGG-IDH^{wt} ($p = 0.0081$) (Figure 6A), correlating with *LOXL1* and *LOXL3* expression both in LGG-IDH^{mut} and LGG-IDH^{wt} (Figure 6B).

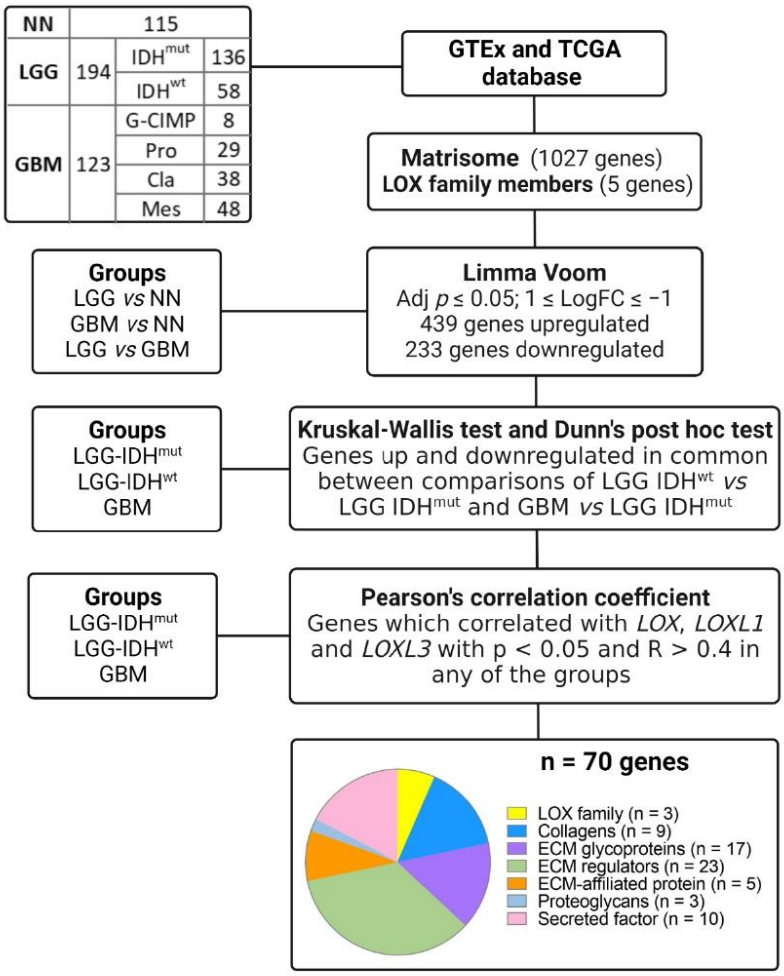

Figure 4. Workflow of in silico analysis of genes coding for matrisome and LOX family in LGG and GBM cohort on TCGA database. Abbreviations: ECM, extracellular matrix; FC, fold change; GBM, glioblastoma; GTEx, Genotype-Tissue Expression; IDH^{mut}, isocitrate dehydrogenase gene with mutation; IDH^{wt}, isocitrate dehydrogenase gene wild type; LGG, lower-grade astrocytic glioma; NN, non-neoplastic; TCGA, The Cancer Genome Atlas. Created with BioRender.com.

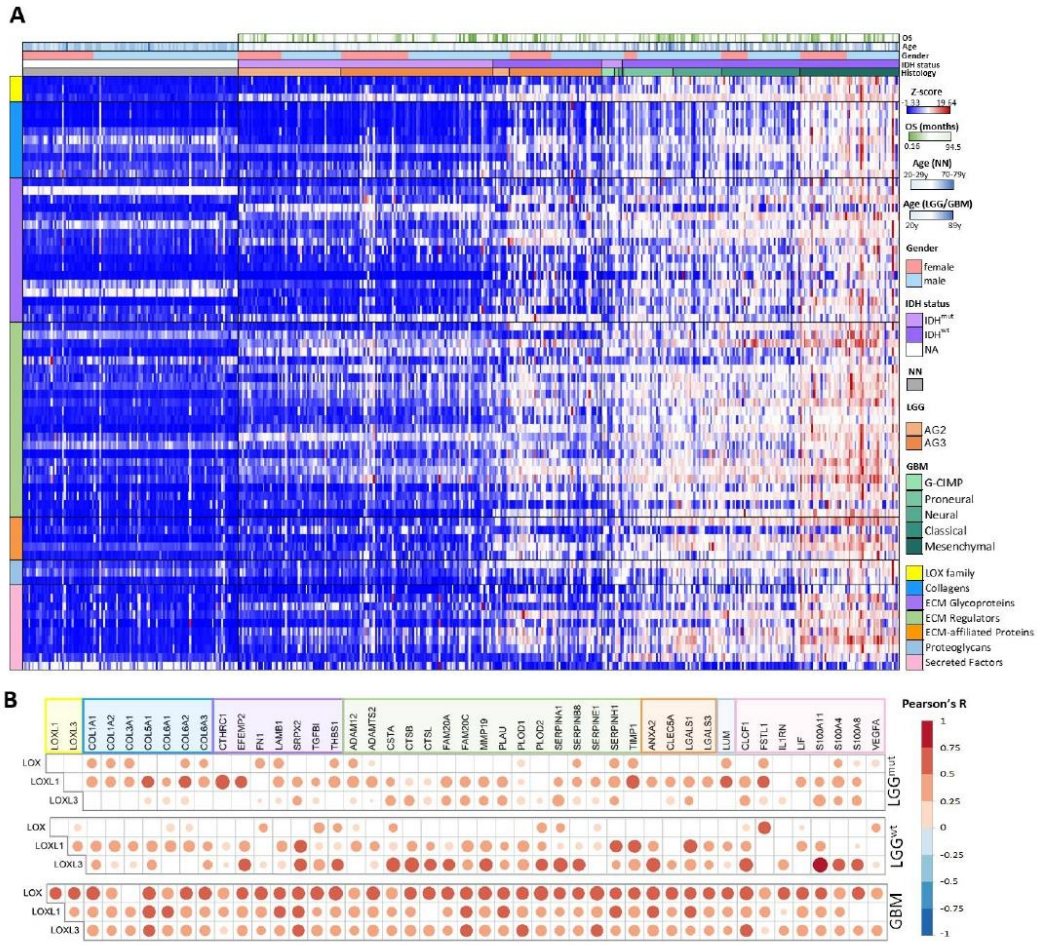

Figure 5. Lysyl oxidase family and matrisome gene expression analyses. (**A**) Heatmap of lysyl oxidase family and matrisome genes in non-neoplastic brain samples and diffuse astrocytomas with IDH mutation status and different subtypes of glioblastoma. The 70 genes selected using the workflow presented in Figure 4 are depicted in the heatmap of z-score of normalized read counts. (**B**) Pearson's correlation coefficient test of *LOX*, *LOXL1*, and *LOXL3* and matrisome genes in LGG IDH^{mut}, LGG IDH^{wt}, GBM groups. Abbreviations: AG2, low-grade astrocytoma; AG3, anaplastic astrocytoma; ECM, extracellular matrix; GBM, glioblastoma; IDH^{mut}, isocitrate dehydrogenase gene with mutation; IDH^{wt}, isocitrate dehydrogenase gene wild type; LGG, lower-grade astrocytic glioma; NA, not analyzed.

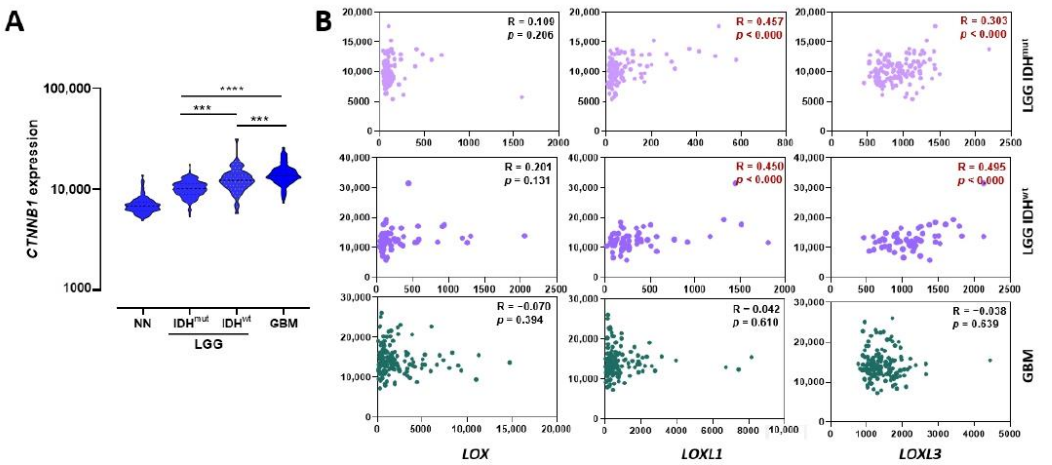

Figure 6. β-catenin gene expression in astrocytoma and relationship with LOX members. (**A**) Expression levels of *CTNNB1* in non-neoplastic tissues, LGG (AG2 and AG3) with (IDH^{mut}) and without (IDH^{wt}) IDH mutation, and GBM cases. Differences were statistically significant ($p < 0.0001$) as determined by Kruskal–Wallis test. Middle lines represent median of groups. Top and bottom lines represent first and third quartiles, respectively. The post-hoc Dunn's multiple comparison test was used to calculate differences in expression between two groups (*** $p < 0.001$; **** $p < 0.0001$). (**B**) Pearson's correlation coefficient test of *CTNNB1* expression levels and *LOX*, *LOXL1*, and *LOXL3* in groups of LGG-IDH^{mut}, LGG-IDH^{wt}, and GBM. Significative correlations (in red) between *LOXL1* and *LOXL3* with *CTNNB1* were observed in LGG-IDH^{mut} and LGG-IDH^{wt}. Abbreviations: GBM, glioblastoma; IDH^{mut}, isocitrate dehydrogenase gene with mutation; IDH^{wt}, isocitrate dehydrogenase gene wild type; LGG, lower-grade astrocytic glioma; NN, non-neoplastic.

3. Discussion

ECM stiffness contributes significantly to cancer progression by promoting tumor cell proliferation, invasion, and drug resistance. In fact, the matrix stiffness of glioma is higher than that of normal brain tissue and increases with malignancy [28,29]. The LOX family is widely known as amine oxidase enzymes responsible for crosslinking of ECM collagens and/or elastin that determines ECM tensile strength, remodeling, and integrity [6,7,18,30–33]. LOX is the most extensively studied member of this family and, in a previous study by our group, a progressive increase in LOX expression according to malignancy was observed in human astrocytomas [34]. In the present study, the role of the other LOX family members in the progression of astrocytomas was confirmed. *LOXL1*, *LOXL2*, *LOXL3*, and *LOXL4* expression levels were also found to increase progressively in astrocytomas from grades 2 to 4, proving highest in GBM, and significantly higher relative to non-neoplastic brain tissue. These results were subsequently confirmed in silico for the TCGA glioma RNAseq dataset. Similar results have been observed for other tumors, suggesting a key role of the LOX family members in tumor progression [9,18,21,35–40]. In a previous study by our group, a correlation of LOX expression level with IDH1 mutation status was found in diffusely infiltrative astrocytomas (grades 2 to 4) [27]. Similarly, significant differential expression of the other LOX family members according to IDH mutational status was also observed in the present investigation. Oncogenic IDH mutations lead to decreased levels of α-ketoglutarate (α-KG) and accumulation of 2-hydroxyglutarate (2HG) [41], an oncometabolite linked to increased reactive oxygen species (ROS) production [42] and decreased mitochondrial respiration in GBM cells [43]. Moreover, 2HG is a competitive inhibitor of α-KG dependent dioxygenases, including histone demethylases and the ten

eleven translocation (TET) family of 5-methylcytosine (5mC) hydroxylases, which promote marked epigenetic alterations [44]. Given α-KG is also required by prolyl hydroxylases to promote the degradation of hypoxia-inducible factor 1 alpha (HIF-1α), the IDH mutation with decreased α-KG level leads to HIF-1α stability [45]. Thus, increased HIF-1α promotes ECM remodeling through regulation of collagen deposition by tumor cells [46] and up-regulation of metalloproteinases and collagen-modifying enzymes in stromal cells [47]. Glioma aggressiveness and patient outcomes have also been found to correlate with HIF-1α levels and tenascin C-enriched ECM stiffness. IDH^{mut} has been shown to restrict tumor aggression by decreasing HIF1α-dependent tenascin C expression, thereby decreasing ECM stiffness and mechanosignaling [28]. In fact, ECM stiffness has been described as significantly lower in IDH^{mut} than in IDH^{wt} tumors [28] and, clinically, LGG-IDH^{wt} has a poorer prognosis than LGG-IDHmut [48]. Moreover, reports show *LOX* [49], *LOXL1*, and *LOXL3* [50] expression levels are modulated by HIF-1α. Regulation of ECM stiffness and glioma cell migration by LOX expression have been shown in drosophila and mouse models [51], and LOX activity was reduced by HIF-1α knockdown [50]. Correlations of *LOX* expression with epithelial mesenchymal transition (EMT) and IDH1 mutation status have also been described [52]. Similarly, *LOXL1* has been associated with tumor invasion, metastasis, and extracellular accumulation of lactate [53], linked to integrin α11, a stromal collagen receptor [54]. Associations of *LOXL3* expression with EMT (through E-cadherin transcription repression by SNAIL) [55,56], cell invasion in breast cancer [57], and with GBM cell adhesion and invasion [10] have been described. Interestingly, genes related to EMT were overexpressed in IDH^{wt} [58].

In the present study, a progressive increase in levels of *LOX*, *LOXL1*, and *LOXL3* expression was observed for LGG-IDH^{mut}, LGG-IDH^{wt}, and GBM in the TCGA glioma RNAseq dataset, suggesting their role in determining ECM composition and stiffness enhancement in these phenotypes.

ECM stiffness is related to matrix composition, matrix contraction, and matrix crosslinking, where LOX family members play a major role [59]. Concerning matrix composition, collagen is an ECM scaffolding protein that contributes significantly to the tensile strength of tissue, binding cells by forming specialized extracellular networks [60]. Fibrillar collagen types I-III, V, and XI are the most common [61], and LOX, LOXL1, and LOXL3 are preferentially associated with fibrillar collagen types I and III [6]. In this study, *COL1A1*, *COL1A2*, *COL3A1*, and *COL5A1* expression levels were correlated with all three LOXs in GBM, whereas *COL6A1-3* expression levels correlated with *LOXL1* and *LOXL3* in LGG, and with all three LOXs in GBM. Fibrillar collagen deposition was described in the adventitia of remodeled large vessels and glomeruloid vascular structures of GBM [62]. High *COL6A1* expression levels were observed in astrocytoma of different malignancy grades, especially in higher grade tumors associated with poor prognosis [63]. COL6A1 was detected in perivascular regions and pseudopalisading cells, while COL6A1 expression was associated with hypoxia [64] and VEGF expression [65].

Results showed overexpression of two genes coding for lysyl hydroxylases, procollagen-lysine, and 2-oxoglutarate 5-dioxygenase (PLOD) [66], *PLOD1*, and *PLOD2*, involved in collagen biosynthesis and crosslinking [66,67] in LGG-$IDH1^{wt}$ and GBM. Similar results were recently reported by other authors [68,69] and in other cancer types with aggressive phenotype [70]. We also found upregulation of another gene related to collagen biosynthesis, the serpin family H member 1 (*SERPINH1*), which was significantly correlated with LOXL1 in LGG-IDH^{wt} and GBM, and with LOX in GBM. *SERPINH1* encodes a heat shock protein (HSP47) localized in the endoplasmic reticulum, participates in the correct folding of collagen [71], and facilitates its secretion and deposition [72]. Increased expression of HSP47 has been associated with high malignancy grade of glioma [73]. Transforming growth factor β1 (TGF-β1) is also an inducer of collagen biosynthesis [74], and the gene coding for the transforming growth factor beta induced (TGFBI) was overexpressed and correlated significantly with LOX expression in GBM. TGFBI binds to collagens I, II, and IV and, therefore, mediates cell–collagen interaction. TGFBI also inhibits cell adhesion, promotes cell migration in glioma

cells [75] and has been associated with the expression signature of mesenchymal GBM [76], the molecular subtype with the poorest prognosis.

The organization of collagen fibrils, including modulation of their diameters and interfibrillar spacing [77], is performed by lumican (coded by *LUM*), a class II leucine rich proteoglycan. The ECM organization process assembles adhesion plaque complexes and allows integrins to transduce cues from the ECM by activating a signaling cascade that induces cytoskeletal remodeling and regulates cell behavior [78]. Thus, LUM may enhance cancer growth through integrin β1 activating the β-catenin/focal adhesion kinase (FAK) [79]. Fibronectin [80] also induces α5β1 signaling and rapidly activates the downstream cascade through FAK, providing tensile support for motility of cancer cells in the invasion process [81]. In addition, β1 integrins and tumor adhesion to FN1 mediate resistance to radiotherapy [82]. Previous studies have reported that radiotherapy increases LOX secretion [83]. In the current analysis, both *LUM* and *FN1* were upregulated and showed significant correlation with *LOX* in GBM. A high abundance of FN1 protein in the ECM of GBM was previously demonstrated by our group [84].

Metabolically, IDH^{wt} possesses a cytosolic substrate composition that is better suited for collagen biosynthesis. Proline (Pro) constitutes about 10% of total amino acids in collagen [85], and can be synthesized from arginine, glutamine (Gln), and glutamate (Glu) [86]. The presence of IDH^{mut} in glioma leads to a significant reduction in Gln and Glu levels, whereas IDH^{wt} gliomas contain high levels of intracellular Glu [87,88], providing Pro for collagen biosynthesis through the activity of two enzymes: aldehyde dehydrogenase 18 family member A1, coded by *ALDH18A1*, and pyrroline-5-carbohydrate reductase 1, coded by *PYCR1*. These two enzymes synthesize Glu to glutamate ϒ-semialdehyde and then to Pro, respectively. Interestingly, both these genes were upregulated in both LGG and GBM (data not shown).

In addition to Glu accumulation, an increase in lactate level can be observed in IDH^{wt} due to the Warburg effect, with a shift of the oxidative tricarboxylic acid cycle towards glycolysis [89]. Glycolytically derived acids are transported to the extracellular microenvironment by membrane ion pumps and transporters, substantially lowering extracellular pH [90]. The acidification of tumoral environments produces favorable conditions for tumor cell invasion, as it induces the formation and maturation of invadopodia and activates proteases to focally degrade the ECM [91], through metalloproteinase 3 activity [92] and MMP9 secretion [93]. Moreover, acid-activated protease, such as cathepsin B (CTSB) [94], is secreted into the ECM at low pH. CTSB is located predominantly in secretory vesicles [95] and participates in ECM remodeling by degrading ECM components such as collagen, laminin, fibrin, elastin and TNC [96–98]. In gliomas, CTSB can bind to ANXA2 and induce the expression of vascular endothelial growth factor C, TGF-β, and MMP9 to promote angiogenesis [99,100]. *CSTB* upregulation has been described in GBM [101] and GBM stem cells [102], particularly in IDH^{wt}, and has been strongly associated with the mesenchymal subtype and immunosuppressive conditions in gliomas [94]. Interestingly, *CTSB* was highly correlated with *LOXL3* in LGG-IDH^{wt} and with LOX in GBM. The 2-HG generated in IDH^{mut} enhances angiogenesis through HIF1α stabilization, partially by decreasing levels of endostatin, an HIF1α antagonist, which in turn increases vascular VEGF signaling [103]. VEGFA was upregulated and significantly correlated with *LOX* in GBM. Additionally, the expression level of the collagen triple helix repeat containing-1 gene (*CTHRC1*), an ECM glycoprotein inducer of angiogenesis, migration, and cell invasion, showed the highest correlation with LOXL1 in LGG-IDH^{mut}. FN1, significantly correlated with LOX expression in GBM in the present analysis, may also promote angiogenesis in cancer by providing a ridged structure for vessel development and signaling for endothelial cell migration [104].

Lastly, the ways in which ECM stiffness can trigger mechanotransduction were analyzed by searching for correlations between the differentially expressed genes and mechanosensitive transcription factors. Interestingly, there was a progressive increase in *CTNNB1*, which codes for β-catenin, according to astrocytoma malignancy grade, and its expression correlated significantly with *LOXL1* and *LOXL3* expression in both LGG-

IDH^{mut} and LGG-IDH^{wt}. Collagen deposition and crosslinking promote ECM stiffness and clustering of integrins, leading to FAK activation with subsequent PI3K/AKT activation, inhibition of GSK-3β, and stabilization of β-catenin [105]. Nuclear accumulation of β-catenin and induction of stemness by matrix stiffness was observed in glioma cells [29]. LOXL1 has previously been shown to regulate cell migration and apoptosis via Wnt/β-catenin signaling [106]. However, this is the first report of correlation of *LOXL3* with β-catenin expression level in cancer. Recently, our group identified upregulation of LOXL1 and involvement of Wnt/β-catenin signaling in the malignant transformation of normal astrocytes by anoikis [107]. We speculate that *LOXL1*, and its interactions with the matrisome-related genes, may be involved in this first step of transformation towards an astrocytic tumor. Additionally, elements of TCF/LEF transcription factors were identified in the promoter region of LOXL1, suggesting that the β-catenin signaling pathway may regulate positively LOXL1 expression [108].

Overall, the results showed a significant correlation of increased gene expression of *LOXL1*, *LOXL3* and *LOX* with matrisome-related gene expression, possibly explaining the progressive increase in ECM stiffness from LGG-IDH^{wt}, LGG-IDH^{wt}, and through to GBM. Figure 7 summarizes our findings. More specifically, the *LOXL1* correlation net was detected in less malignant astrocytomas. Connectivity with *LOXL3* was prominent among more aggressive LGG-IDH^{wt}, and strong connectivity with *LOX* was detected in GBM, demonstrating the complexity of ECM components involved in astrocytoma progression. More specifically, level of LOXL1 expression impacted the outcome of LGG and GBM patients, with shorter OS in individuals exhibiting higher expression. In addition, radiotherapy was indicated more frequently in LGG patients with high LOXL1 expression, yet this group had shorter survival than LGG patients with low LOXL1 expression.

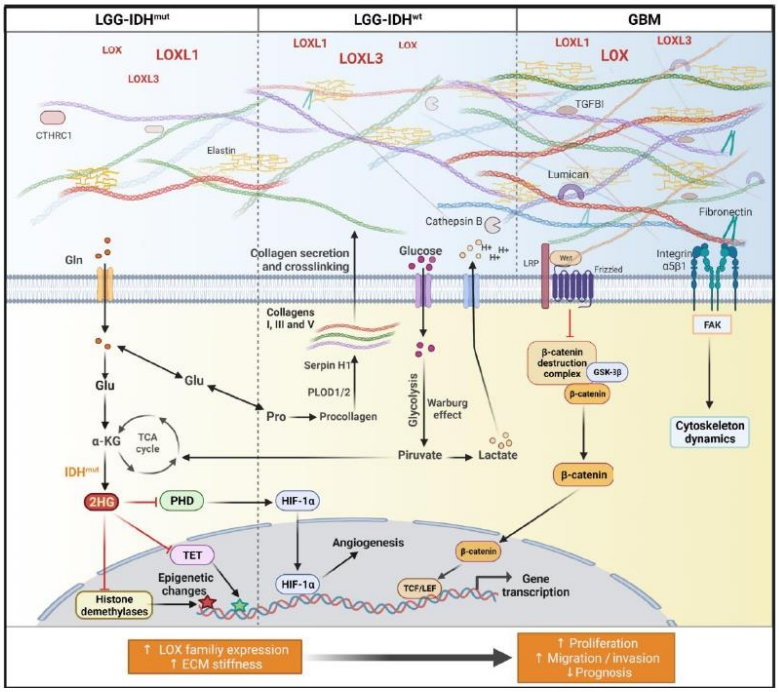

Figure 7. Schematic diagram representing LOX family influence in extracellular matrix composition of astrocytomas. Malignancy and aggressiveness increase from LGG-IDH^{mut}, LGG-IDH^{wt}, and through

to GBM, and have been attributed to the IDH mutation status and ECM stiffness. ECM composition in turn was directly related to differential expression levels of *LOX*, *LOXL1*, and *LOXL3*, and their correlations with matrisome-associated genes, especially fibrillar collagens type I, III, and V. *LOXL1* expression level correlated significantly with expression of *CTHRC1* in LGG-IDH^{mut}. In LGG-IDH^{wt}, strong correlations were observed between *LOXL3* and cathepsin B expression levels. *LOX* expression correlated significantly with *PLOD1* and *PLOD2* (related to collagen biosynthesis) and with serpin H1 (involved in collagen folding). In IDH^{wt}, Glu is accumulated and converted to Pro favoring collagen biosynthesis. The Warburg effect, with increased glucose uptake and glycolysis, leads to lactate production with lowering of extracellular pH, which promotes cathepsin B secretion and contributes to ECM degradation and remodeling. In GBM, *LOX* expression correlated with genes coding for lumican, TGFI, and fibronectin expression levels. ECM stiffness triggers mechanotransduction through α5β1 integrins and Wnt/β-catenin signaling with translocation of β-catenin to nucleus and transcription genes related to tumor malignant progression. Abbreviations: 2HG, 2-hydroxyglutarate; α-KG, α-ketoglutarate; CTHRC1, collagen triple helix repeat containing-1; ECM, extracellular matrix; FAK, focal adhesion kinase; GBM, glioblastoma; Gln, glycine; Glu, glutamine; GSK-3β, glycogen synthase kinase 3 beta; HIF-1α, hypoxia-inducible factor 1 alpha; IDH^{mut}, isocitrate dehydrogenase gene with mutation; IDH^{wt}, isocitrate dehydrogenase gene wild type; LEF, lymphoid enhancer factor; LGG, lower-grade astrocytic gliomas; PHD, prolyl hydroxylase; Pro, proline; TCA, tricarboxylic acid; TCF, T cell factor; TET, ten eleven translocation; Wnt, wingless and Int-1. Created with BioRender.com.

4. Materials and Methods

4.1. Tissue Samples

The casuistic samples consisted of 130 diffusely infiltrative astrocytomas (grades II to IV). Tumors were graded according to the WHO classification AG2 (n = 26, mean age at diagnosis 34.0 ± 8.1 years, 15 males and 11 females), AG3 (n = 18, mean age at diagnosis 35.0 ± 12.3 years, 11 males and 7 females), and GBM (n = 86 mean age at diagnosis 54.0 ± 13.9 years, 58 males and 28 females). The non-neoplastic control group consisted of samples from individuals undergoing temporal lobe resection during epilepsy surgery (n = 22, mean age at diagnosis 38.0 ± 7.6 years, 10 males and 12 females). All samples were collected during surgical procedures by the Neurosurgery Group of the Department of Neurology at the Hospital das Clinicas of the School of Medicine of University of Sao Paulo. Fresh surgical samples were immediately snap-frozen in liquid nitrogen upon surgical removal. Before RNA extraction, a 4-µm-thick section of each sample was obtained for histological assessment using a cryostat at −25 °C. Sections were stained with hematoxylin and eosin and examined under light microscope. Necrotic and non-neoplastic areas were removed from the frozen block of tumoral tissue by microdissection prior to RNA extraction. Grey matter was avoided in the control samples. Written informed consent was obtained from all patients according to the ethical guidelines approved by the Ethical Committee of the School of Medicine, University of São Paulo (0599/10).

4.2. Total RNA Extraction and cDNA Synthesis

Total RNA was extracted from frozen tissues using the RNeasy Mini kit (Qiagen, Hilden, Germany). RNA concentration and purity were determined by measuring absorbance at 260 and 280 nm. Ratios of 260/280 measures ranging from 1.8 to 2.0 were considered acceptable for purity standards. Denaturing agarose gel electrophoresis was used to evaluate the integrity of samples. A conventional reverse transcription reaction was performed to yield single-stranded cDNA. The first strand of cDNA was synthesized from 1000 ng of total RNA previously treated with one unit of DNase I (FPLC-pure, GE Healthcare, Uppsala, Sweden) using random and oligo (dT) primers, RNase inhibitor, and SuperScript III reverse transcriptase according to the recommendations of the manufacturer (Thermo Fisher Scientific, Carlsbad, CA, USA). The resulting cDNA was subsequently treated with one unit of RNase H (GE Healthcare), diluted with TE buffer, and stored at −20 °C until later use.

4.3. Reverse Transcription Quantitative Real Time PCR

Analysis of relative expression levels of LOXL1, LOXL2, LOXL3, and LOXL4 were performed by RT-qPCR using the Sybr Green I approach. Quantitative data were normalized in relation to the geometric mean of three reference genes: glucuronidase beta (GUSB), hypoxanthine phosphoribosyltransferase (HPRT), and TATA box binding protein (TBP). Table 1 shows the specific primer sequences and concentrations used for RT-qPCR. The minimum primer concentrations necessary were determined to give the lowest quantification cycle (Cq) and maximum amplification efficiency, while minimizing non-specific amplification. Primer concentrations used were 200 nM for all primers, except for GUSB which was 400 nM. Standard curves were established to ensure amplification efficiency, and analysis of melting curves demonstrated a single peak for all PCR products. Additionally, agarose gel electrophoresis was employed to check the size of the PCR products amplified. Sybr Green I amplification mixtures (12 µL) contained 3 µL of cDNA, 6 µL of Power Sybr Green I Master Mix (Thermo Fisher Scientific), and forward and reverse primers. PCR reactions were run on an ABI Prism 7500 sequence detector (Thermo Fisher Scientific) as follows: 2 min at 50 °C, 10 min at 95 °C, and 40 cycles of 15 s at 95 °C, and 1 min at 60 °C. The equation 2-µCt was applied to calculate the expression in all samples, where ΔCt = [Ct of gene − geometric mean Cq of reference genes]. The RT-qPCR reactions for each sample were performed in duplicates and repeated when the Cq values were not similar. The results are presented on a log10 scale for better visualization. The gene expression levels were scored according to the median relative expression values of each astrocytoma grade. For statistical analysis, scores equal or higher than the median values were defined as overexpression.

Table 1. Oligonucleotides for RT-qPCR reactions.

Gene	PCR Product (bp)	Orientation	Primer Sequences (5′-3′)
LOX	117	Sense Antisense	CCTACTACATCCAGGCGTCCA CATAATCTCTGACATCTGCCCTGT
LOXL1	162	Sense Antisense	GCTATGACACCTACAATGCGGA GACCTGTGTAGTGAATGTTGCATCT
LOXL2	112	Sense Antisense	ACCCACCCACTATGACCTGCT CTCGTAATTCTTCTGGATGTCTCCT
LOXL3	115	Sense Antisense	CTGGAACAGGCCGCATCT CCCCAGCATCCTCATCGT
LOXL4	115	Sense Antisense	GGCAGAGTCAGATTTCTCCAACA GAGTTCTGCATTGGCTGGGTAT
GUSB	101	Sense Antisense	GAAAATACGTGGTTGGAGAGCTCATT CCGAGTGAAGATCCCCTTTTTA
HPRT	118	Sense Antisense	TGAGGATTTGGAAAGGGTGT GAGCACACAGAGGGCTACAA
TBP	98	Sense Antisene	AGGATAAGAGAGCCACGAACCA CTTGCTGCCAGTCTGGACTG

4.4. Immunohistochemistry

The immunohistochemical procedures for LOX, LOXL1, and LOXL3 expression analyses were performed on 4-µm slices of paraffin-embedded tissues of 6 cases each of AG2, AG3, and GBM. Tissue sections were first subjected to antigen retrieval in 10 mM citrate buffer, pH 6.0, and incubated at 122 °C for 3 min using an electric Pascal (BioCare Medical, Walnut Creek, CA, USA). Specimens were then blocked and further incubated with primary antibodies against human LOX (ab31238, Abcam, Cambridge, UK), LOXL1 (HPA 042111, Sigma-Aldrich, St Louis, MO, USA), and LOXL3 (ARP60280, Aviva, San Diego, CA, USA) at 16–20 °C for 16 h. Slices were then incubated for endogenous peroxidase

blocking (Novolink Polymer Detection System, Novocastra, Newcastle upon Tyne, UK) at 16–20 °C for 16 h. Antibodies localization was visualized using diaminobenzidine and Harris hematoxylin. Table 2 show the positive controls were used for all reactions, as well as the dilutions for each antibody.

Table 2. Primary antibodies used for immunohistochemistry.

Antibodies	Specificity	Company	Positive Control	Dilution
LOX	rabbit polyclonal	Abcam	Placenta	1:400
LOXL1	rabbit polyclonal	Sigma-Aldrich	Esophagus	1:100
LOXL3	rabbit polyclonal	Aviva	Placenta	1:50

4.5. TCGA

In silico analysis of gene expression was performed in TCGA database (http://www.cbioportal.org, accessed on 1 May 2022) [109,110]. Gene expression dataset from non-tumoral brain samples was obtained from GTEx project (https://gtexportal.org/, accessed on 1 May 2022) [111]. Data was downloaded and read counts were normalized by DeSeq [112]. Data consisted in 115 of non-neoplastic samples, 194 LGG (136 IDH^{mut}, 58 IDH^{wt}), and 160 samples of GBM (8 G-CIMP, 29 proneural, 38 classical, and 48 mesenchymal subtype). Matrisome gene lists were based on the Matrisome Project (http://matrisome.org/, accessed on 1 May 2022) [113]. Normalized read counts were converted to a z-score for heat map visualization.

4.6. Statistical Analysis

The distribution of gene expression data was analyzed by the normality test of Kolmogorov–Smirnov and Shapiro–Wilk test. For gene expression, non-parametric Kruskal–Wallis test was used to compare multiple groups, followed by Dunn's post-hoc test. Kaplan–Meier survival curves were analyzed using the log-rank test. Multivariate Cox proportional regression analysis was performed using age as a covariate with gene expression level. Receiver Operating Characteristic curves were used to determine the high and low expression groups to Kaplan–Meier analysis for OS of LGG and GBM cases. The cut off of the expression values for ROC analysis was determined for the LGG cases were divided into IDH^{mut} and IDH^{wt}, and for GBM samples, the cases were divided into proneural and mesenchymal subtype. Limma package with voom method in R package was used for differentially expressed gene analysis. Correlation analyses between gene expression values were assessed by the non-parametric Pearson's correlation test. Correlation coefficient R value used was $R > 0.5$. Statistical significances were considered when $p \leq 0.05$. All analyses were performed using SPSS version 20.0 (IBM Corporation, Armonk, NY, USA), R software, and plots were made using the program GraphPad Prism version 8.0 (GraphPad Software, San Diego, CA, USA).

5. Conclusions

The LOX family was increasingly expressed according to malignancy of astrocytoma, exhibiting the highest expression in GBM. The progressive gene expression connectivity among LOX, LOXL1, and LOXL3 and matrisome-related genes from LGG-IDH^{mut}, LGG-IDH^{wt}, and through to GBM, reinforce the impact of ECM components contributing for matrix stiffness on the malignant progression and prognosis of astrocytoma.

Supplementary Materials: The following are available online at https://www.mdpi.com/article/10.3390/ijms23179507/s1.

Author Contributions: Conceptualization, T.d.S.L., R.d.S.S., S.K.N.M. and S.M.O.-S.; Data curation, T.d.S.L. and R.d.S.S.; Formal analysis, T.d.S.L., R.d.S.S. and S.K.N.M.; Methodology, T.d.S.L. and R.d.S.S.; Supervision, S.K.N.M. and S.M.O.-S.; Writing—original draft, T.d.S.L. and R.d.S.S.; Writing—

review and editing, S.K.N.M. and S.M.O.-S. All authors have read and agreed to the published version of the manuscript.

Funding: This research was supported by Conselho Nacional de Pesquisa (CNPq), Sao Paulo Research Foundation (FAPESP, grants #2015/03614-5, #2016/05777-1, #2020/02988-9, #2021/01207-4), Coordenação de Aperfeiçoamento de Pessoal de Nível Superior-Brasil (CAPES/PROEX)—Finance Code 23038.018285/2019-21, and Faculdade de Medicina da USP (FMUSP).

Institutional Review Board Statement: Not applicable.

Informed Consent Statement: Not applicable.

Data Availability Statement: Not applicable.

Conflicts of Interest: The authors declare that the research was conducted in the absence of any commercial or financial relationships that could be construed as a potential conflict of interest.

References

1. Kumar, S.; Weaver, V.M. Mechanics, malignancy, and metastasis: The force journey of a tumor cell. *Cancer Metastasis Rev.* **2009**, *28*, 113–127. [CrossRef] [PubMed]
2. Seewaldt, V. ECM stiffness paves the way for tumor cells. *Nat. Med.* **2014**, *20*, 332–333. [CrossRef] [PubMed]
3. Grigorieva, E.V. Radiation Effects on Brain Extracellular Matrix. *Front. Oncol.* **2020**, *10*, 576701. [CrossRef] [PubMed]
4. Levental, K.R.; Yu, H.; Kass, L.; Lakins, J.N.; Egeblad, M.; Erler, J.T.; Fong, S.F.; Csiszar, K.; Giaccia, A.; Weninger, W.; et al. Matrix crosslinking forces tumor progression by enhancing integrin signaling. *Cell* **2009**, *139*, 891–906. [CrossRef] [PubMed]
5. Wullkopf, L.; West, A.V.; Leijnse, N.; Cox, T.R.; Madsen, C.D.; Oddershede, L.B.; Erler, J.T. Cancer cells' ability to mechanically adjust to extracellular matrix stiffness correlates with their invasive potential. *Mol. Biol. Cell* **2018**, *29*, 2378–2385. [CrossRef]
6. Grau-Bové, X.; Ruiz-Trillo, I.; Rodriguez-Pascual, F. Origin and evolution of lysyl oxidases. *Sci. Rep.* **2015**, *5*, 10568. [CrossRef]
7. Csiszar, K. Lysyl oxidases: A novel multifunctional amine oxidase family. *Prog. Nucleic Acid Res. Mol. Biol.* **2001**, *70*, 1–32. [CrossRef]
8. Amendola, P.G.; Reuten, R.; Erler, J.T. Interplay Between LOX Enzymes and Integrins in the Tumor Microenvironment. *Cancers* **2019**, *11*, 729. [CrossRef]
9. Wang, T.-H.; Hsia, S.-M.; Shieh, T.-M. Lysyl Oxidase and the Tumor Microenvironment. *Int. J. Mol. Sci.* **2017**, *18*, 62. [CrossRef]
10. Laurentino, T.d.S.; Soares, R.d.S.; Lerario, A.M.; Marie, S.K.N.; Oba-Shinjo, S.M. LOXL3 Silencing Affected Cell Adhesion and Invasion in U87MG Glioma Cells. *Int. J. Mol. Sci.* **2021**, *22*, 8072. [CrossRef]
11. Xu, X.H.; Jia, Y.; Zhou, X.; Xie, D.; Huang, X.; Jia, L.; Zhou, Q.; Zheng, Q.; Wang, K.; Jin, L.P. Downregulation of lysyl oxidase and lysyl oxidase-like protein 2 suppressed the migration and invasion of trophoblasts by activating the TGF-β/collagen pathway in preeclampsia. *Exp. Mol. Med.* **2019**, *51*, 1–12. [CrossRef] [PubMed]
12. Wei, L.; Song, X.R.; Sun, J.J.; Wang, X.W.; Xie, L.; Lv, L.Y. Lysyl Oxidase May Play a Critical Role in Hypoxia-Induced NSCLC Cells Invasion and Migration. *Cancer Biother. Radiopharm.* **2012**, *27*, 672–677. [CrossRef] [PubMed]
13. Hong, X.; Yu, J.J. Silencing of lysyl oxidase-like 2 inhibits the migration, invasion and epithelial-to-mesenchymal transition of renal cell carcinoma cells through the Src/FAK signaling pathway. *Int. J. Oncol.* **2019**, *54*, 1676–1690. [CrossRef] [PubMed]
14. Shih, Y.H.; Chang, K.W.; Chen, M.Y.; Yu, C.C.; Lin, D.J.; Hsia, S.M.; Huang, H.L.; Shieh, T.M. Lysyl oxidase and enhancement of cell proliferation and angiogenesis in oral squamous cell carcinoma. *Head Neck* **2013**, *35*, 250–256. [CrossRef]
15. Tsai, S.Y.; Chang, Y.L.; Swamy, K.B.S.; Chiang, R.L.; Huang, D.H. GAGA factor, a positive regulator of global gene expression, modulates transcriptional pausing and organization of upstream nucleosomes. *Epigenet. Chromatin* **2016**, *9*, 32. [CrossRef] [PubMed]
16. Gao, Y.; Xiao, Q.; Ma, H.; Li, L.; Liu, J.; Feng, Y.; Fang, Z.; Wu, J.; Han, X.; Zhang, J.; et al. LKB1 inhibits lung cancer progression through lysyl oxidase and extracellular matrix remodeling. *Proc. Natl. Acad. Sci. USA* **2010**, *107*, 18892–18897. [CrossRef]
17. Jeong, Y.J.; Park, S.H.; Mun, S.H.; Kwak, S.G.; Lee, S.J.; Oh, H.K. Association between lysyl oxidase and fibrotic focus in relation with inflammation in breast cancer. *Oncol. Lett.* **2018**, *15*, 2431–2440. [CrossRef]
18. Tenti, P.; Vannucci, L. Lysyl oxidases: Linking structures and immunity in the tumor microenvironment. *Cancer Immunol. Immunother.* **2020**, *69*, 223–235. [CrossRef]
19. Ma, L.; Huang, C.; Wang, X.J.; Xin, D.E.; Wang, L.S.; Zou, Q.L.C.; Zhang, Y.N.S.; Tan, M.D.; Wang, Y.M.; Zhao, T.C.; et al. Lysyl Oxidase 3 Is a Dual-Specificity Enzyme Involved in STAT3 Deacetylation and Deacetylimination Modulation. *Mol. Cell* **2017**, *65*, 296–309. [CrossRef]
20. Santamaria, P.G.; Floristan, A.; Fontanals-Cirera, B.; Vazquez-Naharro, A.; Santos, V.; Morales, S.; Yuste, L.; Peinado, H.; Garcia-Gomez, A.; Portillo, F.; et al. Lysyl oxidase-like 3 is required for melanoma cell survival by maintaining genomic stability. *Cell Death Differ.* **2018**, *25*, 935–950. [CrossRef]
21. Saatci, O.; Kaymak, A.; Raza, U.; Ersan, P.G.; Akbulut, O.; Banister, C.E.; Sikirzhytski, V.; Tokat, U.M.; Aykut, G.; Ansari, S.A.; et al. Targeting lysyl oxidase (LOX) overcomes chemotherapy resistance in triple negative breast cancer. *Nat. Commun.* **2020**, *11*, 2416. [CrossRef] [PubMed]

22. Le Calvé, B.; Griveau, A.; Vindrieux, D.; Maréchal, R.; Wiel, C.; Svrcek, M.; Gout, J.; Azzi, L.; Payen, L.; Cros, J.; et al. Lysyl oxidase family activity promotes resistance of pancreatic ductal adenocarcinoma to chemotherapy by limiting the intratumoral anticancer drug distribution. *Oncotarget* **2016**, *7*, 32100–32112. [CrossRef]
23. Yan, H.; Parsons, D.W.; Jin, G.; McLendon, R.; Rasheed, B.A.; Yuan, W.; Kos, I.; Batinic-Haberle, I.; Jones, S.; Riggins, G.J.; et al. IDH1 and IDH2 mutations in gliomas. *N. Engl. J. Med.* **2009**, *360*, 765–773. [CrossRef] [PubMed]
24. Louis, D.N.; Perry, A.; Wesseling, P.; Brat, D.J.; Cree, I.A.; Figarella-Branger, D.; Hawkins, C.; HK, N.; Pfister, S.M.; Reifenberger, G.; et al. The 2021 WHO Classification of Tumors of the Central Nervous System: A summary. *Neuro-Oncology* **2021**, *23*, 1231–1251. [CrossRef] [PubMed]
25. Chan, A.K.Y.; Yao, Y.; Zhang, Z.; Shi, Z.; Chen, L.; Chung, N.Y.F.; Liu, J.S.M.; Li, K.K.W.; Chan, D.T.M.; Poon, W.S.; et al. Combination genetic signature stratifies lower-grade gliomas better than histological grade. *Oncotarget* **2015**, *6*, 20885–20901. [CrossRef] [PubMed]
26. Sasaki, M.; Knobbe, C.B.; Itsumi, M.; Elia, A.J.; Harris, I.S.; Chio, I.I.; Cairns, R.A.; McCracken, S.; Wakeham, A.; Haight, J.; et al. D-2-hydroxyglutarate produced by mutant IDH1 perturbs collagen maturation and basement membrane function. *Genes Dev.* **2012**, *26*, 2038–2049. [CrossRef] [PubMed]
27. Da Silva, R.; Uno, M.; Nagahashi Marie, S.K.; Oba-Shinjo, S.M. LOX Expression and Functional Analysis in Astrocytomas and Impact of IDH1 Mutation. *PLoS ONE* **2015**, *10*, e0119781. [CrossRef]
28. Miroshnikova, Y.A.; Mouw, J.K.; Barnes, J.M.; Pickup, M.W.; Lakins, J.N.; Kim, Y.; Lobo, K.; Persson, A.I.; Reis, G.F.; McKnight, T.R.; et al. Tissue mechanics promote IDH1-dependent HIF1α-tenascin C feedback to regulate glioblastoma aggression. *Nat. Cell Biol.* **2016**, *18*, 1336–1345. [CrossRef]
29. Tao, B.; Song, Y.; Wu, Y.; Yang, X.; Peng, T.; Peng, L.; Xia, K.; Xia, X.; Chen, L.; Zhong, C. Matrix stiffness promotes glioma cell stemness by activating BCL9L/Wnt/β-catenin signaling. *Aging* **2021**, *13*, 5284–5296. [CrossRef]
30. Sethi, A.; Mao, W.; Wordinger, R.J.; Clark, A.F. Transforming growth factor-β induces extracellular matrix protein cross-linking lysyl oxidase (LOX) genes in human trabecular meshwork cells. *Investig. Ophthalmol. Vis. Sci.* **2011**, *52*, 5240–5250. [CrossRef]
31. Vallet, S.D.; Ricard-Blum, S. Lysyl oxidases: From enzyme activity to extracellular matrix cross-links. *Essays Biochem.* **2019**, *63*, 349–364. [CrossRef] [PubMed]
32. Lucero, H.A.; Kagan, H.M. Lysyl oxidase: An oxidative enzyme and effector of cell function. *Cell. Mol. Life Sci.* **2006**, *63*, 2304–2316. [CrossRef] [PubMed]
33. Chen, L.; Li, S.; Li, W. LOX/LOXL in pulmonary fibrosis: Potential therapeutic targets. *J. Drug Target.* **2018**, *27*, 790–796. [CrossRef]
34. Marie, S.K.; Okamoto, O.K.; Uno, M.; Hasegawa, A.P.; Oba-Shinjo, S.M.; Cohen, T.; Camargo, A.A.; Kosoy, A.; Carlotti, C.G., Jr.; Toledo, S.; et al. Maternal embryonic leucine zipper kinase transcript abundance correlates with malignancy grade in human astrocytomas. *Int. J. Cancer* **2008**, *122*, 807–815. [CrossRef] [PubMed]
35. Barker, H.E.; Cox, T.R.; Erler, J.T. The rationale for targeting the LOX family in cancer. *Nat. Rev. Cancer* **2012**, *12*, 540–552. [CrossRef] [PubMed]
36. Payne, S.L.; Hendrix, M.J.; Kirschmann, D.A. Paradoxical roles for lysyl oxidases in cancer—A prospect. *J. Cell. Biochem.* **2007**, *101*, 1338–1354. [CrossRef]
37. Kirschmann, D.A.; Seftor, E.A.; Fong, S.F.T.; Nieva, D.R.C.; Sullivan, C.M.; Edwards, E.M.; Sommer, P.; Csiszar, K.; Hendrix, M.J.C. A molecular role for lysyl oxidase in breast cancer invasion. *Cancer Res.* **2002**, *62*, 4478–4483.
38. Nishioka, T.; Eustace, A.; West, C. Lysyl oxidase: From basic science to future cancer treatment. *Cell Struct. Funct.* **2012**, *37*, 75–80. [CrossRef]
39. Johnston, K.A.; Lopez, K.M. Lysyl oxidase in cancer inhibition and metastasis. *Cancer Lett.* **2018**, *417*, 174–181. [CrossRef]
40. Erler, J.T.; Bennewith, K.L.; Cox, T.R.; Lang, G.; Bird, D.; Koong, A.; Le, Q.T.; Giaccia, A.J. Hypoxia-Induced Lysyl Oxidase Is a Critical Mediator of Bone Marrow Cell Recruitment to Form the Premetastatic Niche. *Cancer Cell* **2009**, *15*, 35–44. [CrossRef]
41. Dang, L.; White, D.W.; Gross, S.; Bennett, B.D.; Bittinger, M.A.; Driggers, E.M.; Fantin, V.R.; Jang, H.G.; Jin, S.; Keenan, M.C.; et al. Cancer-associated IDH1 mutations produce 2-hydroxyglutarate. *Nature* **2010**, *465*, 966. [CrossRef] [PubMed]
42. Shi, J.; Zuo, H.; Ni, L.; Xia, L.; Zhao, L.; Gong, M.; Nie, D.; Gong, P.; Cui, D.; Shi, W.; et al. An IDH1 mutation inhibits growth of glioma cells via GSH depletion and ROS generation. *Neurol. Sci.* **2014**, *35*, 839–845. [CrossRef] [PubMed]
43. Li, F.; He, X.; Ye, D.; Lin, Y.; Yu, H.; Yao, C.; Huang, L.; Zhang, J.; Wang, F.; Xu, S.; et al. $NADP^+$-IDH Mutations Promote Hypersuccinylation that Impairs Mitochondria Respiration and Induces Apoptosis Resistance. *Mol. Cell* **2015**, *60*, 661–675. [CrossRef]
44. Xu, W.; Yang, H.; Liu, Y.; Yang, Y.; Wang, P.; Kim, S.H.; Ito, S.; Yang, C.; Wang, P.; Xiao, M.T.; et al. Oncometabolite 2-hydroxyglutarate is a competitive inhibitor of α-ketoglutarate-dependent dioxygenases. *Cancer Cell* **2011**, *19*, 17–30. [CrossRef]
45. Zhao, S.; Lin, Y.; Xu, W.; Jiang, W.; Zha, Z.; Wang, P.; Yu, W.; Li, Z.; Gong, L.; Peng, Y.; et al. Glioma-derived mutations in IDH1 dominantly inhibit IDH1 catalytic activity and induce HIF-1α. *Science* **2009**, *324*, 261–265. [CrossRef] [PubMed]
46. Gilkes, D.M.; Semenza, G.L.; Wirtz, D. Hypoxia and the extracellular matrix: Drivers of tumour metastasis. *Nat. Rev. Cancer* **2014**, *14*, 430–439. [CrossRef]
47. Winkler, J.; Abisoye-Ogunniyan, A.; Metcalf, K.J.; Werb, Z. Concepts of extracellular matrix remodelling in tumour progression and metastasis. *Nat. Commun.* **2020**, *11*, 5120. [CrossRef]

48. Chang, Y.Z.; Li, G.Z.; Pang, B.; Zhang, K.N.; Zhang, X.H.; Wang, Y.Z.; Jiang, Z.L.; Chai, R.C. Transcriptional Characteristics of IDH-Wild Type Glioma Subgroups Highlight the Biological Processes Underlying Heterogeneity of IDH-Wild Type WHO Grade IV Gliomas. *Front. Cell Dev. Biol.* **2020**, *8*, 580464. [CrossRef]
49. Wong, C.C.; Gilkes, D.M.; Zhang, H.; Chen, J.; Wei, H.; Chaturvedi, P.; Fraley, S.I.; Wong, C.M.; Khoo, U.S.; Ng, I.O.; et al. Hypoxia-inducible factor 1 is a master regulator of breast cancer metastatic niche formation. *Proc. Natl. Acad. Sci. USA* **2011**, *108*, 16369–16374. [CrossRef]
50. Xie, Q.; Xie, J.; Tian, T.; Ma, Q.; Zhang, Q.; Zhu, B.; Cai, X. Hypoxia triggers angiogenesis by increasing expression of LOX genes in 3-D culture of ASCs and ECs. *Exp. Cell Res.* **2017**, *352*, 157–163. [CrossRef]
51. Kim, S.N.; Jeibmann, A.; Halama, K.; Witte, H.T.; Wälte, M.; Matzat, T.; Schillers, H.; Faber, C.; Senner, V.; Paulus, W.; et al. ECM stiffness regulates glial migration in Drosophila and mammalian glioma models. *Development* **2014**, *141*, 3233–3242. [CrossRef] [PubMed]
52. Huang, S.P.; Chiou, J.; Jan, Y.H.; Lai, T.C.; Yu, Y.L.; Hsiao, M.; Lin, Y.F. Over-expression of lysyl oxidase is associated with poor prognosis and response to therapy of patients with lower grade gliomas. *Biochem. Biophys. Res. Commun.* **2018**, *501*, 619–627. [CrossRef]
53. Lee, G.H.; Kim, D.S.; Chung, M.J.; Chae, S.W.; Kim, H.R.; Chae, H.J. Lysyl oxidase-like-1 enhances lung metastasis when lactate accumulation and monocarboxylate transporter expression are involved. *Oncol. Lett.* **2011**, *2*, 831–838. [CrossRef] [PubMed]
54. Zeltz, C.; Pasko, E.; Cox, T.R.; Navab, R.; Tsao, M.S. LOXL1 Is Regulated by Integrin α11 and Promotes Non-Small Cell Lung Cancer Tumorigenicity. *Cancers* **2019**, *11*, 705. [CrossRef] [PubMed]
55. Peinado, H.; Del Carmen Iglesias-de la Cruz, M.; Olmeda, D.; Csiszar, K.; Fong, K.S.; Vega, S.; Nieto, M.A.; Cano, A.; Portillo, F. A molecular role for lysyl oxidase-like 2 enzyme in snail regulation and tumor progression. *EMBO J.* **2005**, *24*, 3446–3458. [CrossRef]
56. Eiseler, T.; Köhler, C.; Nimmagadda, S.C.; Jamali, A.; Funk, N.; Joodi, G.; Storz, P.; Seufferlein, T. Protein Kinase D1 Mediates Anchorage-dependent and -independent Growth of Tumor Cells via the Zinc Finger Transcription Factor Snail1. *J. Biol. Chem.* **2012**, *287*, 32367–32380. [CrossRef]
57. Koorman, T.; Jansen, K.A.; Khalil, A.; Haughton, P.D.; Visser, D.; Ratze, M.A.K.; Haakma, W.E.; Sakalauskaite, G.; van Diest, P.J.; de Rooij, J.; et al. Spatial collagen stiffening promotes collective breast cancer cell invasion by reinforcing extracellular matrix alignment. *Oncogene* **2022**, *41*, 2458–2469. [CrossRef]
58. Tao, C.; Huang, K.; Shi, J.; Hu, Q.; Li, K.; Zhu, X. Genomics and Prognosis Analysis of Epithelial-Mesenchymal Transition in Glioma. *Front. Oncol.* **2020**, *10*, 183. [CrossRef]
59. Ishihara, S.; Haga, H. Matrix Stiffness Contributes to Cancer Progression by Regulating Transcription Factors. *Cancers* **2022**, *14*, 1049. [CrossRef]
60. Kolacna, L.; Bakesova, J.; Varga, F.; Kostakova, E.; Planka, L.; Necas, A.; Lukas, D.; Amler, E.; Pelouch, V. Biochemical and biophysical aspects of collagen nanostructure in the extracellular matrix. *Physiol. Res.* **2007**, *56*, S51–S60. [CrossRef]
61. Exposito, J.Y.; Cluzel, C.; Garrone, R.; Lethias, C. Evolution of collagens. *Anat. Rec.* **2002**, *268*, 302–316. [CrossRef] [PubMed]
62. Jiang, L.W.; Wang, X.F.; Wu, Z.Y.; Lin, P.H.; Du, H.P.; Wang, S.; Li, L.H.; Fang, N.; Zhuo, S.M.; Kang, D.Z.; et al. Label-free detection of fibrillar collagen deposition associated with vascular elements in glioblastoma multiforme by using multiphoton microscopy. *J. Microsc.* **2017**, *265*, 207–213. [CrossRef] [PubMed]
63. Fujita, A.; Sato, J.R.; Festa, F.; Gomes, L.R.; Oba-Shinjo, S.M.; Marie, S.K.N.; Ferreira, C.E.; Sogayar, M.C. Identification of COL6A1 as a differentially expressed gene in human astrocytomas. *Genet Mol. Res.* **2008**, *7*, 371–378. [CrossRef]
64. Turtoi, A.; Blomme, A.; Bianchi, E.; Maris, P.; Vannozzi, R.; Naccarato, A.G.; Delvenne, P.; De Pauw, E.; Bevilacqua, G.; Castronovo, V. Accessibilome of Human Glioblastoma: Collagen-VI-α-1 Is a New Target and a Marker of Poor Outcome. *J. Proteome Res.* **2014**, *13*, 5660–5669. [CrossRef] [PubMed]
65. Lin, H.; Yang, Y.; Hou, C.X.; Zheng, J.T.; Lv, G.Z.; Mao, R.; Xu, P.H.; Chen, S.W.; Zhou, Y.J.; Wang, P.; et al. Identification of COL6A1 as the Key Gene Associated with Antivascular Endothelial Growth Factor Therapy in Glioblastoma Multiforme. *Genet. Test. Mol. Biomark.* **2021**, *25*, 334–345. [CrossRef]
66. Hautala, T.; Byers, M.G.; Eddy, R.L.; Shows, T.B.; Kivirikko, K.I.; Myllylä, R. Cloning of human lysyl hydroxylase: Complete cDNA-derived amino acid sequence and assignment of the gene (PLOD) to chromosome 1p36.3–p36.2. *Genomics* **1992**, *13*, 62–69. [CrossRef]
67. Jover, E.; Silvente, A.; Marin, F.; Martinez-Gonzalez, J.; Orriols, M.; Martinez, C.M.; Maria Puche, C.; Valdes, M.; Rodriguez, C.; Hernandez-Romero, D. Inhibition of enzymes involved in collagen cross-linking reduces vascular smooth muscle cell calcification. *FASEB J.* **2018**, *32*, 4459–4469. [CrossRef]
68. Gong, S.; Wu, C.; Koehler, F.; Meixensberger, J.; Schopow, N.; Kallendrusch, S. Procollagen-Lysine, 2-Oxoglutarate 5-Dioxygenase Family: Novel Prognostic Biomarkers and Tumor Microenvironment Regulators for Lower-Grade Glioma. *Front. Cell. Neurosci.* **2022**, *16*, 838548. [CrossRef]
69. Gong, S.; Duan, Y.; Wu, C.; Osterhoff, G.; Schopow, N.; Kallendrusch, S. A Human Pan-Cancer System Analysis of Procollagen-Lysine, 2-Oxoglutarate 5-Dioxygenase 3 (PLOD3). *Int. J. Mol. Sci.* **2021**, *22*, 9903. [CrossRef]
70. Qi, Y.; Xu, R. Roles of PLODs in Collagen Synthesis and Cancer Progression. *Front. Cell Dev. Biol.* **2018**, *6*, 66. [CrossRef]
71. Ito, S.; Nagata, K. Roles of the endoplasmic reticulum-resident, collagen-specific molecular chaperone Hsp47 in vertebrate cells and human disease. *J. Biol. Chem.* **2019**, *294*, 2133–2141. [CrossRef] [PubMed]

72. Ishida, Y.; Nagata, K. Hsp47 as a collagen-specific molecular chaperone. *Methods Enzym.* **2011**, *499*, 167–182. [CrossRef]
73. Zhao, D.; Jiang, X.; Yao, C.; Zhang, L.; Liu, H.; Xia, H.; Wang, Y. Heat shock protein 47 regulated by miR-29a to enhance glioma tumor growth and invasion. *J. Neurooncol.* **2014**, *118*, 39–47. [CrossRef] [PubMed]
74. Bird, J.L.E.; Tyler, J.A. Dexamethasone potentiates the stimulatory effect of insulin-like growth factor-I on collagen production in cultured human fibroblasts. *J. Endocrinol.* **1994**, *142*, 571–579. [CrossRef] [PubMed]
75. Guo, S.-K.; Shen, M.-F.; Yao, H.-W.; Liu, Y.-S. Enhanced Expression of TGFBI Promotes the Proliferation and Migration of Glioma Cells. *Cell. Physiol. Biochem.* **2018**, *49*, 1138–1150. [CrossRef]
76. Pan, Y.-B.; Zhang, C.-H.; Wang, S.-Q.; Ai, P.-H.; Chen, K.; Zhu, L.; Sun, Z.-L.; Feng, D.-F. Transforming growth factor beta induced (TGFBI) is a potential signature gene for mesenchymal subtype high-grade glioma. *J. Neurooncol.* **2018**, *137*, 395–407. [CrossRef]
77. Iozzo, R.V.; Sanderson, R.D. Proteoglycans in cancer biology, tumour microenvironment and angiogenesis. *J. Cell. Mol. Med.* **2011**, *15*, 1013–1031. [CrossRef]
78. Miranti, C.K.; Brugge, J.S. Sensing the environment: A historical perspective on integrin signal transduction. *Nat. Cell Biol.* **2002**, *4*, E83–E90. [CrossRef]
79. Wang, X.; Zhou, Q.; Yu, Z.; Wu, X.; Chen, X.; Li, J.; Li, C.; Yan, M.; Zhu, Z.; Liu, B.; et al. Cancer-associated fibroblast-derived Lumican promotes gastric cancer progression via the integrin β1-FAK signaling pathway. *Int. J. Cancer* **2017**, *141*, 998–1010. [CrossRef]
80. Liao, Y.X.; Zhang, Z.P.; Zhao, J.; Liu, J.P. Effects of Fibronectin 1 on Cell Proliferation, Senescence and Apoptosis of Human Glioma Cells Through the PI3K/AKT Signaling Pathway. *Cell. Physiol. Biochem.* **2018**, *48*, 1382–1396. [CrossRef]
81. Rainero, E.; Howe, J.D.; Caswell, P.T.; Jamieson, N.B.; Anderson, K.; Critchley, D.R.; Machesky, L.; Norman, J.C. Ligand-Occupied Integrin Internalization Links Nutrient Signaling to Invasive Migration. *Cell Rep.* **2015**, *10*, 398–413. [CrossRef] [PubMed]
82. Henke, E.; Nandigama, R.; Ergün, S. Extracellular Matrix in the Tumor Microenvironment and Its Impact on Cancer Therapy. *Front. Mol. Biosci.* **2020**, *6*, 160. [CrossRef] [PubMed]
83. Shen, C.J.; Sharma, A.; Vuong, D.V.; Erler, J.T.; Pruschy, M.; Broggini-Tenzer, A. Ionizing radiation induces tumor cell lysyl oxidase secretion. *BMC Cancer* **2014**, *14*, 532. [CrossRef] [PubMed]
84. Trombetta-Lima, M.; Rosa-Fernandes, L.; Angeli, C.B.; Moretti, I.F.; Franco, Y.M.; Mousessian, A.S.; Wakamatsu, A.; Lerario, A.M.; Oba-Shinjo, S.M.; Pasqualucci, C.A.; et al. Extracellular Matrix Proteome Remodeling in Human Glioblastoma and Medulloblastoma. *J. Proteome Res.* **2021**, *20*, 4693–4707. [CrossRef]
85. Krane, S.M. The importance of proline residues in the structure, stability and susceptibility to proteolytic degradation of collagens. *Amino Acids* **2008**, *35*, 703–710. [CrossRef]
86. Szoka, L.; Karna, E.; Hlebowicz-Sarat, K.; Karaszewski, J.; Palka, J.A. Exogenous proline stimulates type I collagen and HIF-1α expression and the process is attenuated by glutamine in human skin fibroblasts. *Mol. Cell. Biochem.* **2017**, *435*, 197–206. [CrossRef]
87. Obara-Michlewska, M.; Szeliga, M. Targeting Glutamine Addiction in Gliomas. *Cancers* **2020**, *12*, 310. [CrossRef]
88. Moreira Franco, Y.E.; Alves, M.J.; Uno, M.; Moretti, I.F.; Trombetta-Lima, M.; de Siqueira Santos, S.; dos Santos, A.F.; Arini, G.S.; Baptista, M.S.; Lerario, A.M.; et al. Glutaminolysis dynamics during astrocytoma progression correlates with tumor aggressiveness. *Cancer Metab.* **2021**, *9*, 18. [CrossRef]
89. Khurshed, M.; Molenaar, R.J.; Lenting, K.; Leenders, W.P.; van Noorden, C.J.F. In silico gene expression analysis reveals glycolysis and acetate anaplerosis in IDH1 wild-type glioma and lactate and glutamate anaplerosis in IDH1-mutated glioma. *Oncotarget* **2017**, *8*, 49165–49177. [CrossRef]
90. Webb, B.A.; Chimenti, M.; Jacobson, M.P.; Barber, D.L. Dysregulated pH: A perfect storm for cancer progression. *Nat. Rev. Cancer* **2011**, *11*, 671–677. [CrossRef]
91. Gatenby, R.A.; Gawlinski, E.T.; Gmitro, A.F.; Kaylor, B.; Gillies, R.J. Acid-mediated tumor invasion: A multidisciplinary study. *Cancer Res.* **2006**, *66*, 5216–5223. [CrossRef]
92. Johnson, L.L.; Pavlovsky, A.G.; Johnson, A.R.; Janowicz, J.A.; Man, C.F.; Ortwine, D.F.; Purchase, C.F.; White, A.D.; Hupe, D.J. A rationalization of the acidic pH dependence for stromelysin-1 (Matrix metalloproteinase-3) catalysis and inhibition. *J. Biol. Chem.* **2000**, *275*, 11026–11033. [CrossRef] [PubMed]
93. Greco, M.R.; Antelmi, E.; Busco, G.; Guerra, L.; Rubino, R.; Casavola, V.; Reshikin, S.J.; Cardone, R.A. Protease activity at invadopodial focal digestive areas is dependent on NHE1-driven acidic pHe. *Oncol. Rep.* **2014**, *31*, 940–946. [CrossRef] [PubMed]
94. Ma, K.; Chen, X.; Liu, W.; Chen, S.; Yang, C.; Yang, J. CTSB is a negative prognostic biomarker and therapeutic target associated with immune cells infiltration and immunosuppression in gliomas. *Sci. Rep.* **2022**, *12*, 4295. [CrossRef] [PubMed]
95. Pislar, A.; Jewett, A.; Kos, J. Cysteine cathepsins: Their biological and molecular significance in cancer stem cells. *Semin. Cancer Biol.* **2018**, *53*, 168–177. [CrossRef] [PubMed]
96. Vidak, E.; Javorsek, U.; Vizovisek, M.; Turk, B. Cysteine Cathepsins and Their Extracellular Roles: Shaping the Microenvironment. *Cells* **2019**, *8*, 264. [CrossRef]
97. Mijanovic, O.; Brankovic, A.; Panin, A.N.; Saychuk, S.; Timashev, P.; Ulasov, I.; Lesniak, M.S. Cathepsin B: A sellsword of cancer progression. *Cancer Lett.* **2019**, *449*, 207–214. [CrossRef]
98. Nettesheim, A.; Shim, M.S.; Dixon, A.; Raychaudhuri, U.; Gong, H.; Liton, P.B. Cathepsin B Localizes in the Caveolae and Participates in the Proteolytic Cascade in Trabecular Meshwork Cells. Potential New Drug Target for the Treatment of Glaucoma. *J. Clin. Med.* **2021**, *10*, 78. [CrossRef]

99. Clara, C.A.; Marie, S.K.N.; de Almeida, J.R.W.; Wakamatsu, A.; Oba-Shinjo, S.M.; Uno, M.; Neville, M.; Rosemberg, S. Angiogenesis and expression of PDGF-C, VEGF, CD105 and HIF-1α in human glioblastoma. *Neuropathology* **2014**, *34*, 343–352. [CrossRef]
100. Nakao, S.; Zandi, S.; Sun, D.; Hafezi-Moghadam, A. Cathepsin B-mediated CD18 shedding regulates leukocyte recruitment from angiogenic vessels. *FASEB J.* **2018**, *32*, 143–154. [CrossRef]
101. Tan, D.C.H.; Roth, I.M.; Wickremesekera, A.C.; Davis, P.E.; Kaye, A.H.; Mantamadiotis, T.; Stylli, S.S.; Tan, S.T. Therapeutic Targeting of Cancer Stem Cells in Human Glioblastoma by Manipulating the Renin-Angiotensin System. *Cells* **2019**, *8*, 1364. [CrossRef] [PubMed]
102. Bischof, J.; Westhoff, M.-A.; Wagner, J.E.; Halatsch, M.-E.; Trentmann, S.; Knippschild, U.; Wirtz, C.R.; Burster, T. Cancer stem cells: The potential role of autophagy, proteolysis, and cathepsins in glioblastoma stem cells. *Tumor. Biol.* **2017**, *39*, 1010428317692227. [CrossRef] [PubMed]
103. Prensner, J.R.; Chinnaiyan, A.M. Metabolism unhinged: IDH mutations in cancer. *Nat. Med.* **2011**, *17*, 291–293. [CrossRef] [PubMed]
104. Rick, J.W.; Chandra, A.; Dalle Ore, C.; Nguyen, A.T.; Yagnik, G.; Aghi, M.K. Fibronectin in malignancy: Cancer-specific alterations, protumoral effects, and therapeutic implications. *Semin. Oncol.* **2019**, *46*, 284–290. [CrossRef] [PubMed]
105. Astudillo, P. Extracellular matrix stiffness and Wnt/β-catenin signaling in physiology and disease. *Biochem. Soc. Tran.* **2020**, *48*, 1187–11898. [CrossRef] [PubMed]
106. Li, H.Y.; He, X.J.; Peng, Y.J.; Shao, B.; Duan, H.Y.; Yang, F.; Chen, H.H.; Lan, Q. LOXL1 regulates cell apoptosis and migration in human neuroglioma U87 and U251 cells via Wnt/β-catenin signaling. *Int. J. Clin. Exp. Pathol.* **2018**, *11*, 2032–2037.
107. Soares, R.D.; Laurentino, T.D.; da Silva, C.T.; Goncalves, J.D.; Lerario, A.M.; Marie, S.K.N.; Oba-Shinjo, S.M.; Jasiulionis, M.G. Cellular Model of Malignant Transformation of Primary Human Astrocytes Induced by Deadhesion/Readhesion Cycles. *Int. J. Mol. Sci.* **2022**, *23*, 4471. [CrossRef]
108. Daley, E.J.; Trackman, P.C. β-Catenin mediates glucose-dependent insulinotropic polypeptide increases in lysyl oxidase expression in osteoblasts. *Bone Rep.* **2021**, *14*, 101063. [CrossRef]
109. Gao, J.; Aksoy, B.A.; Dogrusoz, U.; Dresdner, G.; Gross, B.; Sumer, S.O.; Sun, Y.; Jacobsen, A.; Sinha, R.; Larsson, E.; et al. Integrative analysis of complex cancer genomics and clinical profiles using the cBioPortal. *Sci. Signal.* **2013**, *6*, pl1. [CrossRef]
110. Brennan, C.W.; Verhaak, R.G.; McKenna, A.; Campos, B.; Noushmehr, H.; Salama, S.R.; Zheng, S.; Chakravarty, D.; Sanborn, J.Z.; Berman, S.H.; et al. The somatic genomic landscape of glioblastoma. *Cell* **2013**, *155*, 462–477. [CrossRef]
111. Consortium, G. The Genotype-Tissue Expression (GTEx) project. *Nat Genet* **2013**, *45*, 580–585. [CrossRef]
112. Anders, S.; Huber, W. Differential expression analysis for sequence count data. *Genome Biol.* **2010**, *11*, R106. [CrossRef] [PubMed]
113. Naba, A.; Clauser, K.R.; Ding, H.M.; Whittaker, C.A.; Carr, S.A.; Hynes, R.O. The extracellular matrix: Tools and insights for the "omics" era. *Matrix Biol.* **2016**, *49*, 10–24. [CrossRef] [PubMed]

Publicação 3

Dysregulation of microtubule dynamics caused by LOXL3 knockout triggers mitosis catastrophe and senescence in U87MG and U251 cells

6 Publicação 3 - Dysregulation of microtubule dynamics caused by LOXL3 knockout triggers mitosis catastrophe and senescence in U87MG and U251 cells

Submetido em 06 de dezembro de 2023

Objetivo geral: Detalhar o papel funcional de LOXL3 através do nocaute gênico, via CRIPR-Cas9, nas linhagens celulares de GBM, U87MG e U251.

a) Realizar o nocaute permanente de *LOXL3* via CRISPR-Cas9
b) Avaliar o efeito do nocaute de LOXL3 na viabilidade e morfologia celular
c) Realizar o sequenciamento do transcriptoma e a análise de enriquecimento de genes diferencialmente expressos nas células com nocaute para *LOXL3* em relação ao controle, para identificar as vias de sinalização nas quais LOXL3 esteja envolvido;
d) Avaliar o envolvimento de LOXL3 com a tubulina e com os genes envolvidos com o microtúbulo.
e) Avaliar o efeito do nocaute de LOXL3 no ciclo celular e analisar a expressão dos genes envolvidos neste processo.
f) Avaliar o efeito do nocaute de LOXL3 na morfologia nuclear, morte celular e os genes envolvidos nestes processos.
g) Avaliar o efeito do nocaute de LOXL3 na adesão e migração celular.
h) Analisar a expressão *in silico* dos genes encontrados diferencialmente expressos após o nocaute de LOXL3 através da análise de dados de transcriptoma de banco público.

Dysregulation of microtubule dynamics caused by *LOXL3* knockout triggers mitosis catastrophe and senescence in U87MG and U251 cells

Talita de Sousa Laurentino[1*], Roseli da Silva Soares[1], Antonio Marcondes Lerário[2], Ricardo Cesar Cintra[3], Suely Kazue Nagahashi Marie[1] and Sueli Mieko Oba-Shinjo[1*]

[1]Cellular and Molecular Biology Laboratory (LIM 15), Neurology Department, Faculdade de Medicina FMUSP, Universidade de Sao Paulo, Sao Paulo, SP, Brazil

[2]Department of Internal Medicine, Division of Metabolism, Endocrinology, and Diabetes, University of Michigan, Ann Arbor, Michigan, USA

[3]Centro de Investigação Translacional em Oncologia, Instituto do Câncer do Estado de São Paulo (ICESP), São Paulo, Brazil; Department of Radiology and Oncology, Faculdade de Medicina, Universidade de São Paulo, São Paulo, Brazil.

* Correspondence: talitalaurentino@usp.br; suelimoba@usp.br; Tel.: +55-11-3061-8310

Abstract

LOXL3, an amine oxidase, plays a role in tumorigenesis and tumor progression, and is upregulated in glioblastoma (GBM). LOXL3 is involved in adhesion, migration and proliferation of GBM cells and correlated with tubulin expression. As the major component of cytoskeleton, microtubules are essential for cell cycle and mitotic progression. Here, we performed a LOXL3 knockout using CRISPR-Cas9 in two GBM cell lines, U87MG and U251, to achieve high silencing efficiency. *LOXL3*-knockout promoted a decrease of cell viability in both cell lines. Transcriptome enrichment analysis showed that genes related to tubulin acetylation were downregulated in U87MG cells. Western blot analysis confirmed the decrease in tubulin acetylation. Additionally, downregulation of genes related to the cell cycle and proliferation was observed in both U87MG and U251 cells. Functional assays confirmed that *LOXL3*-knockout cells presented a delay in cell cycle progression and a strong alteration in mitotic spindles in metaphase-anaphase stages. Nuclear morphology analysis demonstrated alterations in nuclear morphology related to mitotic catastrophe and senescence in U87MG and U251 cells, respectively. Cell adhesion and migration were also decreased in the *LOXL3*-knockout clones. Analysis of RNAseq of TCGA database showed a positive correlation between LOXL3 expression and genes involved in cell cycle, cell death and senescence of GBM cases with mutated *TP53*. Interestingly, coexpression of *LOXL3* and *CCNE1* influenced the survival of GBM patients with *TP53* mutations, indicating a potential combinatory therapeutic target for treating *TP53*-mutated GBM cases.

Introduction

Glioblastoma (GBM) is a histological subtype of glioma and is the most commonly occurring malignant brain and other central nervous system histopathology, accounting for 14.2% of all tumors and 50.9% of all malignant tumors. GBM patients have a median of survival of eight months, irrespective of whether individuals receive any treatment for their tumors (1). GBM is a heterogeneous tumor, as evidenced by the landscape of somatic alteration analysis affecting different pathways such as p53, RB and PI3K (2). Recently, astrocytomas were re-classified according to genetic characteristics and IDH mutational status (3). Additionally, GBM is subdivided according to molecular alterations into proneural, classical and mesenchymal (4).

LOXL3, a copper-dependent amine oxidase belonging to the lysyl oxidase family, catalyzes crosslinking of collagen and elastin, which contributes to extracellular matrix stiffness and stabilization (5-7). Along with amine oxidase activity, LOXL3 is described involved in the modulation STAT3 deacetylation of lysine residues (8). LOXL3 plays a crucial role in development, tumorigenesis, tumor progression, and chemoresistance (9-13). Our previous study demonstrated that the expression of LOXL3 correlated with malignancy grade in low-grade gliomas with wildtype *IDH*, a factor of poor prognosis (12). Additionally, LOXL3 is upregulated in GBM, contributing to poorer prognosis of patients, and LOXL3 expression is strongly correlated with the expression of genes coding for tubulins (11).

Microtubules (MTs) are major component of the eukaryotic cytoskeleton, and are uniformly assembled from conserved α/β heterodimers. MTs exhibit cycles of growth, shortening, and regrowth, which is an energy-consuming process termed dynamic instability. The dynamics and architecture of MT depend on the binding of MT-associated

proteins (MAPs). MAPs are a vast and complex family that bind to and stabilize the MT lattice (14). MT recognition/binding by MAPs may be affected by diverse post-translational modification (PTM) of tubulin (15), such as acetylation. Acetylation/deacetylation of tubulin is mediated by acetyltransferases and deacetylases. α-TAT1 is the most well studied enzyme responsible for catalyzing α-tubulin Lys40 acetylation. In contrast, HDAC5/6 and sirtuin 2 mediate the tubulin deacetylation. Acetylation plays an important role in MT stability and prevents MT breakage, thereby prolonging MT longevity, enhancing MT flexibility, and ultimately preventing structural damage (16). During interphase, MTs facilitate the capture of organelles, promote transport and reorganization (17), and regulate cell shape, adhesion, and migration, which are processes strongly controlled by MT acetylation (18). During mitotic spindle formation, dynamic MTs attach to the chromosomes. The mitotic spindle, midbody, and kinetochore MTs contain high levels of acetylated α-tubulin (14).

We performed a *LOXL3* knockout using CRISPR-Cas9 in U87MG and U251 GBM cell lines to better understand the role of LOXL3 in glioblastoma. Loss of LOXL3 strongly altered MT acetylation, triggering a decrease in cell viability, mitotic catastrophe, and senescence. *LOXL3*-knockout promoted *CCNE1* downregulation. In GBM samples, *LOXL3* expression positively correlated with *CCNE1* expression levels in cases with mutated *TP53* (mutTP53) but not with wild type *TP53* (wtTP53), and low expression of both genes was associated with a longer overall survival. Our data suggest a potential combination therapy targeting both *LOXL3* and *CCNE1* in GBM cases with *TP53* mutations.

Results

LOXL3 knockout by CRISPR-Cas9 of GBM cell lines

The role of LOXL3 in GBM was investigated using CRISPR-Cas9 gene editing to generate LOXL*3*-knockdown in two GBM cell lines, U87MG and U251. Two sgRNAs were designed for exon 2 in the coding region of *LOXL3*, followed by cloning of sgRNAs into the pSpCas9 (BB) vector, as showed Fig. 1a. Cells were transfected and clonal single-cell populations were obtained and sequenced, and different genomic alterations were confirmed, as conversion (clone 1 of U87Mg cells) and deletions of different sizes (clone 2 of U87MG cells and clones 1 and 2 of U251 cells) (Fig. S1b). *LOXL3*-knockout clones with the lowest LOXL3 protein levels analyzed by Western blotting were named clones 1 and 2 (Fig. 1b). LOXL3 expression was 13.9% and 21.8% (silencing of 86.1% and 78.2%) for U87MG-derived clones, and 41.6% and 62.12% (silencing 58.4% and 37.9%) for U251-derived clones when compared to the controls, respectively (Fig. 1c). *LOXL3*-knockout resulted in changes in cell morphology, with the cells exhibiting larger sizes when compared to control cells, more evidently in the clones with the lowest LOXL3 expression (clone 1 for both cell lines). Next, we compared the cell proliferation rates between *LOXL3*-knockout clones and control cells. The silencing of LOXL3 significantly affected cell viability, predominantly in clone 1, resulting in 1.7×, 1.8× and 1.5×-decrease in viability for U87MG and 2×, 3.14× and 5.6×-decrease for U251 cell lines in comparison to the control (empty vector) at 48, 72 and 96 h (Fig.1. e-f). Next, transcriptome analysis of *LOXL3*-knockout and control cells was performed to better understand the altered signaling pathways by *LOXL3* knockout. The analysis was performed based on the most efficient LOXL3 knocked out clone 1 in both cell lines. In total, 12,846 and 12,975 genes were mapped for U87MG and U251 cells, and 921 and 1,974 differentially expressed genes (DEGs) were identified between *LOXL3*-knockout and control cells for U87MG and U251 cells (log_2 fold change ≥0.5 and ≤-0.5, and adjusted by p value ≤ 0.05). Among these, 520 and 1,074 genes were

downregulated, whereas 401 and 900 genes were upregulated in U87MG and U251, respectively (Table, S1). Enrichment analysis of DEGs was performed using Gene Ontology (GO). The top 5 GOs Biological Processes downregulated and upregulated in *LOXL3*-knockout U87MG and U251 cells are described in Fig. 1 g-i and detailed in the supplementary material (Table S2). Notably, cell cycle (GO:0007049) and cell division (GO:0051301) pathways were downregulated in both cell lines, corroborating the decreased cell proliferation. Additionally, negative regulation of the tubulin acetylation pathway (GO:1904428) was downregulated in U87MG cells, whereas DNA repair (GO:0006281) and cellular response to DNA damage stimulus (GO:0006974) were downregulated in U251 cells.

LOXL3-knockout significantly influenced tubulin acetylation in U87MG and U251 cell lines

Tubulin acetylation was investigated by Western blotting (Fig.2 a). Downregulation of LOXL3 significantly reduced the acetylation of α-tubulin compared to the control, mostly in U87MG cells, confirming transcriptome analysis. Tubulin acetylation levels decreased by approximately 4.6× and 3× decrease in clones 1 and 2 compared with the control in U87MG cells, respectively, while *LOXL3*-knockout U251 clones showed an approximately 1.5×-decrease of acetylated α-tubulin for both clones compared with the control (Fig.2 b). The differences observed in the levels of post-translational modification (PTM) in *LOXL3*-knockout U87MG and U251 clones may be attributed to LOXL3 expression levels after knockout. Additionally, immunofluorescence staining analysis was performed to evaluate distribution of the acetylated α-tubulin in both cell types. *LOXL3*-knockout clones presented a lower distribution of acetylated α-tubulin compared to control cells

in both U87MG and U251 cell lines (Fig.2 c). Among the upregulated and downregulated genes, including those involved in “negative regulation of tubulin acetylation”, were key genes that code for MAPs, such as *MAPT*, which codes for Tau protein, and *FRY,* which codes for FRY protein in *LOXL3*-knockout U87MG clones. In addition, it was observed an increase in the expression of *ATAT1* and *HDAC5*, genes that code for α-TAT1 and histone deacetylase 5, respectively, which are key proteins involved in tubulin acetylation/deacetylation (Fig.2 d). In contrast, *LOXL3*-knockout U251 clone 1 upregulated the expression of genes that code for the same MAPs (*MAPT* and *FRY*). Conversely, *HDAC5* expression was upregulated in U251 clone 1, similar to U87MG clone 1. There were no differences in *ATAT1* gene expression between the *LOXL3*-knockout and control U251 cells.

LOXL3-knockout promoted a delay on cell cycle and cell division progress

Cell cycle progression was investigated using flow cytometry as *LOXL3*-knockout cells presented lower proliferation rates and downregulated DEGs involved in the cell cycle. Delays in the cell cycle progression were observed in both the *LOXL3*-knockout U87MG and U251 cell lines. Cell cycle progression was monitored 12, 24, and 36 h after synchronization. Notably, the LOXL3-knockout clone 1 in U87MG cells exhibited cell cycle arrest in the G2/M phase at the 12-hour, and in the G1 phase after 36 h. In contrast, the *LOXL3*-knockout U251 clones demonstrated arrest in both the S and G2/M phases for clone 1 and the S phase for clone 2 at the 36-hour time point (Fig.3 a-b). Representative histograms displaying the phases of cell cycle progression in control samples and *LOXL3*-knockout clones in U87MG and U251, respectively (Fig.3 c-d). A DEG set list related to the cell cycle phases was analyzed in *LOXL3*-knockout clones and control samples.

Several genes associated with different cell cycle phases were downregulated compared to the respective control groups in both U87MG and U251 cell lines (Fig.3 e-f). In *LOXL3*-knockout U87MG clones key genes related to p53 regulation (*MDM2* and *CDKN1A*), exit from mitosis, and the onset of a new G1 phase (*HSPA2* and *CDC14B*), associated with MAPs (*MAP10*), were also downregulated (Fig.3 e). For *LOXL3*-knockout U251 cells, key genes related to the decision window to G1/S transition (*CCNE1* and *CDC7*), involved in checkpoint (*RAD51C*, *RAD54B*, *BRCA1*, and *ATM*), mitosis (*CEP72*, *CEP85*, and *CENPS*), were downregulated exclusively in *LOXL3*-knockout U251 cells (mutTP53) (Fig.3 f). In contrast, *MDM1* and *MAD1L1*, that code for a microtubule-binding protein and a component spindle-assembly checkpoint, respectively, were upregulated in *LOXL3*-knockout U87MG cells (Fig.3 g). *HDAC2*, which codes for histone deacetylase 1 involved in S phase, was also upregulated in U87MG cells with *LOXL3* knocked out (Fig.3 g). In *LOXL3*-knockout U251 cells, *INCA1* and *HDAC3*, which code for a CDK inhibitor and histone deacetylase 5 involved in S-phase, respectively, and similar to U87MG cells, *MAD1L1* were upregulated (Fig. 3h). The upregulated genes are presented as $\log_2$ fold changes (logFC) of clones 1 and 2 relative to the control. MT acetylation was evaluated in the metaphase and anaphase stages of mitosis by immunofluorescence staining in *LOXL3*-knockout clones and controls in both cell lines. The results demonstrated a significant reduction of acetylated tubulin predominantly in clone 1 of both U87MG and U251 cells, corroborating the Western blot analysis (Fig. 2 b), resulting in aberrant mitotic figures. Notably, damage to the structure of mitotic spindle fibers was observed in *LOXL3*-knockout U251 clone 1 cells when compared to the control cells, resulting in multipolar mitosis (Fig.4).

Nuclear morphology and cell death are altered after knockout of *LOXL3*

The impact of MT destabilization was assessed using analysis of the nuclei morphology by nuclear morphometric analysis (NMA) tool based on the nuclear irregularity index (NII). An increase of irregular and large regular populations, which can be associated to mitotic catastrophe and senescence in *LOXL3*-knockout clone 1 U87MG and U251 cells, respectively (Fig.5 a-b). Next, we analyzed the effect of *LOXL3*-knockout on cell death of U87MG and U251 cell lines, before and after treatment with temozolomide (TMZ). In clone 1 U87MG cells, the absence of *LOXL3* expression *per si* caused an increase in cell death in the early stage. TMZ treatment increased the cell population in the early stages of apoptosis (Fig.5 c). On the other hand, U251 clones with knocked out LOXL3 did not show increased cell death when compared to control cells before or after TMZ treatment (Fig.5 d). Only clone 2 U251 cells showed an increased cell population in late apoptosis without TMZ treatment. Representative scatter plots of cell death analysis by flow cytometry are shown in Fig.5 e-f. These data reinforce the clear differences in the influence of *LOXL3*-knockout in U87MG and U251 cells. Therefore, we analyzed genes associated with cell death, mitotic catastrophe and senescence. The logFC of clones 1 and 2 of U87MG and U251 cells relative to respective controls are presented in Fig.5 g. Genes related to anti-senescence, such as *CCNB1*, *CCNE1*, *E2F1/3*, and cell death, were among the downregulated genes, mainly in the clone 1 U251 cells. Additionally, these cells also showed upregulation of pro-senescence genes, such as *SMAD2*, *RBL2*, and mainly *CDKN1A* and *CDKN1B*, which code for p21 and p27, markers of senescence (Fig.5 g). Conversely, LOXL3-knockout U87MG cells showed upregulation of genes related to p53-dependent cell death, namely *HIPK2*, *DYRK2*, *MAPK12* and *APAF1*.

LOXL3-knockout affected the cell adhesion and cell migration

Cell adhesion and migration can be affected by acetylation of MTs; therefore, these processes were analyzed in *LOXL3*-knockout clones. In U87MG *LOXL3*-knockout cells, predominantly in clone 1, there was a significant 1.5× decrease in cell adhesion compared to control cells (Fig.6 a). Nonetheless, in the U251 cell line, LOXL3 knockout did not influence the cell adhesion property (Fig.6 b), possibly due to a minor change in MT acetylation levels. Cell migration was analyzed by wound healing assay, and the scratch areas were monitored at 6, 18 and 24 h. The knockout of LOXL3 resulted in a significant decrease in cell migration in clone 1 of the U87MG cell line at 11.1%, 20.1% and 13.6% after 6, 18 and 24 h, respectively, when compared to the control, while clone 2 showed significantly decreased migration only after 6h relative to control cells (Fig. 6c). In the U251 cell line, *LOXL3*-knockout clone 1 showed a significant reduction in cell migration of 8.3% and 13.6% after 18 and 24-hour time points compared to control cells (Fig.6 d). Representative photomicrographs of the cell migration assays are shown in Fig.6 e.

Differential gene expression analysis of enrichment pathways in TCGA glioblastoma database

Up- and downregulated genes in RNA-seq analysis related to cell cycle phases and MT acetylation (Fig.3 e-g), and apoptosis and senescence (Fig.5 g) were evaluated in GBM samples from the TCGA database, amounting to 85 genes (excluding the duplicated genes) to *LOXL3*-knckout in U87MG and U251 cell lines. Initially, the samples were divided into wtTP53 (n=106) and mutTP53 (n=54), totaling 160 cases. Therefore, to evaluate the level of correlation according TP53 status, Spearman's correlation was performed in the selected database. Among the 85 genes analyzed, 16 genes were

correlated with LOXL3 between the groups (genes that exhibited correlation in at least one of the groups were included in the graph). Interestingly, genes which code for α-TAT1 *(ATAT1)* and MAPs, such as *MAPT* and *FRY*, were negatively correlated with LOXL3, corroborating to the RNA-seq analysis in *LOXL3*-knockout U251 clones. Additionally, the expression of key genes related to the cell cycle and senescence (*CDKN1A*, *CDKN1B*, and *CCNE1)* and S-phase (*TRRAP*, *PRPD1B*, *BRD4*, *MCMPB* and *RUNX3*) correlated positively with *LOXL3* expression. The expression of genes involved in the decision window to G2, checkpoint, and mitosis was positively correlated with *LOXL3* expression (Fig.7 a). An additional analysis of samples based on the molecular subtype classification into G-CIMP, proneural, classical and mesenchymal subtypes was also considered. Genes were categorized into MAP, decision window (G1), S-phase, decision window (G2), checkpoint (G2/M), mitosis and pro-senescence. The heatmap shows the gene expression profile of the gene set list correlated with LOXL3 in the different subtypes and TP53 status groups in TCGA database (Fig. 7 b). Survival analysis was performed to evaluate whether co-expression may affect the outcome of patients with GBM. Gene expression levels were divided into up- and down-expression based on the median of each gene expression. Interestingly, *CCNE1* and *LOXL3* downregulation was associated with an increase in overall survival outcome. Global comparison demonstrated that, *LOXL3* upregulation and *CCNE1* downregulation showed the worst prognosis (green line), while patients that presented *LOXL3* and *CCNE1* downregulation presented better prognosis. GBM cases with both *LOXL3* and *CCNE1* downregulated presented an estimative median of 21.2 months (21.2±6.4; CI: 8.6-33.8; OR: 1.79 and 0.676, for *LOXL3* and *CCNE1*, respectively). Collectively, these results suggest that *LOXL3* and *CCNE1* may be possible targets in GBM patients with *TP53*.

Discussion

LOXL3, a copper-dependent amine oxidase, plays a crucial role in the development, a tumorigenesis and tumor progression (6, 7, 12, 19). LOXL3 is upregulated in GBM, and we demonstrated that LOXL3 is involved in cell viability, cell adhesion and invasion by LOXL3 transitory silencing in GBM cell lines (11). Here, we performed a LOXL3 permanent knockout in U87MG (wtTP53) and U251 (mutTP53) GBM cell lines using CRISPR-Cas9 system. Two clones with the lowest LOXL3 expression were selected from each cell line, named clones 1 and 2, with different LOXL3 knockout levels. Significant enlargement of U87MG and U251 cell size when compared to control cells was observed in *LOXL3*-knockout cells. Moreover, a remarkable decrease in the viability of *LOXL3*-knockout cells was observed in both cell lines, mainly in clone 1, the most efficiently knocked out cell line. These findings corroborate our previous studies on *LOXL3*-silenced cells by transient silencing in U87MG cells, where cell enlargement was associated with an increase in cell adhesion, accompanied by a decrease in viability (11). Similar results were observed in melanoma cells, where LOXL3 silencing decreased viability (20).

Enrichment analysis of pathways utilizing RNA-seq data of LOXL3-knockout cells was conducted to better understand the role of LOXL3 in GBM. Analysis of DEGs revealed that one of the most significantly downregulated enriched pathways was associated with tubulin acetylation in U87MG cells. In fact, acetylated α-tubulin was significantly reduced in *LOXL3*-knockout clones, with a more prominent effect observed in U87MG cells than in U251 cells, probably because of *LOXL3* knockout efficiency. Acetylation has been associated with an enhancement of MT flexibility to prevent structural damage, and related to the polymerization of MT (14, 21). Among the genes related to tubulin

acetylation, *MAPT* and *FRY* were downregulated in the U87MG cells. *MAPT,* which codes for Tau protein, and *FRY*, which codes for the FRY protein, also known as furry, belong to MAPs, and are specifically related to the polymerization and stability of MTs (22, 23). Several studies have demonstrated a relationship between MAPs and Lys40 α-tubulin acetylation (14). Tau protein binds preferentially to acetylated and tyrosinated MTs in neuronal and non-neuronal cells, whereas FRY is involved in MT acetylation in mitotic spindles by inhibiting SIRT2, a tubulin-deacetylase (23-25). In contrast to *LOXL3*-knockout U87MG cells, *LOXL3*-knockout U251 cells showed an increase in the expression of the same MAPs. p53 has been associated with the expression of several MAPs. The decrease in MAP4 expression is associated with p53 induction and can be restored using molecules that prevent p53-mediated transcriptional repression (26, 27). Kinesin and katanin expression, proteins classified as motor proteins and MT-severing, respectively, were also influenced by p53 expression (28, 29). The highest kinesin expression level was detected in p53-mutant cell lines compared to cell lines with wildtype p53, and kinesin silencing effects depend on the *TP53* status (29, 30). In addition, tau protein predicted to interact with p53. *TP53* is upregulated in Alzheimer's disease, and enhanced p53 expression sustains hyperphosphorylation of Tau, resulting in the accumulation of neurofibrillary tangles (NFT), a hallmark of Alzheimer's disease (31). In addition to MAPs, *HDAC5,* which codes for histone deacetylase 5, was upregulated in *LOXL3*-knockout U87MG and U251 cell lines (clones 1), whereas *ATAT1* was upregulated only in U87MG cells. The addition/removal of acetylation occurs in α- and β-tubulin, with α-tubulin Lys40 being the well-studied. Tubulin acetylation mostly catalyzed by α-TAT1 (coded by *ATAT1)*, which is responsible for α-tubulin Lys40 acetylation. Tubulin deacetylation is catalyzed by histone deacetylases 5/6 and sirtuin 2 (32). Although an increase in *ATAT1*

313 expression was observed, no concomitant increase in tubulin acetylation was observed.
314 *In vivo*, the activity of α-TAT1 may be regulated through processes such as
315 phosphorylation, acetylation, and localization of the α-TAT1 enzyme. Furthermore, the
316 involvement of calpain proteins may be a determining factor in modulating α-TAT1
317 activity. (33). Additionally, histone deacetylase 5 was phosphorylated and activated by
318 PKC upon axonal injury, thereby increasing MT deacetylation (34).

319 A significant delay in the cell cycle was observed in the G2/M and G1 phases in *LOXL3*-
320 knockout U87MG clone 1 cells, while *LOXL3*-knockout U251 cells presented a delay in
321 the S, G2/M and S phases, corroborating the transcriptome analysis. Several key genes
322 related to the cell cycle were downregulated when LOXL3 was knocked out in both the
323 U87MG and U251 cells. Failure of chromosomes to attach properly to mitotic spindles or
324 formation of mitotic spindles may result in G2/M cell cycle arrest. Acetylation of α-
325 tubulin is highly abundant in mitotic spindles, midbodies, and kinetochore MTs (14). MT
326 acetylation promotes the recruitment of key proteins, such as PLK1, which is required to
327 maintain bipolar homeostasis (35). Several genes associated with mitotic spindle
328 assembly were identified with altered expression, such as *FRY,* which codes for Furry,
329 related to MT acetylation in the mitotic spindle (23) and CDC14B (coded by *CDC14B*), a
330 dual-specificity phosphatase that promotes MT stabilization through bundle formation
331 (36). CDC14B dephosphorylates E-cadherin in early anaphase, leading to APC/C^{Cdh1}
332 activation and cell division progression (37). *MAP10,* another gene associated with MAPs
333 that was downregulated after LOXL3 knockout, is also associated with MT stability and
334 correct cytokinesis (38). Heat shock protein 70 protein 2 (coded by *HSPA2*), required for
335 the maintenance of functional mitotic centrosomes, was downregulated in *LOXL3*-
336 knockout U87MG and U251 cell lines (39). *MDM1,* one of the genes upregulated in

LOXL3-knockout U87MG cells, is a MT-binding protein that negatively regulates centriole duplication (40). Errors in mitotic spindle formation result in incorrect chromosomal segregation. The spindle assembly checkpoint (SAC) prevents these errors by acting as a surveillance mechanism for unattached or incorrectly attached MT (41). SAC catalyzes formation of the mitotic checkpoint complex (MCC) (42). Among them, *MAD1L1,* which codes for the MAD1 protein, was upregulated in *LOXL3*-knockout clones of the U87MG and U251 cell lines. The initial step in SAC signaling is the recruitment of MAD1-MAD2 complex to the unattached kinetochore (43). In this manner, SAC acts as a delay signal, prolonging mitosis until bipolar spindle attachment is achieved by all chromosomes. Mitotic entry is an irreversible and continuous process, and consequently cells cannot exit mitosis until SAC is satisfied. Cells treated with MT-disrupting agents presented a prolonged SAC and were arrested in mitosis for 24 h (44). *LOXL3*-knockout U87MG cells had and increased cell population in the G2/M phase in the first 12 h, and in the G1 phase after 36 h. In cases where chromosome biorientation is not resolved following prolonged mitotic arrest, cells can follow two pathways: apoptosis via caspase activation (45) or slippage, a process in which cells exit the M phase without chromosome segregation and enter the next cell cycle as single tetraploid cells (46). In cancer, cells that undergo slippage exit mitosis without cell division and return to interphase (G1), escaping mitotic cell death. Mitotic slippage has been proposed to limit the effectiveness of chemotherapy using MT-disrupting agents. (47). Similarly, to U87MG cells, knockout of *LOXL3* in U251 cell line increased the cell population in G2/M and the expression of *MAD1L1*, suggesting similar SAC activation. Among the DEGs that were downregulated in the *LOXL3*-knockout U251 cell line, there were genes that coded for centrosome proteins, such as *CEP72* and *CEP85*. The amplification of these genes is related to MT

acetylation (48). Additionally, there was a decrease in the cell population in the S phase, probably because the cells did not re-enter the cell cycle. The decision to enter a new cell cycle was attributed to E2F-RB regulation. During G1 phase, RB keeps E2F-dependent transcription inactive until S phase entry (44). In *LOXL3*-knockout U251 clone 1, there was increased expression of *RBL2* (which codes for p130), which is involved in E2F-dependent transcription. Accumulation of cyclins E and A results from E2F-dependent transcription and creates a decision window to enter the S phase (49). Cyclin E (coded by *CCNE1*) was downregulated in *LOXL3*-knockout U251 clones, suggesting an inhibition of S phase entry. In addition, the interaction between cyclin E and CDK2 is required for entry into the cell cycle. *INCA1*, a gene that codes for an inhibitor of CDK2 activity (50), was upregulated. *CDC7*, a component of DNA replicative helicase, was also downregulated, and its inhibition impaired progression through the S phase (51). Interestingly, we observed a substantial decrease in *RAD51C* and *RAD54B* in U251 knocked out to LOXL3. These genes code for proteins involved in the homologous recombination (HR) pathway of DNA repair, which maintains genomic stability (52, 53). *RAD51C* downregulation in cancer cells results in the accumulation of DNA damage (54), and *RAD54B* inhibition in hepatoma cells is associated with cell cycle arrest in the G1 phase (55). *BRCA1*, also downregulated in *LOXL3*-knockout U251 cells, when silenced in breast cancer cells, promoted a defective HR response and spindle damage (56). In addition, *ATM* expression is also downregulated. ATM is a sensor of DNA damage that phosphorylates BRCA1 and is associated with sensitivity to DNA-damaging chemotherapeutic agents (57).

SAC activation occurs during the metaphase-to-anaphase transition (58). MTs acetylation levels vary according to the mitosis phase. Acetylation occurs on spindle MTs

385 during metaphase and anaphase (59). Significant alterations in the amount and structure
386 of MT acetylation in *LOXL3*-knockout U87MG and U251 cells, mostly in clones 1, were
387 observed in metaphase and anaphase. This observation in *LOXL3*-knockout U251 clone
388 1 was accompanied by the detection of multipolar mitosis, associated with SAC
389 activation impairment or super-activation, and after p53-independent mitotic slippage
390 (60).

391 The evaluation of nuclei morphology and distribution revealed an increase in nuclear
392 aberrations characteristic of mitotic catastrophe in *LOXL3*-knockout U87MG cells,
393 whereas there was an increase in nuclei categorized as senescent cells in U251 cells
394 knocked down for *LOXL3*. Similar to our results, LOXL3 silencing resulted in aberrant
395 mitosis associated with mitotic catastrophe in melanoma cells (20). Additionally, *LOXL3*-
396 knockout U87MG cells showed an increase in cell death in the early phase, with a boost
397 after treatment with TMZ, compared to control cells. In contrast, there was a discrete
398 increase in cell death in the late phase in the *LOXL3*-knockout U251 cell line, without
399 alteration after TMZ treatment. Mitotic catastrophe is used to explain the mechanism of
400 delayed mitotic-linked cell death. Tetraploid cells can either be arrested at the G1 phase
401 and dye by p53-dependent apoptosis, or be arrested to an irreversible growth to
402 senescence. Senescent cells are generally characterized by a reduction in proliferative
403 capacity, adoption of flattened, enlarged cell shapes (similar to those observed by light
404 microscopy) and an increase in β-galactosidase activity (SA-β-gal) (61, 62). Interestingly,
405 similar effects have been observed with anti-MT drug therapy (46, 63).

406 Indeed, we observed an increase in gene expression related to cell death p53-dependent
407 in *LOXL3*-knockout U87MG cells. Interestingly, *HIPK2*, which code for homeodomain-

interacting protein kinase 2, was also upregulated. HIPK2 promotes cell death by activating p53 via phosphorylation in response to genotoxic stress. It is associated with reinforcement of the SAC-induced mitotic block, resulting in mitotic slippage and increased cyclin B levels, ultimately leading to cell death. This effect was observed under CDC14B downregulation conditions, which is consistent with the findings presented here (64). *DYRK2* is also upregulated in *LOXL3*-knockout U87MG cells and codes for a kinase that promotes p53 activation by phosphorylation in response to genotoxic stress (65). HIPK2 and DYRK2 activate p53 phosphorylation at Ser46, promoting the transcription of apoptosis-related genes. Phosphorylation of p53 at Ser20 occurs in response to DNA damage and is associated with increased *CDKN1A* expression (66), which may explain the decrease in *CDKN1A* expression in *LOXL3*-knockout U87MG cells. Additionally, we observed an increase in *APAF1* expression, which codes for a key molecule in the intrinsic apoptosis pathway and a transcriptional target of p53 (67). Furthermore, it was observed a downregulation of *MDM2*, an ubiquitin ligase, which is classically known to bind and promote p53 degradation (68). Therefore, our results suggest upregulation of p53, corroborating our findings of apoptosis when *LOLX3* was knocked out in U87MG cells, which have wild type *TP53*.

In contrast, U251 cells showed altered expression of senescence-related genes when *LOXL3* was knocked out. Cellular senescence can be induced in cells in the absence of p53 through a retinoblastoma (RB) tumor suppressor. RB controls cell cycle progression by repressing E2F activity. Although *RB1* expression was not altered, *E2F1/3* expression was downregulated (69). Furthermore, *CCNE1* and *CDC25A* expression levels were downregulated. *CCNE1* codes for cyclin E, which is a target of E2F-dependent transcription (70). *CDC25A*, in turn, which codes for a dual phosphatase, activates cyclin

E and CDK2 complex by phosphorylation, which in sequence phosphorylates and dissociates RB from complex with E2F, which is essential of the G1/S transition, corroborating with our findings, where *LOXL3*-knockout U251 cells presented a decrease in cell population in S phase (71). Downregulation of *CCNE1* is associated with cell cycle arrest in the G1 phase of gastric cancer cells (72). In addition, cyclin E/CDK2 promoted the degradation of p27 (coded by *CDKN1B*, which was upregulated). *CDKN1B* and *CDKN1A* act as inhibitors of cyclin-dependent kinases (CDKs) by binding and inhibiting cyclin E/CDK2, leading to G0/G1 cell cycle arrest and susceptibility to senescence (73). Notably, *CDKN1A*, a classic marker and inducer of senescence, was upregulated in *LOXL3*-knockout U251 cells with *TP53* mutation. p21 functions as a key downstream effector of the tumor suppressor p53. However, multiple studies have shown that p21 is activated by diverse p53-independent signals (74). Upregulation of p21 was observed in the U251 cell line, resulting in an increase of the cell population in the G2/M phase, with subsequent senescence, similar to that observed here (75).

Ultimately, MTs play a crucial role in cell migration by regulating cell polarity and extracellular matrix adhesion turnover. *LOXL3*-knockout promoted a decrease in cell adhesion only in U87MG cells, predominantly in clone 1. LOXL3 silencing by siRNA in the U87MG cell line resulted in increased cell adhesion (11), possibly as a result of a substantial increase in the expression of extracellular matrix-related genes, including other lysyl oxidases. No alterations in ECM-related genes were observed in the enrichment analysis. MT acetylation directly influences the increase in focal adhesion and cell migration of astrocytes (76), consistent with our results, which demonstrated a significant decrease in cell migration, particularly in clones 1 of both U87MG and U251 cells, which had the lowest expression of LOXL3. Our previous study showed that LOXL3

456 silencing promotes a decrease in cell invasion in U87MG (11). LOXL3 interacts with
457 SNAIL1 and plays a role in epithelial-mesenchymal transition in hepatocellular carcinoma
458 and adenocarcinoma (10, 77). We demonstrated a correlation between the expression
459 of *LOXL3* and the gene encoding the transcription factor β-catenin (*CTNNB1*), linked to
460 the SNAIL signaling pathway in low-grade astrocytoma (12).

461 *LOXL3* expression correlated with several analyzed genes in GBM RNA-seq datasets from
462 TCGA in mutTP53, wtTP53, and the total cohort. Genes exhibited a stronger correlation
463 with *LOXL3* in mutTP53 GBM cases. Subsequently, Kaplan-Meier analysis was performed
464 and demonstrated that downregulation of both *LOXL3* and *CCNE1* increased the survival
465 of patients with mutTP53. Previous survival analysis has already shown that lower
466 expression levels of *LOXL3* positively impacted the overall survival of GBM patients (11).
467 *CCNE1* amplification, found in a variety of malignancies associated with mutTP53,
468 contributes to a more aggressive clinical outcomes but with a better response to anti-
469 angiogenic therapy. Cyclin E overexpression due to *CCNE1* amplification and concurrent
470 mutTP53 promotes progression from the G1 phase to the S phase, providing evidence
471 that concurrent genetic alterations may help support future development of
472 personalized strategic therapies to enhance mitotic catastrophe and apoptosis (78).

473 Altogether, these results suggest that *LOXL3* silencing promotes MT destabilization
474 induced by a decrease of tubulin deacetylation followed by mitotic stress, or mitotic
475 catastrophe, SAC activation, and cell cycle arrest in G2/M and G1/S (79). Mitotic stress
476 promotes SAC activation in metaphase-anaphase phases, followed by an increase in cell
477 death in U87MG cells and senescence in U251 cells. The model depicting the effects of
478 *LOXL3* knockout on GBM U89MG and U251 cell lines is shown in Fig. 8.

GBM is a very heterogeneous tumor, the patients have poor outcomes. *TP53* mutations occur in up to 30% and 70% of primary and secondary GBM cases, respectively (80). Overall, these results suggest that *LOXL3* and *CCNE1* may be potential therapeutic targets for GBM cases harboring *TP53* mutation. Of note, *LOXL3* is also a potential therapeutic target in GBM patients with wtTP53, which can be induced by a programmed cell death by apoptosis.

Methods and materials

Cell culture

U87MG and U251 glioblastoma cells were obtained from American Type Culture Collection (Manassas, VA, USA). U251 cells line harbors mutation in *TP53*, whereas U87MG cells harbor wildtype *TP53* (80). Cells were grown in Dulbecco's modified Eagle's medium (DMEM) (Thermo Fisher Scientific, Waltham, MA, USA), complemented with 10% heat-inactivated fetal bovine serum (FBS) (Cultilab, Campinas, Brazil), and antibiotics (100 units/mL penicillin and 100 µg/mL streptomycin) in a humidified atmosphere with 5% CO2 at 37°C. The authentication of the cell line was conducted through short tandem repeat DNA analysis utilizing the GenePrint 10 System (Promega, Fitchburg, WI, USA). All the cell lines were routinely tested for mycoplasma.

LOXL3 knockout by CRISPR-Cas9

The knockout of LOXL3 was performed using the CRISPR (Clustered Regularly Interspaced Short Palindromic Repeats) system associated with an endonuclease (Cas9). The gene inactivation of LOXL3 was carried out in glioblastoma cell lines U87MG and U251. Two guide pairs (sgRNA) were designed for the coding sequence (CDS) region located in exon 2 of the LOXL3 gene (NM_032603.4), targeting the initiation codon region (sgRNA 1) and

the coding region (-95) (sgRNA 2). The sgRNA designs were generated using the online tool http://crispor.org (81) (Fig. S1a). For the silencing approach, the commercial vector pSpCas9(BB)-2A-Puro V2.0, also known as pX459 (Addgene, Cambridge, MA, USA) was used. Genome editing by CRISPR-Ca9 and cloning were performed according to a previously published procedure. U87MG and U251 cells were seeded in a six-well plate and transfected with 2µg of plasmids (empty vector as control, and the two cloned sgRNAs) and FuGENE according to the manufacturer's protocol (Promega). Single-cell clones were isolated by limiting dilution to obtain a homogenous cell population.

DNA and RNA extraction

DNA and RNA extractions were performed using the AllPrep DNA/RNA Mini kit (Qiagen, Valencia, CA, USA), following the protocol provided by the manufacturer. The concentrations and purity were determined by spectrophotometry at 260 and 280 nm. A260/A280 ratios greater than 1.8 were considered satisfactory for purity.

Sanger Sequencing

The CRISPR-Cas9 target region was amplified by PCR using 100 ng of DNA in GoTaq Green Master Mix buffer, containing 3 mM MgCl2 and 1U of GoTaq DNA polymerase (Promega), 10 µM primers, 2.5 µM dNTPs in a final volume of 25 µL. Agarose gel electrophoresis (2% in TAE buffer) was performed to confirm amplification. The primer sequences used are shown in Fig. S1a. The PCR products were subcloned into the pGEM-T Easy Vector (Promega), transformed into bacteria, and subjected to Sanger sequencing. Sanger sequencing was performed using PCR products from the selected cell clones and purified using Agencourt AMPure XP magnetic beads (Beckman Coulter Biosciences, Indianapolis, IN, USA). Sequencing was performed using an automated method on an

ABI 3500 Genetic Analyzer (Thermo Fisher Scientific) using BigDye Terminator v3.1 Cycle Sequencing Kit (Thermo Fisher Scientific). The sequences were compared to the original gene sequences published in GenBank.

Western blotting

Cell protein extracts were acquired through the radioimmunoprecipitation assay (Tris-HCl 454 50 mM, NP-40 1%, Na-deoxycholate 0.25%, NaCl 150 mM, EDTA 1 mM) lysis buffer and a protease inhibitor cocktail (Sigma–Aldrich, St. Louis, MO, USA). The total protein concentrations were assessed using the Bradford method. Cell lysates (20 µg of protein) were separated by 4–12% gradient polyacrylamide gel electrophoresis in NuPAGE 3-(N-morpholino) propanesulfonic acid electrophoresis buffer (Thermo Fisher Scientific) and transferred to a polyvinylidene difluoride membrane using the iBLOT system (Thermo Fisher Scientific). The membrane was incubated with rabbit polyclonal anti-LOXL3 (1:1,000, Aviva Antibody Corporation, San Diego, CA, USA), mouse monoclonal anti-acetylated tubulin (1:1,000, Sigma–Aldrich), mouse monoclonal anti-α-tubulin (1:8,000, Sigma–Aldrich), and mouse monoclonal anti-β-actin (1:20,000, Sigma–Aldrich) as a control for protein loading. Anti-rabbit and anti-mouse IgG secondary antibodies conjugated to peroxidase (1:1,000, Sigma–Aldrich) and the chemiluminescence detection system Clarity Western ECL Blotting Substrate (Bio-Rad Laboratories, Hercules, CA, USA) were used to visualize proteins in the membrane on the ImageQuant LAS4000 apparatus (GE Healthcare, Pittsburgh, PA, USA).

Viability assay

A total of 1×10^3 *LOXL3*-knockout clones and control of U87MG and U251 cells were seeded in 96-well plates. The cells were incubated with PrestoBlue Cell Viability Reagent

(Thermo Fisher Scientific) and viability was determined daily for four consecutive days. The fluorescence intensity (excitation at 540 nm; emission at 560 nm) was measured using a GloMax-96 Microplate Reader (Promega). The background consisted of DMEM with 10% fetal bovine serum was measured for each plate and was subtracted from each measurement value. Assays were performed in octuplicate in two independent experiments.

High-throughput sequencing for transcriptome analysis

RNA-seq libraries were performed using QuantSeq 3'mRNA-Seq Library Prep Kit-FWD for Illumina (Lexogen, Vienna, Austria) following the manufacturer's recommendations. Total RNA (500 ng) from each sample was used in quadruplicate to construct the libraries. The size distribution of each library was determined using TapeStation 4200 (Agilent Technologies) with a D1000 ScreenTape. DNA libraries were pooled and sequenced on a NextSeq 500 (Illumina, San Diego, CA) with a 75 bp single read in the SELA Facility Core of School of Medicine, University of Sao Paulo. Sequencing generated an average of 5 million reads per sample. Quality control analysis was performed using FASTQC software (82). Raw reads were aligned to hg38 using STAR software (83). Gene expression data was quantified using featureCounts software (84). Data normalization was conducted with edgeR software using the trimmed mean method. Expression levels were calculated as counts per million (CPM) (85). Differential expression analysis among groups and $\log_2$-CPM transformation of the data were performed using the limma framework (86). Differentially expressed genes (DEGs; genes differentially expressed in LOXL3 knockout clones compared with controls) were analyzed using DAVID (Database for Annotation, Visualization and Integrated Discovery; update 2021) and the Gene

Ontology (GO) - biological function database (87). Log_2-CPM values were transformed into z-scores for heatmap visualization. Data of Log_2-CPM of the samples from the differential expression analysis and enrichment analysis are presented in the Supplementary Material (S1 and S2, respectively).

Immunofluorescence

The cells were seeded in a monolayer on glass coverslips, fixed with 4% paraformaldehyde, permeabilized with 0.1% Triton X-100, and blocked with 4% goat serum. Subsequently, the cells were incubated with monoclonal anti-acetylated tubulin (1:200, Sigma–Aldrich) and anti-α-tubulin (1:2,000, Sigma–Aldrich) primary antibodies overnight at 37°C, followed by incubation with anti-mouse IgG secondary antibody conjugated to Alexa Fluor 488 and 568 (1:400; Thermo Fisher Scientific) overnight at 4°C. Nuclei were stained with 4',6-diamidino-2-phenylindole (DAPI; Thermo Fisher Scientific). The slides were analyzed under a confocal microscope Zeiss 510 LSM META and 780-NLO (Carl Zeiss Microscopy, Thornwood, NY, USA). The images were analyzed using the ImageJ software (National Institutes of Health, Bethesda, MD, USA).

Cell cycle analysis

Cells were seeded (5×10^3 cells/well) in six-well plates in triplicate with DMEM medium without FBS for synchronization. The next day, cells were incubated with DMEM containing FBS to induce cell cycle progression. Cells were collected for fixation with 70% ethanol at different time points (12, 24 and 36 h) and maintained at 4°C. Cells were treated with RNase A (30 µg/ml) (Sigma-Aldrich) to prevent the incorporation of DNA intercalators into RNAs, followed by incubation with PI. Cell detection and quantification

were performed using flow cytometry (FACS Canto II; BD Biosciences). The flow cytometry results were analyzed using FlowJo V10 software.

Nuclear morphology analysis

Nuclear morphology analysis was performed using a plugin in of Image J Fiji Software, based on nuclear irregularity index, characterized by the feature aspect, area box, radius ratio and roundness were combined in an index. These parameters were analyzed using principal component analysis (PCA). The nuclear population was divided into four categories: normal, large, irregular and small, and subdivided into regular and irregular. Putative biological meanings were assigned to each category. The protocol was performed according a previously procedure published (88). For this analysis, we used the prepared cells with stained nuclei for immunofluorescence, as described above.

Cell death analysis

LOXL3-knockout cells (5×10^3 cells/well) were seeded in six-well plates in quadruplicate and two independent experiments. Cells were treated with TMZ (0.5 mM) or without TMZ (control DMSO). Cells were labelled on the fourth day with FITC Annexin V and PI using the Dead Cell Apoptosis kit (Thermo Fisher Scientific). A total of 30,000 events were recorded for each condition. Detection and quantification of apoptotic cells (*LOXL3*-knockout and control) were performed by flow cytometry (FACS Canto II; BD Biosciences, San Jose, CA, USA). The flow cytometry results were analyzed using FlowJo V10 software. Three independent experiments were performed, including duplicate measurements.

Cell adhesion analysis

Cells (5×10^3 cells/well) were cultivated in six-well plates with DMEM complemented with 1% FBS and incubated for 2 h. Cells (5×10^4 cells/well) were seeded in 96-well plates and maintained for 3 hours at 37°C in an atmosphere with 5% CO2. After three washes with phosphate-buffered saline, the cells were incubated with the PrestoBlue Cell Viability Reagent (Thermo Fisher Scientific). The quantification of attached cells was performed by measuring the fluorescence intensity at 525 nm (excitation at 560 nm) using a GloMax-96 Microplate Reader (Promega) (89). Assays were performed in octuplicate in two independent experiments.

Cell migration analysis

To access cell migration, a wound-healing assay was performed. Cells (8×10^4 cells/well) were seeded in 48-well plates until they reached 70%-80% confluence. After removing the culture medium, a cell-free area was created in the monolayer with a thin pipette tip. The wells were washed, and DMEM with 1% FBS was added. The protocol was performed according to previously procedure published (90). The scratches were recorded at different time points (zero, 6, 18, and 24 h). Assays were performed in octuplicate in two independent experiments.

***In silico* GBM RNA-Seq data analyses**

The gene expression data for GBM from the RNA-seq dataset of The Cancer Genome Atlas (TCGA) were retrieved from the Genomics Data Commons Data Portal (https://portal.gdc.cancer.gov/) and subsequently normalized using the DESeq R software. Normalized read counts were converted to z-scores for heatmap visualization. The analyzed GBM dataset of TCGA database comprised 160 cases, consisting of 106

TP53 wildtype and 54 *TP53* mutated cases, with additional molecular subtypes classified as 29 proneural, 38 classical and 48 mesenchymal.

Statistical analyses

For cell viability, quantification of tubulin expression, cell cycle assay, nuclear morphology analysis, apoptosis assay, cell adhesion and cell migration assay the two-way analysis of variance was used to compare multiple groups, followed by Tukey's post-hoc test. For gene expression, one-way analysis of variance (ANOVA) followed by Tukey's post-hoc test was used. Correlation analyses between gene expression values were performed using the non-parametric Spearman's-rho correlation test. Correlation values equal to or greater than -0.2 or 0.2 with greater p-value of ≤ 0.05 were considered statistically significant. A heatmap was generated using z-score values. Survival analysis was performed using Kaplan-Meier curve with Log-Rank Test. Gene expression levels were categorized as low or high based on the median values of the group. SPSS version 20.0 (IBM Corporation, Armonk, NY, USA) and GraphPad Prism 8 (GraphPad Software, San Diego, CA, USA) were used for the statistical analyses. Statistical significance was set at $p \leq 0.05$.

Supplementary Materials:

Author Contributions: TSL, SKNM, and SMO-S conceptualized the study. TSL and RSS performed the experiments, interpreted and analyzed of data. TSL and RCC performed the CRISPR-Cas9 gene knockout. SKNM and SMO-S supervised the study. AML analyzed the next-generation sequencing data. TSL and SMO-S wrote the original manuscript draft. All authors have revised the content and approved the final version of the manuscript.

Funding: This research was supported by Conselho Nacional de Pesquisa (CNPq), grant #140482/2020-2, #304541/2020-6, #317214/2021-7, Sao Paulo Research Foundation (FAPESP grants #2015/03614-5, #2016/05777-1, #2020/02988-9, #2021/01207-4), Fundação Faculdade de Medicina (FFM), and Faculdade de Medicina da USP (FMUSP).

Acknowledgments: The authors thank to SELA Facility Core of School of Medicine, University of Sao Paulo (Fapesp grant #2014/50137-5) for assistance with sequencing.

Conflicts of Interest: The authors declare that the research was conducted in the absence of any commercial or financial relationships that could be construed as a potential conflict of interest.

Ethics Statement:

Funding Statement:

References

1. Ostrom QT, Price M, Neff C, Cioffi G, Waite KA, Kruchko C, et al. CBTRUS Statistical Report: Primary Brain and Other Central Nervous System Tumors Diagnosed in the United States in 2016-2020. Neuro-oncology. 2023;25(Supplement_4).
2. Brennan CW, Verhaak RG, McKenna A, Campos B, Noushmehr H, Salama SR, et al. The somatic genomic landscape of glioblastoma. Cell. 2013;155(2):462-77.
3. Louis DN, Perry A, Wesseling P, Brat DJ, Cree IA, Figarella-Branger D, et al. The 2021 WHO Classification of Tumors of the Central Nervous System: a summary. Neuro-oncology. 2021;23(8):1231-51.
4. Verhaak RG, Hoadley KA, Purdom E, Wang V, Qi Y, Wilkerson MD, et al. An integrated genomic analysis identifies clinically relevant subtypes of glioblastoma characterized by abnormalities in PDGFRA, IDH1, EGFR and NF1. Cancer Cell. 2010;17(1):98-110.
5. Laurentino Td, S., Soares Rd, S., Marie SKN, Oba-Shinjo SM. LOXL3 Function Beyond Amino Oxidase and Role in Pathologies, Including Cancer. Int J Mol Sci. 2019;20(14):3587.
6. Barker HE, Cox TR, Erler JT. The rationale for targeting the LOX family in cancer. Nat Rev Cancer. 2012;12(8):540-52.
7. Mäki JM, Kivirikko KI. Cloning and characterization of a fourth human lysyl oxidase isoenzyme. Biochem J. 2001;355(Pt 2):381-7.
8. Ma L, Huang C, Wang XJ, Xin DE, Wang LS, Zou QLC, et al. Lysyl Oxidase 3 Is a Dual-Specificity Enzyme Involved in STAT3 Deacetylation and Deacetylimination Modulation. Molecular Cell. 2017;65(2):296-309.

9. Vázquez-Naharro A, Bustos-Tauler J, Floristán A, Yuste L, Oltra SS, Vinyals A, et al. Loxl3 Promotes Melanoma Progression and Dissemination Influencing Cell Plasticity and Survival. Cancers. 2022;14(5).
10. Li R, Shang R, Li S, Ren Y, Shen L, Yang L, et al. LOXL3-promoted hepatocellular carcinoma progression via promotion of Snail1/USP4-mediated epithelial-mesenchymal transition. Environmental toxicology. 2022;37(10).
11. Laurentino TS, Soares RDS, Lerario AM, Marie SKN, Oba-Shinjo SM. LOXL3 Silencing Affected Cell Adhesion and Invasion in U87MG Glioma Cells. International journal of molecular sciences. 2021;22(15).
12. Laurentino TS, Soares RDS, Marie SKN, Oba-Shinjo SM. Correlation of Matrisome-Associatted Gene Expressions with LOX Family Members in Astrocytomas Stratified by IDH Mutation Status. International journal of molecular sciences. 2022;23(17).
13. Zhan M, Ding Y, Huang S, Liu Y, Xiao J, Yu H, et al. Lysyl oxidase-like 3 restrains mitochondrial ferroptosis to promote liver cancer chemoresistance by stabilizing dihydroorotate dehydrogenase. Nature communications. 2023;14(1).
14. Carmona B, Marinho HS, Matos CL, Nolasco S, Soares H. Tubulin Post-Translational Modifications: The Elusive Roles of Acetylation. Biology. 2023;12(4).
15. Janke C, Magiera MM. The tubulin code and its role in controlling microtubule properties and functions. Nature reviews Molecular cell biology. 2020;21(6).
16. Eshun-Wilson L, Zhang R, Portran D, Nachury MV, Toso DB, Löhr T, et al. Effects of α-tubulin acetylation on microtubule structure and stability. Proceedings of the National Academy of Sciences of the United States of America. 2019;116(21).
17. Gudimchuk NB, McIntosh JR. Regulation of microtubule dynamics, mechanics and function through the growing tip. Nature reviews Molecular cell biology. 2021;22(12).
18. Tran AD, Marmo TP, Salam AA, Che S, Finkelstein E, Kabarriti R, et al. HDAC6 deacetylation of tubulin modulates dynamics of cellular adhesions. Journal of cell science. 2007;120(Pt 8).
19. Laurentino TS, Soares RDS, Marie SKN, Oba-Shinjo SM. LOXL3 Function Beyond Amino Oxidase and Role in Pathologies, Including Cancer. International journal of molecular sciences. 2019;20(14).
20. Santamaria PG, Floristan A, Fontanals-Cirera B, Vazquez-Naharro A, Santos V, Morales S, et al. Lysyl oxidase-like 3 is required for melanoma cell survival by maintaining genomic stability. Cell Death Differ. 2018;25(5):935-50.
21. Xu Z, Schaedel L, Portran D, Aguilar A, Gaillard J, Marinkovich MP, et al. Microtubules acquire resistance from mechanical breakage through intralumenal acetylation. Science (New York, NY). 2017;356(6335).
22. Kadavath H, Hofele RV, Biernat J, Kumar S, Tepper K, Urlaub H, et al. Tau stabilizes microtubules by binding at the interface between tubulin heterodimers. Proceedings of the National Academy of Sciences of the United States of America. 2015;112(24).
23. Nagai T, Ikeda M, Chiba S, Kanno S, Mizuno K. Furry promotes acetylation of microtubules in the mitotic spindle by inhibition of SIRT2 tubulin deacetylase. Journal of cell science. 2013;126(Pt 19).
24. Takemura R, Okabe S, Umeyama T, Kanai Y, Cowan NJ, Hirokawa N. Increased microtubule stability and alpha tubulin acetylation in cells transfected with microtubule-associated proteins MAP1B, MAP2 or tau. Journal of cell science. 1992;103 (Pt 4).
25. Saragoni L, Hernández P, Maccioni RB. Differential association of tau with subsets of microtubules containing posttranslationally-modified tubulin variants in neuroblastoma cells. Neurochemical research. 2000;25(1).
26. Murphy M, Hinman A, Levine AJ. Wild-type p53 negatively regulates the expression of a microtubule-associated protein. Genes & development. 1996;10(23).

741 27. Hu P, Zong B, Chen Q, Shao R, Chen M, Yang Y, et al. Microtubule-associated protein 4
742 promotes epithelial mesenchymal transition in hepatocellular cancer cells via regulating
743 GSK3β/β-catenin pathway. Heliyon. 2023;9(3).
744 28. Matsuo M, Shimodaira T, Kasama T, Hata Y, Echigo A, Okabe M, et al. Katanin p60
745 contributes to microtubule instability around the midbody and facilitates cytokinesis in rat
746 cells. PloS one. 2013;8(11).
747 29. Hanselmann S, Wolter P, Malkmus J, Gaubatz S. The microtubule-associated protein
748 PRC1 is a potential therapeutic target for lung cancer. Oncotarget. 2017;9(4).
749 30. Singharajkomron N, Yodsurang V, Seephan S, Kungsukool S, Petchjorm S,
750 Maneeganjanasing N, et al. Evaluating the Expression and Prognostic Value of Genes Encoding
751 Microtubule-Associated Proteins in Lung Cancer. International journal of molecular sciences.
752 2022;23(23).
753 31. Jazvinšćak Jembrek M, Slade N, Hof PR, Šimić G. The interactions of p53 with tau and
754 Aß as potential therapeutic targets for Alzheimer's disease. Progress in neurobiology. 2018;168.
755 32. Song Y, Brady ST. Post-translational modifications of tubulin: pathways to functional
756 diversity of microtubules. Trends in cell biology. 2015;25(3).
757 33. Bär J, Popp Y, Bucher M, Mikhaylova M. Direct and indirect effects of tubulin post-
758 translational modifications on microtubule stability: Insights and regulations. Biochimica et
759 biophysica acta Molecular cell research. 2022;1869(6).
760 34. Cho Y, Cavalli V. HDAC5 is a novel injury-regulated tubulin deacetylase controlling axon
761 regeneration. The EMBO journal. 2012;31(14).
762 35. Rasamizafy SF, Delsert C, Rabeharivelo G, Cau J, Morin N, van Dijk J. Mitotic Acetylation
763 of Microtubules Promotes Centrosomal PLK1 Recruitment and Is Required to Maintain Bipolar
764 Spindle Homeostasis. Cells. 2021;10(8).
765 36. Cho HP, Liu Y, Gomez M, Dunlap J, Tyers M, Wang Y. The dual-specificity phosphatase
766 CDC14B bundles and stabilizes microtubules. Molecular and cellular biology. 2005;25(11).
767 37. Chan AKY, Yao Y, Zhang Z, Shi Z, Chen L, Chung NYF, et al. Combination genetic signature
768 stratifies lower-grade gliomas better than histological grade. Oncotarget. 2015;6(25):20885-
769 901.
770 38. Fong KW, Leung JW, Li Y, Wang W, Feng L, Ma W, et al. MTR120/KIAA1383, a novel
771 microtubule-associated protein, promotes microtubule stability and ensures cytokinesis.
772 Journal of cell science. 2013;126(Pt 3).
773 39. Fang CT, Kuo HH, Pan TS, Yu FC, Yih LH. HSP70 regulates the function of mitotic
774 centrosomes. Cellular and molecular life sciences : CMLS. 2016;73(20).
775 40. Van de Mark D, Kong D, Loncarek J, Stearns T. MDM1 is a microtubule-binding protein
776 that negatively regulates centriole duplication. Molecular biology of the cell. 2015;26(21).
777 41. Musacchio A. The Molecular Biology of Spindle Assembly Checkpoint Signaling
778 Dynamics. Current biology : CB. 2015;25(20).
779 42. Liu ST, Zhang H. The mitotic checkpoint complex (MCC): looking back and forth after 15
780 years. AIMS molecular science. 2016;3(4).
781 43. Lara-Gonzalez P, Pines J, Desai A. Spindle assembly checkpoint activation and silencing
782 at kinetochores. Seminars in cell & developmental biology. 2021;117.
783 44. Matthews HK, Bertoli C, de Bruin RAM. Cell cycle control in cancer. Nature reviews
784 Molecular cell biology. 2022;23(1).
785 45. Vitale I, Manic G, Castedo M, Kroemer G. Caspase 2 in mitotic catastrophe: The
786 terminator of aneuploid and tetraploid cells. Molecular & cellular oncology. 2017;4(3).
787 46. Cheng B, Crasta K. Consequences of mitotic slippage for antimicrotubule drug therapy.
788 Endocrine-related cancer. 2017;24(9).
789 47. Balachandran RS, Kipreos ET. Addressing a weakness of anticancer therapy with mitosis
790 inhibitors: Mitotic slippage. Molecular & cellular oncology. 2017;4(2).
791 48. Monteiro P, Yeon B, Wallis SS, Godinho SA. Centrosome amplification fine tunes tubulin
792 acetylation to differentially control intracellular organization. The EMBO journal. 2023;42(16).

793 49. Johnson A, Skotheim JM. Start and the restriction point. Current opinion in cell biology.
794 2013;25(6).
795 50. Bäumer N, Tickenbrock L, Tschanter P, Lohmeyer L, Diederichs S, Bäumer S, et al.
796 Inhibitor of cyclin-dependent kinase (CDK) interacting with cyclin A1 (INCA1) regulates
797 proliferation and is repressed by oncogenic signaling. The Journal of biological chemistry.
798 2011;286(32).
799 51. Montagnoli A, Moll J, Colotta F. Targeting cell division cycle 7 kinase: a new approach
800 for cancer therapy. Clinical cancer research : an official journal of the American Association for
801 Cancer Research. 2010;16(18).
802 52. Somyajit K, Subramanya S, Nagaraju G. Distinct roles of FANCO/RAD51C protein in DNA
803 damage signaling and repair: implications for Fanconi anemia and breast cancer susceptibility.
804 The Journal of biological chemistry. 2012;287(5).
805 53. Yasuhara T, Suzuki T, Katsura M, Miyagawa K. Rad54B serves as a scaffold in the DNA
806 damage response that limits checkpoint strength. Nature communications. 2014;5.
807 54. Min A, Im SA, Yoon YK, Song SH, Nam HJ, Hur HS, et al. RAD51C-deficient cancer cells
808 are highly sensitive to the PARP inhibitor olaparib. Molecular cancer therapeutics. 2013;12(6).
809 55. Wang R, Li Y, Chen Y, Wang L, Wu Q, Guo Y, et al. Inhibition of RAD54B suppresses
810 proliferation and promotes apoptosis in hepatoma cells. Oncology reports. 2018;40(3).
811 56. Chabalier C, Lamare C, Racca C, Privat M, Valette A, Larminat F. BRCA1 downregulation
812 leads to premature inactivation of spindle checkpoint and confers paclitaxel resistance. Cell
813 cycle (Georgetown, Tex). 2006;5(9).
814 57. Balmus G, Pilger D, Coates J, Demir M, Sczaniecka-Clift M, Barros AC, et al. ATM
815 orchestrates the DNA-damage response to counter toxic non-homologous end-joining at
816 broken replication forks. Nature communications. 2019;10(1).
817 58. Lampert F, Westermann S. A blueprint for kinetochores - new insights into the
818 molecular mechanics of cell division. Nature reviews Molecular cell biology. 2011;12(7).
819 59. Tan HF, Tan SM. The focal adhesion protein kindlin-2 controls mitotic spindle assembly
820 by inhibiting histone deacetylase 6 and maintaining α-tubulin acetylation. The Journal of
821 biological chemistry. 2020;295(18).
822 60. Brito DA, Rieder CL. Mitotic checkpoint slippage in humans occurs via cyclin B
823 destruction in the presence of an active checkpoint. Current biology : CB. 2006;16(12).
824 61. Casenghi M, Mangiacasale R, Tuynder M, Caillet-Fauquet P, Elhajouji A, Lavia P, et al.
825 p53-independent apoptosis and p53-dependent block of DNA rereplication following mitotic
826 spindle inhibition in human cells. Experimental cell research. 1999;250(2).
827 62. Vakifahmetoglu H, Olsson M, Zhivotovsky B. Death through a tragedy: mitotic
828 catastrophe. Cell death and differentiation. 2008;15(7).
829 63. Marxer M, Ma HT, Man WY, Poon RY. p53 deficiency enhances mitotic arrest and
830 slippage induced by pharmacological inhibition of Aurora kinases. Oncogene. 2014;33(27).
831 64. Puca R, Nardinocchi L, Sacchi A, Rechavi G, Givol D, D'Orazi G. HIPK2 modulates p53
832 activity towards pro-apoptotic transcription. Molecular cancer. 2009;8.
833 65. Feng L, Hollstein M, Xu Y. Ser46 phosphorylation regulates p53-dependent apoptosis
834 and replicative senescence. Cell cycle (Georgetown, Tex). 2006;5(23).
835 66. Jabbur JR, Huang P, Zhang W. DNA damage-induced phosphorylation of p53 at serine
836 20 correlates with p21 and Mdm-2 induction in vivo. Oncogene. 2000;19(54).
837 67. Shakeri R, Kheirollahi A, Davoodi J. Apaf-1: Regulation and function in cell death.
838 Biochimie. 2017;135.
839 68. Nag S, Qin J, Srivenugopal KS, Wang M, Zhang R. The MDM2-p53 pathway revisited.
840 Journal of biomedical research. 2013;27(4).
841 69. Müller H, Bracken AP, Vernell R, Moroni MC, Christians F, Grassilli E, et al. E2Fs regulate
842 the expression of genes involved in differentiation, development, proliferation, and apoptosis.
843 Genes & development. 2001;15(3).

70. Caldon CE, Musgrove EA. Distinct and redundant functions of cyclin E1 and cyclin E2 in development and cancer. Cell division. 2010;5.
71. Shen T, Huang S. The role of Cdc25A in the regulation of cell proliferation and apoptosis. Anti-cancer agents in medicinal chemistry. 2012;12(6).
72. Zhang C, Zhu Q, Gu J, Chen S, Li Q, Ying L. Down-regulation of CCNE1 expression suppresses cell proliferation and sensitizes gastric carcinoma cells to Cisplatin. Bioscience reports. 2019;39(6).
73. McKay LK, White JP. The AMPK/p27Kip1 Pathway as a Novel Target to Promote Autophagy and Resilience in Aged Cells. Cells. 2021;10(6).
74. Abbas T, Dutta A. p21 in cancer: intricate networks and multiple activities. Nature reviews Cancer. 2009;9(6).
75. Saito A, Kamikawa Y, Ito T, Matsuhisa K, Kaneko M, Okamoto T, et al. p53-independent tumor suppression by cell-cycle arrest via CREB/ATF transcription factor OASIS. Cell reports. 2023;42(5).
76. Bance B, Seetharaman S, Leduc C, Boëda B, Etienne-Manneville S. Microtubule acetylation but not detyrosination promotes focal adhesion dynamics and astrocyte migration. Journal of cell science. 2019;132(7).
77. Peinado H, Del Carmen Iglesias-de la Cruz M, Olmeda D, Csiszar K, Fong KS, Vega S, et al. A molecular role for lysyl oxidase-like 2 enzyme in snail regulation and tumor progression. Embo j. 2005;24(19):3446-58.
78. Yao S, Meric-Bernstam F, Hong D, Janku F, Naing A, Piha-Paul SA, et al. Clinical characteristics and outcomes of phase I cancer patients with CCNE1 amplification: MD Anderson experiences. Scientific reports. 2022;12(1).
79. Sazonova EV, Petrichuk SV, Kopeina GS, Zhivotovsky B. A link between mitotic defects and mitotic catastrophe: detection and cell fate. Biology direct. 2021;16(1).
80. Lee YJ, Seo HW, Baek JH, Lim SH, Hwang SG, Kim EH. Gene expression profiling of glioblastoma cell lines depending on TP53 status after tumor-treating fields (TTFields) treatment. Scientific reports. 2020;10(1).
81. Concordet JP, Haeussler M. CRISPOR: intuitive guide selection for CRISPR/Cas9 genome editing experiments and screens. Nucleic Acids Res. 2018;46(W1):W242-w5.
82. Spinozzi G, Tini V, Adorni A, Falini B, Martelli MP. ARPIR: automatic RNA-Seq pipelines with interactive report. BMC Bioinformatics. 2020;21(19):1-14.
83. Dobin A, Davis CA, Schlesinger F, Drenkow J, Zaleski C, Jha S, et al. STAR: ultrafast universal RNA-seq aligner. Bioinformatics. 2013;29(1):15-21.
84. Li B, Dewey CN. RSEM: accurate transcript quantification from RNA-Seq data with or without a reference genome. BMC Bioinformatics. 2011;12:323.
85. Wagner GP, Kin K, Lynch VJ. Measurement of mRNA abundance using RNA-seq data: RPKM measure is inconsistent among samples. Theory Biosci. 2012;131(4):281-5.
86. Ritchie ME, Phipson B, Wu D, Hu Y, Law CW, Shi W, et al. limma powers differential expression analyses for RNA-sequencing and microarray studies. Nucleic Acids Res. 2015;43(7):e47.
87. Sherman BT, Hao M, Qiu J, Jiao X, Baseler MW, Lane HC, et al. DAVID: a web server for functional enrichment analysis and functional annotation of gene lists (2021 update). Nucleic acids research. 2022;50(W1).
88. Filippi-Chiela EC, Oliveira MM, Jurkovski B, Callegari-Jacques SM, da Silva VD, Lenz G. Nuclear morphometric analysis (NMA): screening of senescence, apoptosis and nuclear irregularities. PloS one. 2012;7(8).
89. Humphries MJ. Cell-substrate adhesion assays. Current protocols in cell biology. 2001;Chapter 9.
90. Cory G. Scratch-wound assay. Methods in molecular biology (Clifton, NJ). 2011;769.

Graphical abstract – Effect of *LOXL3*-knockout by CRISPR-Cas9 in U87MG and U251 cell lines. Acetylation is a post-translational modification of tubulin that contributes to the stability of microtubules. α-TAT1, an α-tubulin acetyltransferase, coded by *ATAT1*, is the major enzyme that promotes tubulin acetylation. Microtubule acetylation affects directly binds to microtubule associated proteins (MAPs), such as Tau (coded by *MAPT*) and Fry (coded by *FRY*). Microtubule acetylation and the interactions with MAPs are required for essential cellular processes, such as adhesion, migration, and mitosis. Based on the data from the most effective *LOXL3* knockout (clone 1 for both U87MG and U251 cells), there was a decrease of tubulin acetylation levels in both cell lines, with greater significance in U87MG cell line. *MAPT* and *FRY* were downregulated in U87MG cells, but upregulated in U251 cells. Consequently, the effects of *LOXL3* knockout were distinct in both cell lines: 1) Decrease in cell adhesion (only for U87MG cells) and cell migration (for both cell lines). 2) Mitotic stress followed by cell cycle arrest (in both cell lines). 3) Activation of the spindle assembly checkpoint (SAC), characterized by mitotic arrest in metaphase/anaphase and increased expression of MAD1 in both cell lines (coded by *MAD1L1*), a component of the mitotic checkpoint complex. SAC is a crucial mechanism that ensures accurate chromosomal segregation and delays the next phase of the cell cycle. Prolonged SAC activation leads to cell cycle arrest and consequently, mitotic slippage, which may ultimately lead to two cell fates: p53-dependent cell death by apoptosis in U87MG cells and cell death by senescence in U251 cells, which has mutated and non-functional p53. 4) A delay in cell cycle progression in U87MG cells, with an increase in cell population in different phases of the cell cycle, while no upregulation of genes coding for caspases was observed. In U87MG, which has no mutation in *TP53*, there was an increase in the expression of *HIPK2* and *DYRK2,* genes related to p53-dependent cell death. Moreover, *APAF1* and *GADD45B,* transcriptional targets of p53 involved in cell death induced by DNA damage, were upregulated, while *MDM2*, a p53 inhibitor, was also downregulated. 5) Increased expression of *CDKN1A* and *CDKN1B*, considered senescence markers, in U251 cells. In addition, *CCNE1* was downregulated and *RBL2* was upregulated*,* followed by downregulation of *E2F2/3*. U251 cells have mutated *TP53* and, therefore, DNA damage caused by slippage causes senescence. Colors of the gene (italic) and protein names represent expression observed in transcriptome analysis. +, intensity of microtubule instability; stars represent negative (blue) or positive (red) Spearman's R correlation with *LOXL3*. Arrows indicate an increase (up, red) and decrease (down, blue) in cellular processes found in the functional assays.

Figure 1 – *LOXL3*-knockout of U87MG and U251 cell lines using CRISPR-Cas9. (a) *LOXL3* silencing approach using the CRISPR-Cas9 system with two different single guides RNA (sgRNAs). **(b)** Western blot analysis of *LOXL3* expression in control empty vector (EV) cells and after knockout and cloning (clone 1 and clone 2). β-actin was used as loading control of protein. LOXL3: 83kDa; β-actin: 42kDa. (c) Quantification of LOXL3 expression relative to β-actin and control EV in U87MG and U251 cell lines. The data are shown as percentages relative to the control. Bars represent the mean and standard deviation of two independent experiments. **(d)** Representative photomicrographs of morphology of control EV cells and *LOXL3* knockout clones. **(e-f)** Cell viability of control cells (empty vector) and *LOXL3*-knockout clones in U87MG and U251 cell lines, respectively. Data are represented as mean ± standard deviation (two independent experiments each

performed in octuplicate). Symbols represent significative p values compared to control; ## p≤0.001 ### p≤0.001, **** or #### p≤0.0001. (Two –way Anova with Tukey's multiple comparison post-hoc test). (g-j) RNA-seq analysis of *LOXL3* knockout U87MG and U251 cells relative to control cells. Top five gene ontology pathway enrichment analyses for **(g-h)** downregulated (i-j) and upregulated genes after *LOXL3* knockout in U87MG and U251 cell lines, respectively.

Figure 2 – Effect of *LOXL3* knockout on tubulin acetylation in U87MG and U251 cell lines. (a) Representative Western blot analysis of expression of total and acetylated α-tubulin in control cells (EV) and *LOXL3*-knockout clones 1 and 2 of both cells. β-actin was used as loading control. **(b)** Quantification of tubulin expression intensity relative to the control (EV) in U87MG and U251 cell lines. β-actin and tubulin were used as control. Data are represented as the ratio between acetylated and total tubulin normalized to the β-actin level. Quantification was performed using ImageJ *software*. Asterisks represent adjusted *p*-values: * p≤0.05, ** p≤0.001 (Two-way Anova with Tukey's multiple comparison post-hoc test). Bars represent the means and standard deviations of two independent analyses. **(c)** Immunofluorescence for acetylated tubulin (red) and nucleus (DAPI, blue) in control EV and LOXL3 knockout clones of U87MG and U251 cells. Magnification: 63x oil objective and 5x zoom out. EV, empty vector; CL1, clone 1; CL2, clone 2; Ac-α-Tub, acetylated α-tubulin; α-Tub, α- tubulin. **(d)** Gene expression of microtubule-associated proteins in LOXL3-knockout and control U87MG and U251 by RNA-seq analysis. Asterisks represent adjusted *p* values: * p≤0.05, ** p≤0.001, ***p≤0.0001, **** p≤0.001, ****p<0.001. (One-way Anova with Tukey's multiple comparison post-test). The bars represent the mean and standard deviation of four replicates.

Figure 3 – Effect of *LOXL3* knockout on cell cycle progression in U87MG and U251 cell lines. (a–b) Percentage of the cell population in each phase of the cell cycle after 12, 24, and 36 h of synchronization in U87 and U251 cell lines, respectively. Each color represents the phases of cell cycle. Analyses were performed using flow cytometry (30,000 events/sample) and PI staining. Each bar represents the mean ± standard deviation of triplicate experiments. Asterisks represent adjusted *p*-value; * p≤0.05, ** p≤0.01, **** p≤0.0001 (Two -way Anova with Tukey's multiple comparison post-hoc test). **(c-d)** Representative histograms showing the phases of the cell cycle of control and clones 1 and 2 knocked out for *LOXL3* in U87MG and U251 cell lines, respectively. **(e-f)** Heatmap of downregulated genes of the cell cycle in clones with *LOXL3* knocked down relative to control EV in U87MG and U251 cell lines, respectively. The heatmap shows the z-scores of the normalized read counts. Read count data were normalized to z-scores. **(g-h)** Bars show the fold change in the expression of upregulated genes of the cell cycle in U87MG and U251 clones, respectively, relative to the control. Asterisks represent p value of fold change analysis of clones relative to control: * p≤0.05, *** p≤0.001, **** p≤0.0001. EV, empty vector; CL1, clone 1; CL2, clone 2; SAC, spindle assembly checkpoint; PI, propidium iodide.

Figure 4. Effect of LOXL3 knockout on mitotic phases in U87MG and U251 cell lines. Immunofluorescence for acetylated tubulin (red) and nuclei (DAPI) in control (EV) and LOXL3 knocked out clones in the metaphase and anaphase phases of mitosis. EV, empty vector; CL1, clone 1; CL2, clone 2; Ac-Tub, acetylated tubulin.

Figure 5 – Nuclear morphometric analysis and cell death analysis after *LOXL3* knockout in U87MG and U251 cell lines. (a-b) Distribution of nuclei according to nuclear morphometric analysis (NMA) performed using the area and nuclear irregularity index (NII) in control EV and *LOXL3-knockout* clones of U87MG and U251, respectively. Each point represents a single nucleus. Empty vector (n=64, n=108), clone 1 (n=198, n=233), and clone 2 (n=105, n=230) for U87MG and U251 cells, respectively. These analyses were performed using the NII plugin in ImageJ software. Graphs show the mean and standard deviation of the percentages of different NMA populations: Normal (N), Irregular (I), Small and Regular (SR), Small (S), Small and Irregular (SI), and Large and Regular (LR), Large and Irregular (LI). Arrows indicate nuclei altered, and asterisk indicate micronuclei. Bars represents mean ± standard deviations of the number of nuclei amount by population, two independent experiment **(c-d)** Analyses of apoptotic process in control EV and *LOXL3*-knockout clones in U87MG and U251 cell lines, respectively. Each bar represents the percentage of cell population in the early and late phases of cell death, with or without TMZ treatment. Analyses were performed by flow cytometry (30,000 events/sample) using PI and annexin V staining. Bars represent the mean ± standard deviation of two independent experiments performed in quadruplicate. Asterisks represent *p* values: * $p \leq 0.05$, ** $p \leq 0.001$, *** $p \leq 0.0002$, **** $p < 0.0001$ (Two-way Anova with Tukey's multiple comparison post-hoc test). **(e-f)** Representative scatter plot of the cell death analysis. Red, late cell death; blue, live cells; green, early cell death. **(g)** Dot plot of gene expression related to cell death and senescence in LOXL3-silenced clones. Size dot as log10 (p value), color as expression fold change of clones relative to the control. EV, empty vector; CL1, clone 1; CL2, clone 2; PI, propidium iodide; TMZ, temozolomide; FC, fold change.

Figure 6 – Effect of LOXL3 knockout on cell adhesion and migration in U87MG and U251 cell lines. (a-b) Cell adhesion analysis of control and *LOXL3*-knockout clones in U87MG and U251, respectively. Bars represent the mean and standard deviation of two independent experiments in octuplicate. Asterisks represent adjusted *p*-values of Two-way Anova with Tukey's multiple comparison post-test: * $p \leq 0.05$, ** $p \leq 0.001$, **** $p \leq 0.0001$. **(c-d)** Cell migration analysis performed using wound healing assay. Bars represent the percentage of cell migration to the scratch area after 6h, 18h and 24h in relation to time point zero in control and *LOXL3*-knockout clones in U87MG (c) and U251 (d) cell lines. The bars represent the mean and standard deviation of two independent experiment in octuplicate. Asterisks represent adjusted *p* -values of Two-way Anova with Tukey's multiple comparison post-test: * $p \leq 0.05$, ** $p \leq 0.001$, **** $p \leq 0.0001$. **(e)** Representative photomicrographs (10x) of the cell migration assay. The blue lines represent the scratch-area limits. Asterisks represent adjusted *p*-value of Two-way Anova with Tukey's multiple comparison post-test: * $p \leq 0.05$, ** $p \leq 0.001$, **** $p \leq 0.0001$.

Figure 7 - Differential gene expression analysis of enrichment pathways in TCGA glioblastoma database. (a) Dot plot of correlation analysis of differentially expressed genes related to the cell cycle, mitosis, and microtubules showing correlation with *LOXL3*. Each dot represents a gene, with color indicating Spearman's R correlation and dot size representing the *p*-value ($p=0.05 < \text{dot size} > p<0.05$). Correlation was performed within different groups (columns), including the total (dark blue), wildtype *TP53* (dark green), and mutated *TP53* samples (light gray). The genes were categorized into groups based on their associated pathways. **(b)** Heatmap of the expression of genes that

correlated with *LOXL3* expression in different subtypes (G-CIMP, proneural, classical and mesenchymal subtypes) and TP53 mutation status (columns). Selected genes are depicted in the heatmap of the z-score of the normalized read counts. **(c)** Overall survival rate using Kaplan-Meier analysis in GBM cases with mutated *TP53*, stratified by high and low *LOXL3* and *CCNE1* expression (according to the median). *p* values were calculated using log-rank test. **(d)** Table shows data from TCGA database for univariate analysis. Multivariate analysis did not reveal significant differences between the individual variables (*LOXL3* and *CCNE1*), indicating that the impact on survival is dependent on their coexpression.

Supplementary Table 1. Data of logCPM of gene expression up and down regulation of cells control and LOXL3-knockout cells in U87MG and U251

Supplementary Table 2. Table with detailed data of the TOP 5 gene ontology terms of biological processes

Supplementary figure 1a. Sequences of RNA guides and primers used to LOXL3 knockout by CRISPR-cas9

Supplementary figure 1b. Details of mutation generated in LOXL3 gene in LOXL3-knockout clones 1 and 2 by CRISPR-Cas9 in U87MG and U251.

Figura 1

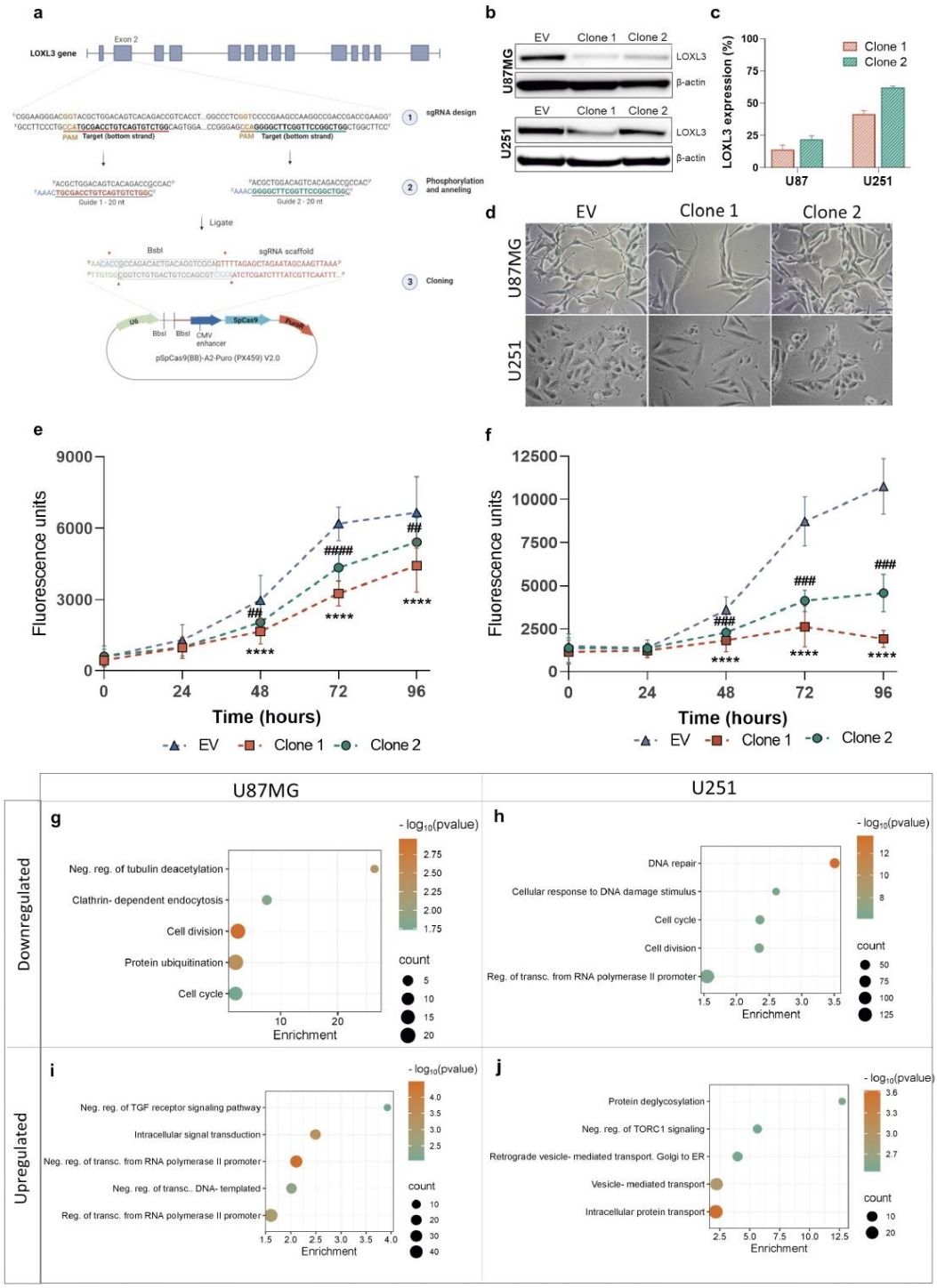
a
LOXL3 gene
Exon 2
sgRNA design
Phosphorylation and anneling
Ligate
Cloning
BbsI
sgRNA scaffold
U6
CMV enhancer
SpCas9
pSpCas9(BB)-A2-Puro (PX459) V2.0
b
EV
Clone 1
Clone 2
U87MG
U251
LOXL3
β-actin
c
LOXL3 expression (%)
U87
U251
d
EV
Clone 1
Clone 2
U87MG
U251
e
Fluorescence units
Time (hours)
EV
Clone 1
Clone 2
f
Fluorescence units
Time (hours)
EV
Clone 1
Clone 2
U87MG
U251
Downregulated
Upregulated
g
Neg. reg. of tubulin deacetylation
Clathrin- dependent endocytosis
Cell division
Protein ubiquitination
Cell cycle
Enrichment
- log10(pvalue)
count
h
DNA repair
Cellular response to DNA damage stimulus
Cell cycle
Cell division
Reg. of transc. from RNA polymerase II promoter
Enrichment
- log10(pvalue)
count
i
Neg. reg. of TGF receptor signaling pathway
Intracellular signal transduction
Neg. reg. of transc. from RNA polymerase II promoter
Neg. reg. of transc.. DNA- templated
Reg. of transc. from RNA polymerase II promoter
Enrichment
- log10(pvalue)
count
j
Protein deglycosylation
Neg. reg. of TORC1 signaling
Retrograde vesicle- mediated transport. Golgi to ER
Vesicle- mediated transport
Intracellular protein transport
Enrichment
- log10(pvalue)
count

Figura 2

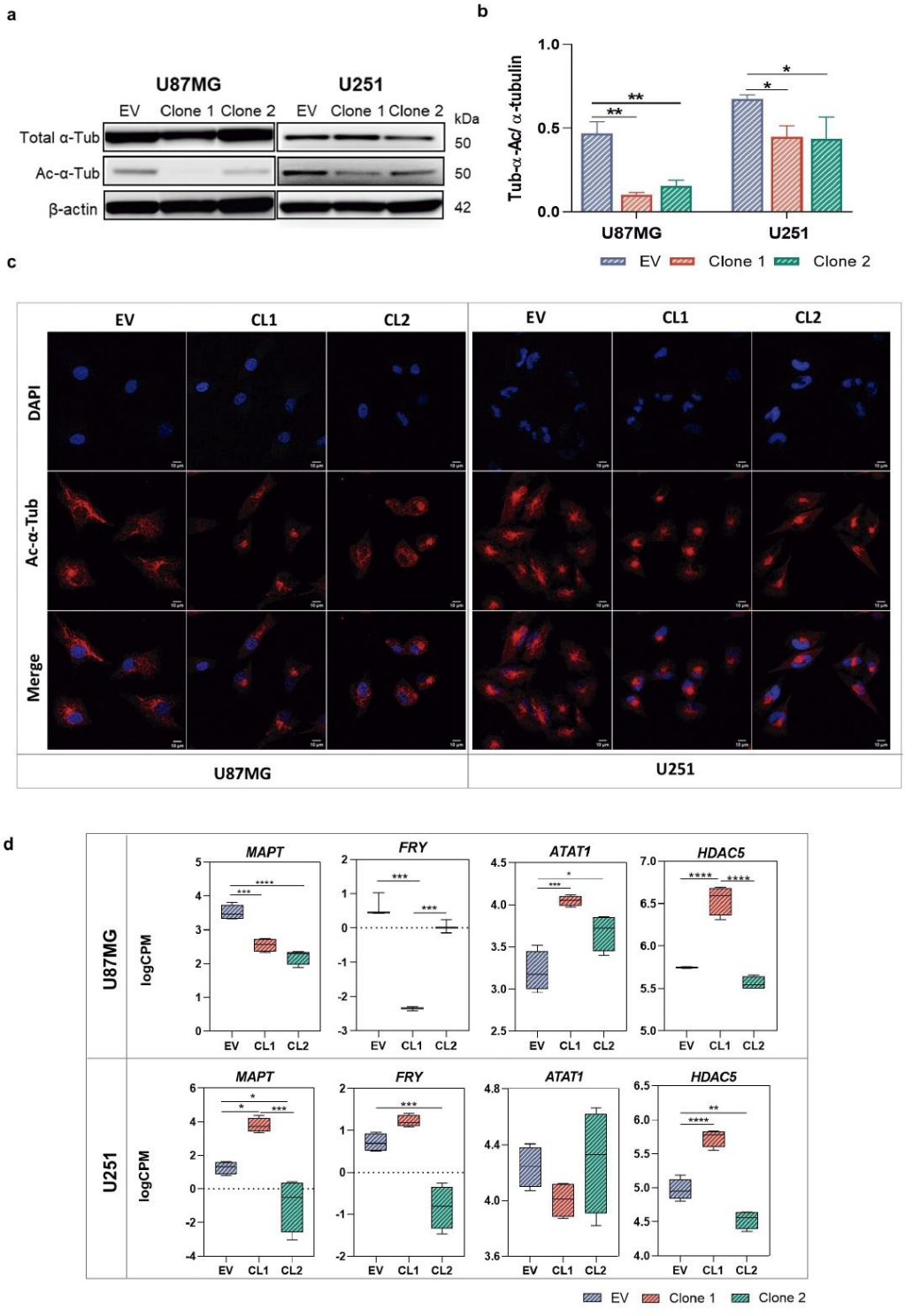
a
U87MG
U251
EV
Clone 1
Clone 2
kDa
Total α-Tub
Ac-α-Tub
β-actin
50
50
42
b
Tub-α-Ac/ α-tubulin
1.0
0.5
0.0
U87MG
U251
EV
Clone 1
Clone 2
c
EV
CL1
CL2
DAPI
Ac-α-Tub
Merge
U87MG
U251
d
U87MG
U251
logCPM
MAPT
FRY
ATAT1
HDAC5
EV
CL1
CL2
EV
Clone 1
Clone 2

Figura 3

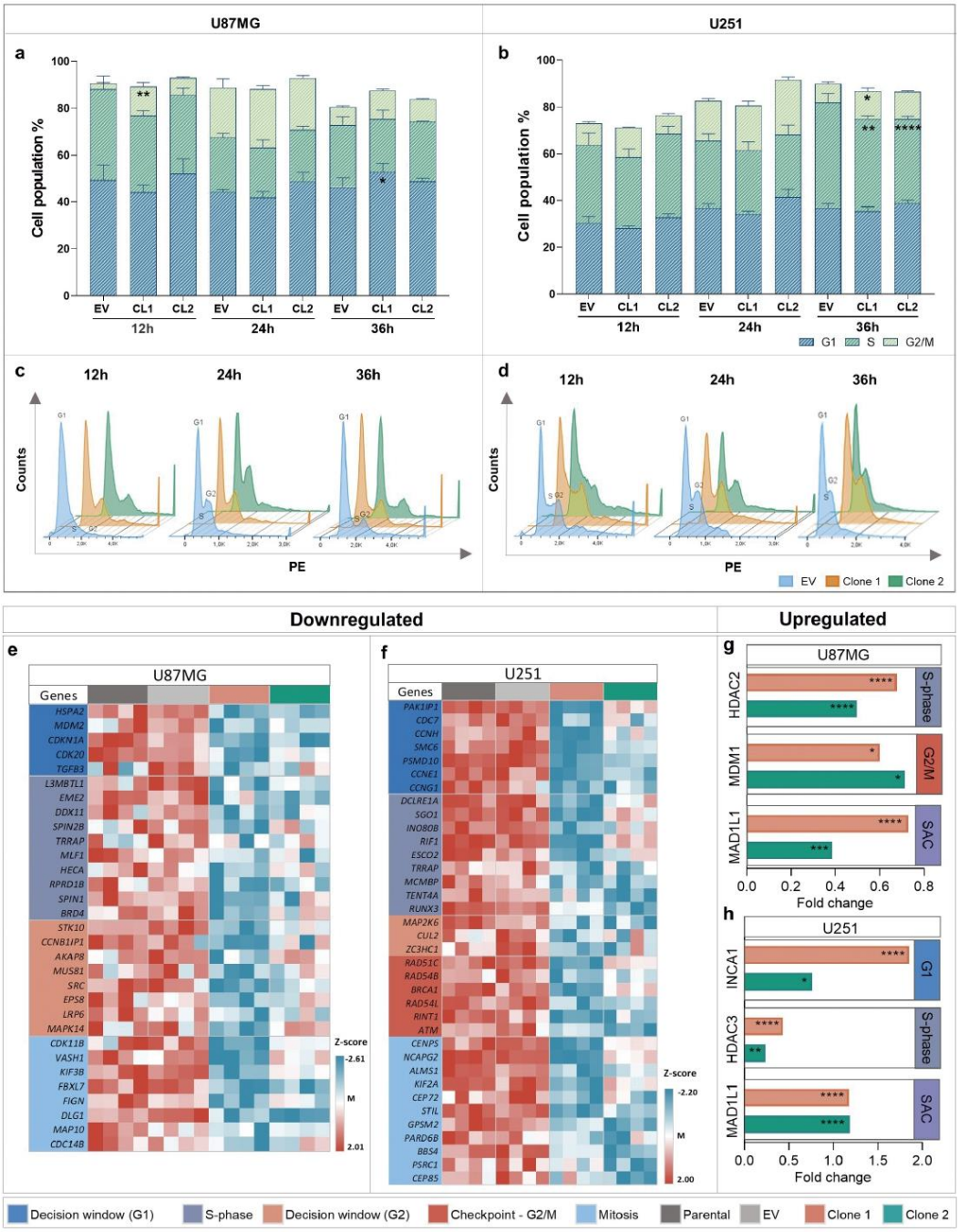
U87MG
U251
a
b
Cell population %
EV CL1 CL2 EV CL1 CL2 EV CL1 CL2
12h 24h 36h
G1 S G2/M
c
d
12h 24h 36h
Counts
PE
EV Clone 1 Clone 2
Downregulated
Upregulated
e
f
U87MG
U251
Genes
HSPA2 MDM2 CDKN1A CDK20 TGFB3 L3MBTL1 EME2 DDX11 SPIN2B TRRAP MLF1 HECA RPRD1B SPIN1 BRD4 STK10 CCNB1IP1 AKAP8 MUS81 SRC EPS8 LRP6 MAPK14 CDK11B VASH1 KIF3B FBXL7 FIGN DLG1 MAP10 CDC14B
PAK1IP1 CDC7 CCNH SMC6 PSMD10 CCNE1 CCNG1 DCLRE1A SGO1 INO80B RIF1 ESCO2 TRRAP MCMBP TENT4A RUNX3 MAP2K6 CUL2 ZC3HC1 RAD51C RAD54B BRCA1 RAD54L RINT1 ATM CENPS NCAPG2 ALMS1 KIF2A CEP72 STIL GPSM2 PARD6B BBS4 PSRC1 CEP85
Z-score
-2.61
M
2.01
-2.20
2.00
g
h
HDAC2 MDM1 MAD1L1
INCA1 HDAC3 MAD1L1
S-phase G2/M SAC
G1 S-phase SAC
Fold change
Decision window (G1) S-phase Decision window (G2) Checkpoint - G2/M Mitosis Parental EV Clone 1 Clone 2

Figura 4

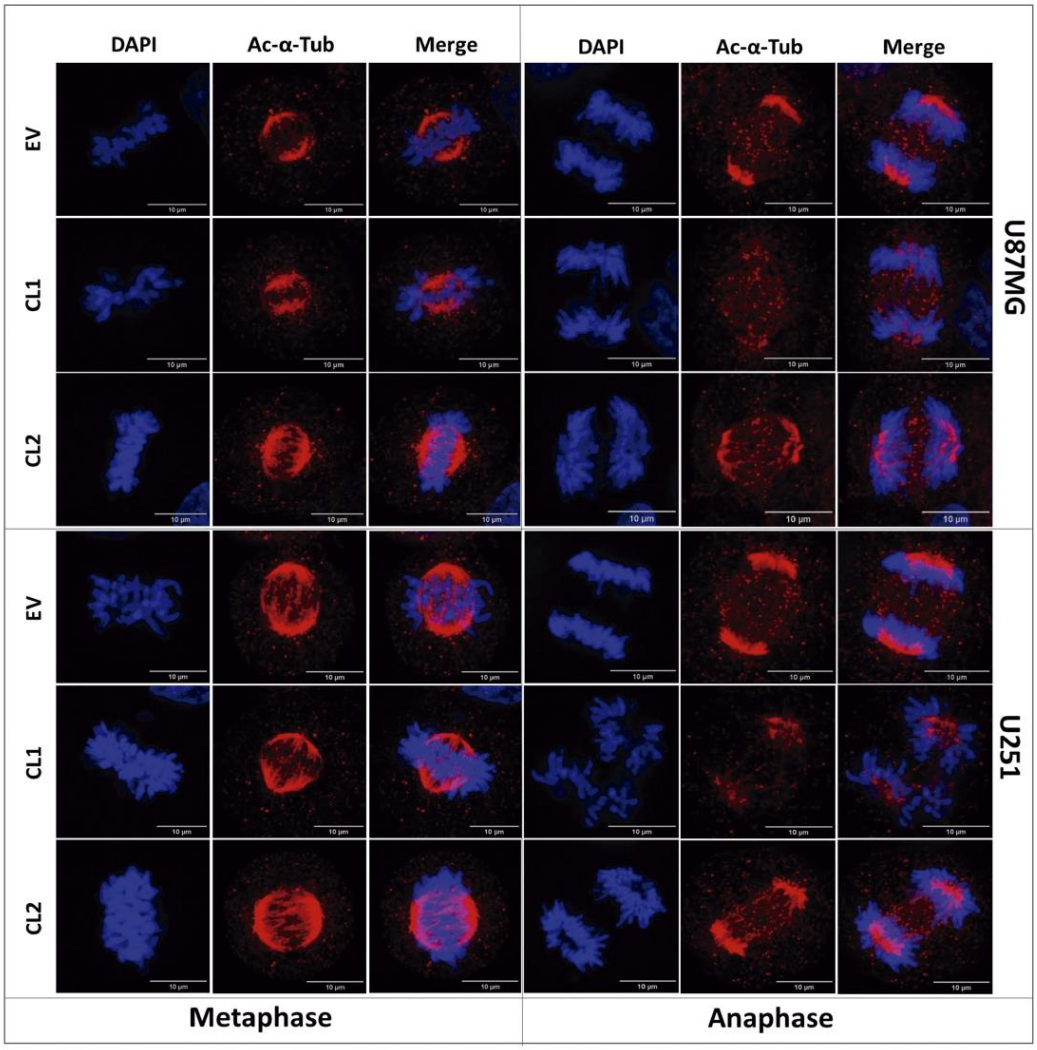
DAPI
Ac-α-Tub
Merge
DAPI
Ac-α-Tub
Merge
EV
CL1
CL2
U87MG
EV
CL1
CL2
U251
Metaphase
Anaphase

Figura 5

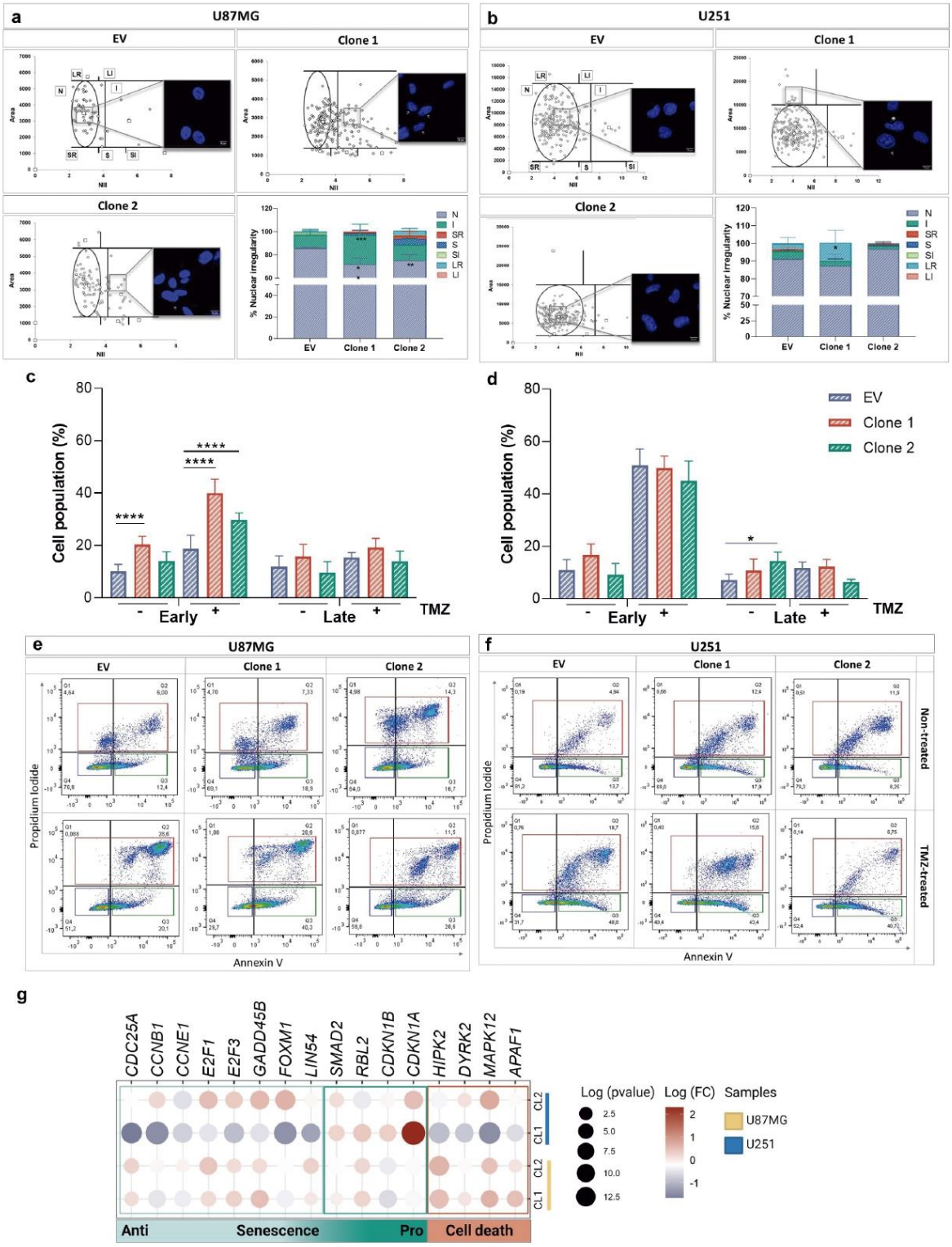
a
U87MG
EV
Clone 1
Clone 2
% Nuclear irregularity
b
U251
c
Cell population (%)
Early
Late
TMZ
d
EV
Clone 1
Clone 2
e
U87MG
f
U251
Propidium Iodide
Annexin V
Non-treated
TMZ-treated
g
CDC25A
CCNB1
CCNE1
E2F1
E2F3
GADD45B
FOXM1
LIN54
SMAD2
RBL2
CDKN1B
CDKN1A
HIPK2
DYRK2
MAPK12
APAF1
Anti
Senescence
Pro
Cell death
Log (pvalue)
Log (FC)
Samples
U87MG
U251

Figura 6

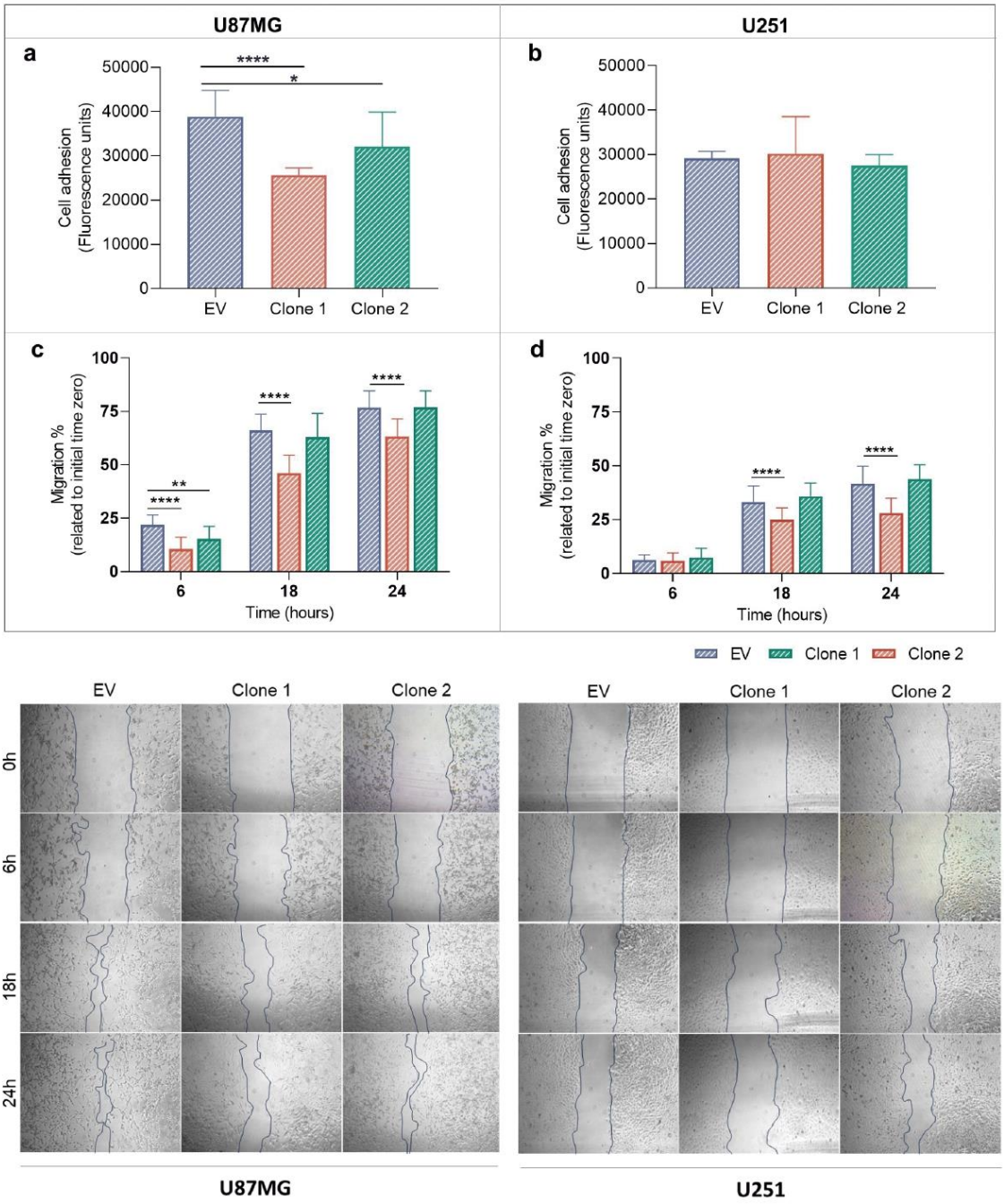
U87MG
U251
a
b
c
d
Cell adhesion (Fluorescence units)
50000
40000
30000
20000
10000
0
****
*
EV
Clone 1
Clone 2
Migration % (related to initial time zero)
100
75
50
25
0
**
****
6
18
24
Time (hours)
EV
Clone 1
Clone 2
0h
6h
18h
24h
U87MG
U251

Figura 7

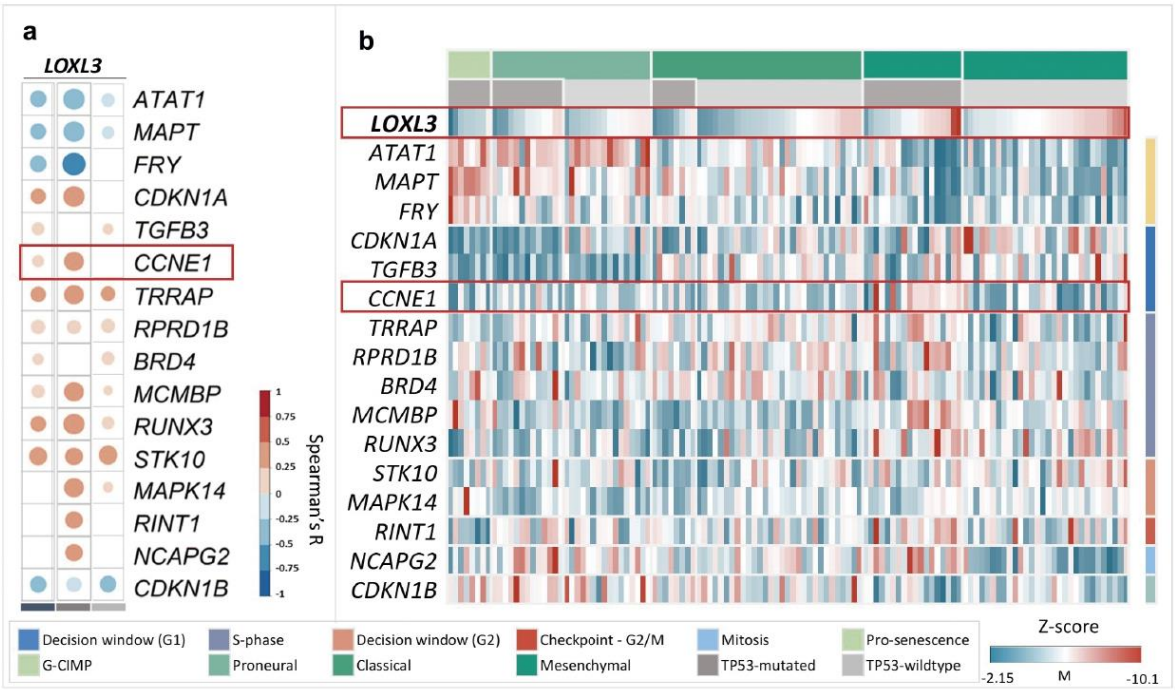

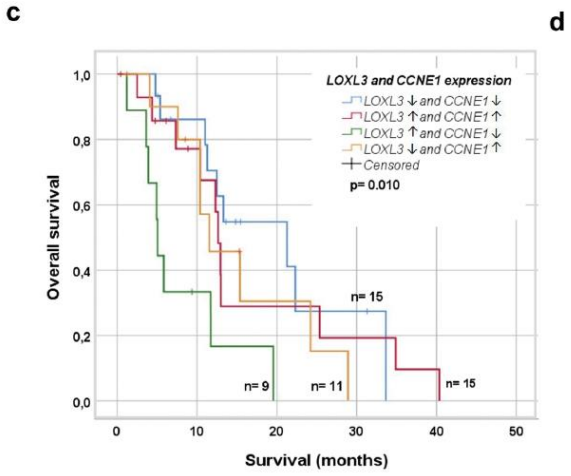

d

Univariate Analysis				
Caracteristic (TP53 mutated group)	**Patients (n)**	**95% CI**		***p* value**
Age < 59.0y >	<59: 22	12.3-23.3		0.33
	>59: 28	10.1-18.8		
Sex	Female: 20	2.4-8.2		0.15
	Male: 30	12.9-22.0		
LOXL3 exp.	Low: 26	13.5-22.1		0.229
	High 24	8.2-18.2		
CCNE1 exp.	Low: 24	10.4-19.8		0.687
	High: 26	11.5-21.1		
LOXL3/CCNE1 exp. (respectively)	↓↓:15	13.4-25.8		-
	↑↑: 15	9.5-23.9	Pairwise comparisons	↓↓ vs ↑↑: 0.676
	↑↓: 9	3.6-12.9		↓↓ vs ↑↓: **0.002**
	↓↑: 11	9.46-21.1		↓↓ vs ↓↑: 0.128

Resumo gráfico

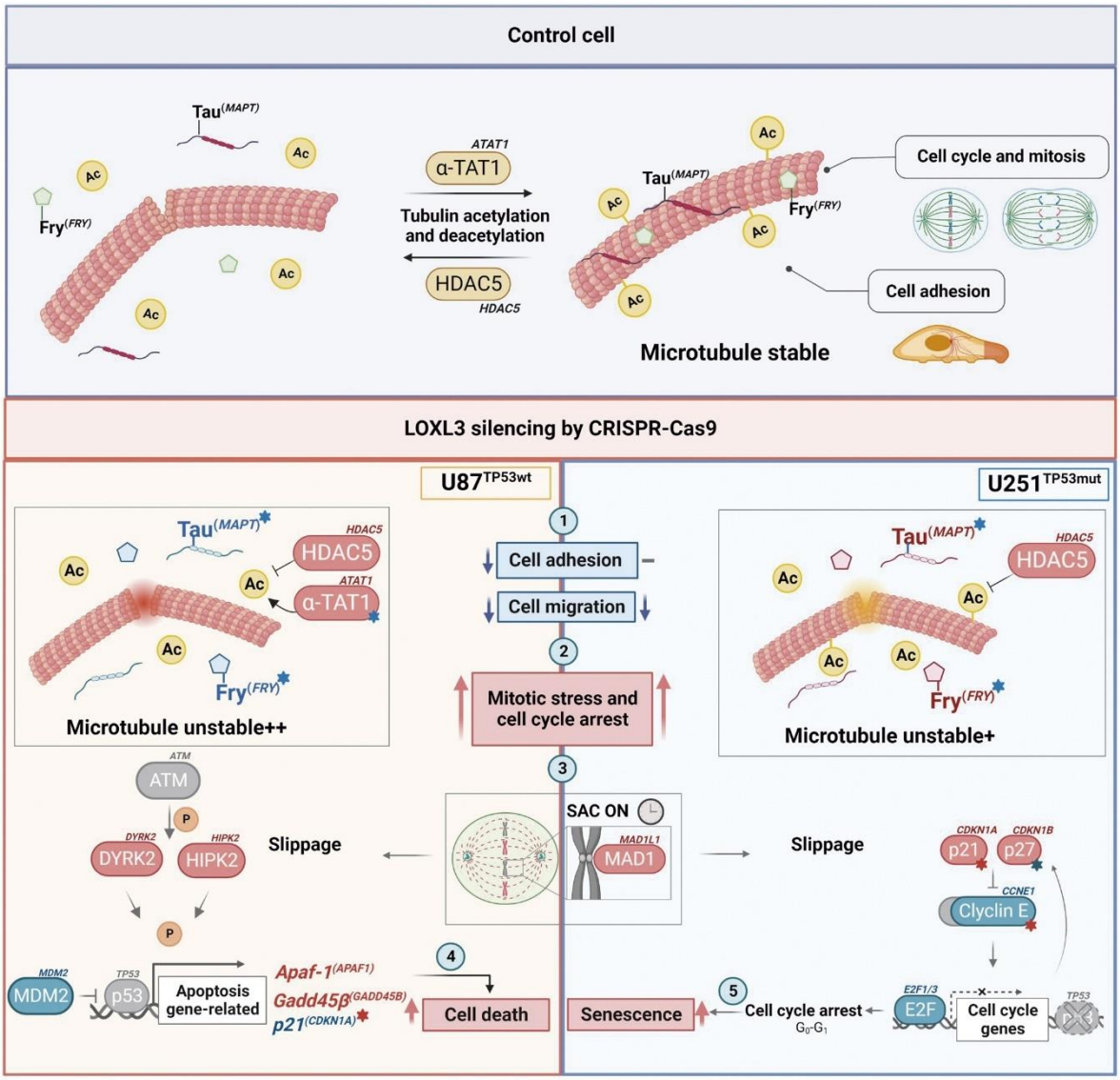

Figura suplementar 1 (Fig. S1)

S1.a

Design	Sequences	Score
sgRNA 1	F- CCAGACACTGACAGGTCGCA	88%
	R- TGCGACCTGTCAGTGTCTGG	
Primers - sgRNA1	F- GCCTGGATCATTGCTCACCT	
	R- ACACTTTGTCTCTGGGGCAC	
sgRNA 2	F -CCAGGGGCTTCGGTTCCGGC	88%
	R -GCCGGAACCGAAGCCCCTGG	
Primers – sgRNA2	F- GCCTGGATCATTGCTCACCT	
	R- CAGACACTGACAGGTCGCAT	
Primer pLKO.1	F – GACTATCATATGCTTACCGT	

S1.b

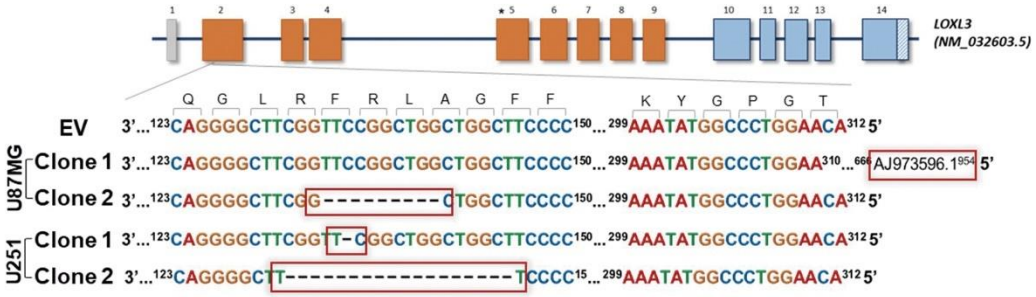

7 DISCUSSÃO

Os astrocitomas são tumores originados de células astrocíticas, e são divididos de acordo com seu grau de malignidade e características moleculares. O glioblastoma, é um dos tumores astrocítícos com pior prognóstico, e são os tumores malignos cerebrais e do SNC mais comuns (12). Estudos anteriores do nosso laboratório mostraram uma alta expressão do gene de lisil oxidase (*LOX)* em glioblastoma em comparação com astrocitoma pilocítico. LOXL3 é uma amino oxidase pertencente à família LOX, responsável pela ligação cruzada do colágeno e da elastina, resultando em rigidez e estabilidade da MEC. LOXL3 está intimamente associada à tumorigênese e à progressão tumoral em vários tipos de câncer. (11).

Neste estudo, investigamos a expressão dos membros da família lisil oxidase nos diferentes graus de astrocitomas, com estratificação molecular de IDH1, através de análises em banco de dados público, bem como especificamente, o papel funcional de LOXL3 em astrocitomas por meio de ensaios de silenciamento transitório e permanente.

Na publicação de número 1 do presente trabalho, foi demonstrado que *LOXL3* é altamente expresso em diversos tipos de tumores, inclusive em astrocitomas de diferentes graus de malignidade. Além disso, *LOXL3* apresentou maior expressão no subtipo molecular mesenquimal de GBM, que apresenta o pior prognóstico. Membros da família LOX tem sido correlacionados com a tumorigênese em diferentes tipos de neoplasias (37). LOXL3 tem sido descrito hiperexpresso em vários tumores, como gástrico, mama, ovários, carcinomas de colorretal (11). Além disso, a expressão de *LOXL3* influenciou no prognóstico dos pacientes com GBM. Análises de curva de Kaplan Meier de sobrevida demonstraram que níveis de expressão mais baixos de *LOXL3* impactam positivamente na sobrevida dos casos com GBM em relação aos que apresentaram maiores níveis de expressão do gene.

Com base nos dados anteriores, foi realizado o silenciamento transitório de LOXL3 afim de entender o papel funcional de LOXL3 em astrocitomas. A diminuição da expressão de *LOXL3* reduziu significantemente a viabilidade, além de promover o aumento da morte celular com e sem tratamento de TMZ em comparação com o controle. Estudos anteriores em outros tumores, também demonstraram resultados semelhantes. A redução da expressão de LOXL3 também resultou na diminuição da proliferação celular em melanoma (7, 30). O silenciamento de LOXL3 também promoveu um aumento da adesão celular, e uma diminuição da invasão celular em célula U87MG. Análises de transcriptoma das células silenciadas demonstraram processos relacionados a MEC e adesão regulados positivamente nas células silenciadas em relação ao controle, corroborando com resultados observados

através de ensaios funcionais. LOXL3 tem sido associado com progressão de tumor e metástase através da interação com SNAIL, um fator de transcrição envolvido na transição epitélio-mesênquima (29). Enquanto que as vias reguladas negativamente foram relacionadas a endossomos/vacúolos e proteínas de ligação a MAPK.

Análises de imunofluorescência, utilizando faloidina e tubulina como marcadores, evidenciaram alterações significativas na morfologia celular. Observou-se um aumento substancial da área nas células submetidas ao processo de silenciamento em comparação ao grupo controle. A linhagem celular T98G, considerada de menor agressividade em relação a U87MG (41), também foi submetida ao silenciamento gênico de *LOXL3*. Semelhantemente, uma alteração morfológica nas células silenciadas, corroborando com o efeito observado na linhagem celular U87MG, sugerindo que os dados observados do silenciamento de *LOXL3* não são célula-específica. Microtúbulos atuam na movimentação celular, bem como está envolvido em transporte intracelular. Células migratórias, apresentam centro de organização dos microtúbulos polarizados, e simétricos (38-40). Interessantemente, análises *in sílico* de expressão dos genes envolvidos com a tubulina em banco de dados públicos do TCGA, demonstraram uma correlação positiva com *LOXL3* no subtipo mesenquimal, diferente dos outros subtipos, sugerindo um possível envolvimento de LOXL3 com citoesqueleto.

Para aprofundar o entendimento da expressão da família LOX em astrocitomas, foram realizadas análises de expressão em diferentes graus de astrocitoma, com estratificação por IDH mutante e selvagem, descrito na Publicação 2. Conforme previsto e em concordância com dados anteriores, notamos um aumento na expressão dos membros da família LOX nas amostras de astrocitoma em comparação com as não neoplásicas. O aumento da expressão acompanhou a progressão da malignidade, atingindo seu ponto mais alto em GBM. Resultados similares foram observados em outros tumores, onde a expressão da família LOX foi associado com progressão tumoral (1, 2, 25, 42-47). Além disso, foram observadas expressões diferenciais significativas de *LOX*, *LOXL1* e *LOXL3* em ambas as comparações LGG-IDH-mut vs LGG-IDH-wt e LGG-IDH-wt vs GBM. Análises proteicas através de imuno-histoquímica também apresentaram aumento progressivo da expressão em LGG-IDH-mutLGG-IDH-wt, GBM-IDH-mut e GBM IDH-wt, corroborando com as análises *in silico*. Estudos anteriores do nosso laboratório demonstraram a correlação da expressão de *LOX* com mutação em *IDH1* nos graus 2 ao 4 dos astrocitomas difusos (48).

Curiosamente, em pacientes com LGG, alta expressão de *LOX* e *LOXL1* correlacionou-se com um prognóstico desfavorável em termos de sobrevida livre de doença, ao contrário dos casos com baixa expressão desses genes. Em GBM, a hipoexpressão de

LOXL1 foi associada a uma prolongada sobrevida geral dos pacientes. Semelhantemente, estudos anteriores descreveram o envolvimento de *LOXL1* na promoção e progressão tumor em gliomagenesis (49), bem como em câncer de colorretal (50) e hepático (51). O papel de LOX em tumores já é amplamente discutido (52).

Análises *in silico* revelaram correlações significativas entre cada membro da família LOX, considerando a estratificação do grau de malignidade e o status mutacional de *IDH1*. *LOXL1* mostrou correlação com genes em tumores de baixo grau com mutação de *IDH1*. *LOXL3* teve correlações mais evidentes em tumores de baixo grau mais agressivos com *IDH*selvagem, enquanto *LOX* se correlacionou mais fortemente em GBM. Esses resultados indicam que a expressão da família LOX pode ser influenciada pelo perfil genético do tumor, potencialmente afetando a rigidez da matriz e a progressão tumoral.

Observando a alta expressão de *LOXL3* em GBM e sua possível participação na progressão maligna de astrocitomas, foi realizado no estudo 3, um silenciamento permanente de *LOXL3* usando CRISPR-Cas9 em linhagens de GBM humano, U87MG (TP53-wt) e U251 (TP53-mut). Interessantemente, observações similares as células silenciadas transitoriamente, quanto ao aumento da superfície da área celular, foram encontradas nas células nocauteadas para *LOXL3* em ambas as linhagens. Além disso, ensaios *in vitro* com as células nocauteadas para *LOXL3* apresentaram uma diminuição na viabilidade celular em ambas as linhagens, principalmente nos clones com maior eficiência de silenciamento.

A análise de enriquecimento de genes diferencialmente expressos do RNAseq nas células nocauteadas em comparação com os controles revelou uma diminuição da via associada à acetilação de tubulina na linhagem U87MG. De fato, uma forte diminuição dos níveis de expressão proteica de α-tubulina acetilada nas células nocauteadas para *LOXL3* nas células U87MG e U251 foram observadas. Acetilação é associada a flexibilidade e estabilidade do microtúbulo (53), e pode influenciar na ligação de proteínas denominadas proteínas de ligação ao microtúbulo (MAPs) (54). Genes que codificam algumas MAPs como *MAPT* e *FRY*, foram encontradas reguladas negativamente nas células com nocaute de *LOXL3* na linhagem U87MG, proteínas estas, relacionadas com o aumento da flexibilidade e polimerização do microtúbulo (55, 56). Além disso, foi observado um aumento da expressão dos genes *ATAT1* e *HDAC5* linhagem U87MG, enquanto que na U251 foi observado aumento de expressão somente de *HDAC5*. A acetilação na α-tubulina é promovida por pela α-TAT1, codificada pelo gene *ATAT1*, enquanto que a desacetilação é realizada pela HDAC5/6 e sirtuína 2 (57).

A acetilação dos microtúbulos também pode influenciar na divisão e ciclo celular (58). Um atraso no ciclo celular, com um aumento da população nas fases G2/M e G1 das células nocauteadas para *LOXL3* na linhagem U87MG, e nas fases G2/M e S nas células com nocaute de *LOXL3* na linhagem U251. Genes associados com a formação do fuso mitótico foram observadas reguladas negativamente, como o próprio *FRY*, relacionado com acetilação em microtúbulos no fuso mitótico (56). *CDC14B*, uma fosfatase, que promove a estabilidade do microtúbulo, e progressão no ciclo celular na anáfase (59). Enquanto que na linhagem U251, genes que codificam para proteínas do centrossomo, como *CEP72* e *CEP85*, foram encontrados com baixa expressão. Amplificação desse genes estão relacionado com acetilação do microtúbulo (60). Além disso, o gene que codifica ciclina E (*CCNE1*), foi encontrado regulado negativamente, podendo explicar a inibição da entrada na fase S (61). Outros genes associados a ciclo celular e reparo de DNA também foram observados regulados negativamente. O gene *MAD1L1*, que codifica para MAD1 envolvida no ponto de verificação da montagem do fuso mitótico, processo conhecido como SAC (*spindle assembly checkpoint*) foi observado com alta expressão nas células nocauteadas para LOXL3 em ambas as linhagens, U87MG e U251 (62). SAC é ativado durante a transição da metáfase para a anáfase (63), e a acetilação dos microtúbulos varia ao longo das fases da mitose, sendo evidente na metáfase e anáfase (64). Alterações significativas foram observadas quanto a quantidade e estrutura da acetilação dos microtúbulos durante essas fases. Além disso, o nocaute de *LOXL3* no clone 1 de U251 resultou em uma mitose multipolar, associada a uma falha ou superativação do SAC de maneira independente de p53 (65). Análises de morfologia nuclear foram realizados, e um aumento de núcleos caracterizados a mitose catastrófica e senescência foram atribuídos a células nocaute de *LOXL3* nas linhagens U87MG e U251, respectivamente. O silenciamento de *LOXL3* resultou em mitoses aberrantes associadas à catástrofe mitótica em células de melanoma (7).

Adicionalmente, um aumento significativo da morte celular na fase inicial com ou sem tratamento com TMZ, similarmente ao descrito no artigo 1. Já na linhagem U251, as células com nocaute de *LOXL3* apresentaram um aumento da morte na fase tardia sem tratamento com TMZ. A mitose catastrófica pode levar a células tetraploides, resultando em células com parada na fase G1 do ciclo celular, promovendo a morte celular dependente de p53, ou podem prosseguir para senescência (66, 67). Curiosamente, efeitos semelhantes são observados no uso de terapia com drogas anti-microtúbulos (68, 69). De fato, foi observado um aumento da expressão de genes relacionados à morte celular dependente de p53 em células U87MG,

enquanto que a U251 apresentou um aumento na expressão de genes relacionados à senescência.

A acetilação de microtúbulos influencia diretamente o aumento da adesão focal e da migração celular (70). O nocaute de *LOXL3* promoveu uma diminuição da adesão celular apenas em células U87MG, principalmente no clone 1. Estes dados são contrários aos observados no silenciamento transitório de LOXL3 por siRNA (publicação 1). No entanto, resultados obtidos no artigo 2 mostraram forte correlação da expressão de *LOXL3* e genes que codificam proteínas da MEC. A diferença no efeito da adesão celular causado pelo silenciamento transitório e permanente pode ser explicado devido a um efeito compensatório da ausência de LOXL3, uma vez que há um aumento substancial da expressão dos genes que codificam proteínas relacionadas a MEC e de membros da família LOX nas células silenciadas transitoriamente. Nas células com nocaute de *LOXL3* não foram observadas alterações na expressão de genes dos outros membros da família LOX bem como relacionados a MEC.

Entre os genes analisados, a expressão de LOXL3 correlacionou-se com vários genes analisados nos conjuntos de dados TCGA-RNAseq em TP53-mut, TP53-wt e no grupo total. Os genes apresentaram uma correlação mais forte com LOXL3 em TP53-mut. A análise de Kaplan-Meier mostrou que a regulação negativa e concomitante de *LOXL3* e *CCNE1* resultou em um aumento do tempo de sobrevida dos pacientes em casos com mutação de *TP53*. Na publicação de número 1 foi demonstrado que níveis de expressão menores de *LOXL3* levou a uma melhoria nas taxas de sobrevida. A maioria dos pacientes com amplificação de *CCNE1* apresentam mutação concomitante em *TP53*, e esse fenótipo contribui para a resistência à quimioterapia. Curiosamente, a amplificação de *CCNE1* e a mutação em *TP53* apresentaram um prognóstico ruim em tumores sólidos. Um ensaio clínico (NCT03253679), na fase 1, mostrou que a amplificação de *CCNE1* estava associada a mutações frequentes de *TP53* e um desfecho clínico agressivo. No esboço do desenvolvimento terapêutico para tumores com amplificação de *CCNE1*, a superexpressão de ciclina E devido à amplificação de *CCNE1* e concomitante mutação em *TP53* promove a progressão da fase G1 para a fase S, proporcionando possíveis alvos terapêuticos para quimioterapia, terapia direcionada e radiação para potencializar a catástrofe mitótica e a apoptose (71).

8 CONCLUSÃO

A família lisil oxidase está fortemente correlacionada com a progressão tumoral em astrocitomas e GBM. *LOXL1*, *LOXL3* e *LOX* demonstraram uma correlação progressiva com genes associados à rigidez da matriz, dependendo do grau de malignidade e da estratificação de *IDH1*. A expressão de *LOXL1* influenciou o prognóstico em tumores astrocíticos de baixo grau e GBM. O silenciamento transitório e permanente de *LOXL3*, o membro menos estudado da família LOX, resultou em diminuição da viabilidade celular e aumento da morte celular, independentemente do tratamento com TMZ. Além disso, o silenciamento alterou a morfologia celular, aumentando a área da superfície celular. Análises *in silico* e proteica revelaram que o silenciamento provocou mudanças no perfil de acetilação de tubulina, levando a uma redução na migração e/ou invasão celular, além de atraso no ciclo celular. Além disso, interessantemente, coexpressão de CCNE1 e *LOXL3* impactou a sobrevida em casos de GBM com *TP53* mutado. Esses resultados destacam a necessidade de estudos mais aprofundados sobre a família LOX, considerando alterações moleculares, para compreender melhor a progressão tumoral e a gliomagênese. Adicionalmente, os resultados do silenciamento indicam LOXL3 como um potencial alvo terapêutico, especialmente em combinação com ciclina E para casos de GBM com mutação em TP53.

9 REFERÊNCIAS (introdução e discussão)

1. Nishioka T, Eustace A, West C. Lysyl oxidase: from basic science to future cancer treatment. Cell Struct Funct. 2012;37(1):75-80.
2. Barker HE, Cox TR, Erler JT. The rationale for targeting the LOX family in cancer. Nat Rev Cancer. 2012;12(8):540-52.
3. Lee JE, Kim Y. A tissue-specific variant of the human lysyl oxidase-like protein 3 (LOXL3) functions as an amine oxidase with substrate specificity. J Biol Chem. 2006;281(49):37282-90.
4. Mäki JM, Kivirikko KI. Cloning and characterization of a fourth human lysyl oxidase isoenzyme. Biochem J. 2001;355(Pt 2):381-7.
5. Kraft-Sheleg O, Zaffryar-Eilot S, Genin O, Yaseen W, Soueid-Baumgarten S, Kessler O, et al. Localized LoxL3-Dependent Fibronectin Oxidation Regulates Myofiber Stretch and Integrin-Mediated Adhesion. Dev Cell. 2016;36(5):550-61.
6. Peinado H, del Carmen Iglesias-de la Cruz M, Olmeda D, Csiszar K, Fong KSK, Vega S, et al. A molecular role for lysyl oxidase-like 2 enzyme in Snail regulation and tumor progression. EMBO J. 242005. p. 3446-58.
7. Santamaria PG, Floristan A, Fontanals-Cirera B, Vazquez-Naharro A, Santos V, Morales S, et al. Lysyl oxidase-like 3 is required for melanoma cell survival by maintaining genomic stability. Cell Death Differ. 2018;25(5):935-50.
8. Ma L, Huang C, Wang XJ, Xin DE, Wang LS, Zou QLC, et al. Lysyl Oxidase 3 Is a Dual-Specificity Enzyme Involved in STAT3 Deacetylation and Deacetylimination Modulation. Molecular Cell. 2017;65(2):296-309.
9. Kasashima H, Yashiro M, Okuno T, Miki Y, Kitayama K, Masuda G, et al. Significance of the Lysyl Oxidase Members Lysyl Oxidase Like 1, 3, and 4 in Gastric Cancer. Digestion. 2018;98(4):238-48.
10. Zhou L, Chen B, Hua X, Zhou P, Guo L, Peng Y, et al. Effect of newly identified hTERT-interacting proteins on telomerase activity. Acta Biochim Biophys Sin (Shanghai). 2013;45(8):674-82.
11. Laurentino Td, S., Soares Rd, S., Marie SKN, Oba-Shinjo SM. LOXL3 Function Beyond Amino Oxidase and Role in Pathologies, Including Cancer. Int J Mol Sci. 2019;20(14):3587.
12. Ostrom QT, Price M, Neff C, Cioffi G, Waite KA, Kruchko C, et al. CBTRUS Statistical Report: Primary Brain and Other Central Nervous System Tumors Diagnosed in the United States in 2016-2020. Neuro-oncology. 2023;25(Supplement_4).
13. Weller M, Wick W, Aldape K, Brada M, Berger M, Pfister SM, et al. Glioma. Nat Rev Dis Primers. 2015;1:15017.
14. Kaminska B, Czapski B, Guzik R, Król SK, Gielniewski B. Consequences of IDH1/2 Mutations in Gliomas and an Assessment of Inhibitors Targeting Mutated IDH Proteins. Molecules. 2019;24(5).
15. Gessler F, Zappi J, Konczalla J, Bernstock JD, Forster MT, Wagner M, et al. Secondary Glioblastoma: Molecular and Clinical Factors That Affect Outcome After Malignant Progression of a Lower Grade Tumor. World Neurosurg. 2017;102:49-55.
16. Parsons DW, Jones S, Zhang X, Lin JC, Leary RJ, Angenendt P, et al. An integrated genomic analysis of human glioblastoma multiforme. Science. 2008;321(5897):1807-12.
17. Louis DN, Perry A, Wesseling P, Brat DJ, Cree IA, Figarella-Branger D, et al. The 2021 WHO Classification of Tumors of the Central Nervous System: a summary. Neuro-oncology. 2021;23(8):1231-51.
18. Molenaar RJ, Maciejewski JP, Wilmink JW, van Noorden CJF. Wild-type and mutated IDH1/2 enzymes and therapy responses. Oncogene. 2018;37(15):1949-60.
19. Lee CY. Strategies of temozolomide in future glioblastoma treatment. Onco Targets Ther. 2017;10:265-70.
20. Ostrom TQ, Cioffi G, Waite K, Kruchko C, Barnholtz-Sloan SJ. CBTRUS Statistical Report: Primary Brain and Other Central Nervous System Tumors Diagnosed in the United States in 2014–2018. Neuro-Oncology. 2021;Volume 23:1-105.

21. Verhaak RG, Hoadley KA, Purdom E, Wang V, Qi Y, Wilkerson MD, et al. An integrated genomic analysis identifies clinically relevant subtypes of glioblastoma characterized by abnormalities in PDGFRA, IDH1, EGFR and NF1. Cancer Cell. 2010;17(1):98-110.
22. Wang Q, Hu B, Hu X, Kim H, Squatrito M, Scarpace L, et al. Tumor Evolution of Glioma-Intrinsic Gene Expression Subtypes Associates with Immunological Changes in the Microenvironment. Cancer Cell. 2017;32(1):42-56.e6.
23. Sidaway P. CNS cancer: Glioblastoma subtypes revisited. Nat Rev Clin Oncol. 2017;14(10):587.
24. Schütze F, Röhrig F, Vorlová S, Gätzner S, Kuhn A, Ergün S, et al. Inhibition of Lysyl Oxidases Improves Drug Diffusion and Increases Efficacy of Cytotoxic Treatment in 3D Tumor Models. Scientific Reports. 2015;5:17576.
25. Johnston KA, Lopez KM. Lysyl oxidase in cancer inhibition and metastasis. Cancer Lett. 2018;417:174-81.
26. Trackman PC. Lysyl Oxidase Isoforms and Potential Therapeutic Opportunities for Fibrosis and Cancer. Expert Opin Ther Targets. 2016;20(8):935-45.
27. Yang J, Savvatis K, Kang JS, Fan P, Zhong H, Schwartz K, et al. Targeting LOXL2 for cardiac interstitial fibrosis and heart failure treatment. Nat Commun. 2016;7:13710.
28. Eiseler T, Köhler C, Nimmagadda SC, Jamali A, Funk N, Joodi G, et al. Protein Kinase D1 Mediates Anchorage-dependent and -independent Growth of Tumor Cells via the Zinc Finger Transcription Factor Snail1*. J Biol Chem. 2012;287(39):32367-80.
29. Peinado H, Del Carmen Iglesias-de la Cruz M, Olmeda D, Csiszar K, Fong KS, Vega S, et al. A molecular role for lysyl oxidase-like 2 enzyme in snail regulation and tumor progression. Embo j. 2005;24(19):3446-58.
30. Vázquez-Naharro A, Bustos-Tauler J, Floristán A, Yuste L, Oltra SS, Vinyals A, et al. Loxl3 Promotes Melanoma Progression and Dissemination Influencing Cell Plasticity and Survival. Cancers. 2022;14(5).
31. Sebban S, Davidson B, Reich R. Lysyl oxidase-like 4 is alternatively spliced in an anatomic site-specific manner in tumors involving the serosal cavities. Virchows Archiv. 2009;454(1):71-9.
32. Dufresne J, Bowden P, Thavarajah T, Florentinus-Mefailoski A, Chen ZZ, Tucholska M, et al. The plasma peptides of ovarian cancer. Clin Proteomics. 2018;15:41.
33. Tadmor T, Bejar J, Attias D, Mischenko E, Sabo E, Neufeld G, et al. The expression of lysyl-oxidase gene family members in myeloproliferative neoplasms. Am J Hematol. 2013;88(5):355-8.
34. Barbazan J, Muinelo-Romay L, Vieito M, Candamio S, Diaz-Lopez A, Cano A, et al. A multimarker panel for circulating tumor cells detection predicts patient outcome and therapy response in metastatic colorectal cancer. International Journal of Cancer. 2014;135(11):2633-43.
35. Insua YV, De la Camara J, Vazquez EB, Fernandez A, Rivera FV, Silva MJV, et al. Predicting Outcome and Therapy Response in mCRC Patients Using an Indirect Method for CTCs Detection by a Multigene Expression Panel: A Multicentric Prospective Validation Study. International Journal of Molecular Sciences. 2017;18(6).
36. Marie SK, Okamoto OK, Uno M, Hasegawa AP, Oba-Shinjo SM, Cohen T, et al. Maternal embryonic leucine zipper kinase transcript abundance correlates with malignancy grade in human astrocytomas. Int J Cancer. 2008;122(4):807-15.
37. Ye M, Y. S, Pan S, Chu M, Wang Z, Zhu X. Evolving roles of lysyl oxidase family in tumorigenesis and cancer therapy. Pharmacology & therapeutics. 2020;215.
38. JCM M, BI S, A A. Generation and regulation of microtubule network asymmetry to drive cell polarity. Current opinion in cell biology. 2020;62.
39. Garcin C, Straube A. Microtubules in cell migration. Essays in biochemistry. 2019;63(5).
40. Etienne-Manneville S. Polarity proteins in migration and invasion. Oncogene. 2008;27(55).
41. Ramão A, Gimenez M, Laure HJ, Izumi C, Vida RC, Oba-Shinjo S, et al. Changes in the expression of proteins associated with aerobic glycolysis and cell migration are involved in tumorigenic ability of two glioma cell lines. Proteome science. 2012;10(1).
42. Wang TH, Hsia SM, Shieh TM. Lysyl Oxidase and the Tumor Microenvironment. International journal of molecular sciences. 2016;18(1).
43. Tenti P, Vannucci L. Lysyl oxidases: linking structures and immunity in the tumor microenvironment. Cancer immunology, immunotherapy : CII. 2020;69(2).

44. Saatci O, Kaymak A, Raza U, Ersan PG, Akbulut O, Banister CE, et al. Targeting lysyl oxidase (LOX) overcomes chemotherapy resistance in triple negative breast cancer. Nature communications. 2020;11(1).
45. Payne SL, Hendrix MJ, Kirschmann DA. Paradoxical roles for lysyl oxidases in cancer--a prospect. Journal of cellular biochemistry. 2007;101(6).
46. Kirschmann DA, Seftor EA, Fong SFT, Nieva DRC, Sullivan CM, Edwards EM, et al. A molecular role for lysyl oxidase in breast cancer invasion. Cancer Research. 2002;62(15):4478-83.
47. Erler JT, Bennewith KL, Cox TR, Lang G, Bird D, Koong A, et al. Hypoxia-Induced Lysyl Oxidase Is a Critical Mediator of Bone Marrow Cell Recruitment to Form the Premetastatic Niche. Cancer Cell. 2009;15(1):35-44.
48. da Silva R, Uno M, Nagahashi Marie SK, Oba-Shinjo SM. LOX Expression and Functional Analysis in Astrocytomas and Impact of IDH1 Mutation. Plos One. 2015;10(3).
49. Yu H, Ding J, Zhu H, Jing Y, Zhou H, Tian H, et al. LOXL1 confers antiapoptosis and promotes gliomagenesis through stabilizing BAG2. Cell death and differentiation. 2020.
50. Hu L, Wang J, Wang Y, Wu L, Wu C, Mao B, et al. LOXL1 modulates the malignant progression of colorectal cancer by inhibiting the transcriptional activity of YAP. Cell communication and signaling : CCS. 2020;18(1).
51. Yuan R, Li Y, Yang B, Jin Z, Xu J, Shao Z, et al. LOXL1 exerts oncogenesis and stimulates angiogenesis through the LOXL1-FBLN5/αvβ3 integrin/FAK-MAPK axis in ICC. Molecular therapy Nucleic acids. 2021;23.
52. Liburkin-Dan T, Toledano S, Neufeld G. Lysyl Oxidase Family Enzymes and Their Role in Tumor Progression. International journal of molecular sciences. 2022;23(11).
53. Xu Z, Schaedel L, Portran D, Aguilar A, Gaillard J, Marinkovich MP, et al. Microtubules acquire resistance from mechanical breakage through intralumenal acetylation. Science (New York, NY). 2017;356(6335).
54. Carmona B, Marinho HS, Matos CL, Nolasco S, Soares H. Tubulin Post-Translational Modifications: The Elusive Roles of Acetylation. Biology. 2023;12(4).
55. Kadavath H, Hofele RV, Biernat J, Kumar S, Tepper K, Urlaub H, et al. Tau stabilizes microtubules by binding at the interface between tubulin heterodimers. Proceedings of the National Academy of Sciences of the United States of America. 2015;112(24).
56. Nagai T, Ikeda M, Chiba S, Kanno S, Mizuno K. Furry promotes acetylation of microtubules in the mitotic spindle by inhibition of SIRT2 tubulin deacetylase. Journal of cell science. 2013;126(Pt 19).
57. Song Y, Brady ST. Post-translational modifications of tubulin: pathways to functional diversity of microtubules. Trends in cell biology. 2015;25(3).
58. Eshun-Wilson L, Zhang R, Portran D, Nachury MV, Toso DB, Löhr T, et al. Effects of α-tubulin acetylation on microtubule structure and stability. Proceedings of the National Academy of Sciences of the United States of America. 2019;116(21).
59. Cho HP, Liu Y, Gomez M, Dunlap J, Tyers M, Wang Y. The dual-specificity phosphatase CDC14B bundles and stabilizes microtubules. Molecular and cellular biology. 2005;25(11).
60. Monteiro P, Yeon B, Wallis SS, Godinho SA. Centrosome amplification fine tunes tubulin acetylation to differentially control intracellular organization. The EMBO journal. 2023;42(16).
61. Johnson A, Skotheim JM. Start and the restriction point. Current opinion in cell biology. 2013;25(6).
62. Lara-Gonzalez P, Pines J, Desai A. Spindle assembly checkpoint activation and silencing at kinetochores. Seminars in cell & developmental biology. 2021;117.
63. Lampert F, Westermann S. A blueprint for kinetochores - new insights into the molecular mechanics of cell division. Nature reviews Molecular cell biology. 2011;12(7).
64. Tan HF, Tan SM. The focal adhesion protein kindlin-2 controls mitotic spindle assembly by inhibiting histone deacetylase 6 and maintaining α-tubulin acetylation. The Journal of biological chemistry. 2020;295(18).
65. Brito DA, Rieder CL. Mitotic checkpoint slippage in humans occurs via cyclin B destruction in the presence of an active checkpoint. Current biology : CB. 2006;16(12).

66. Casenghi M, Mangiacasale R, Tuynder M, Caillet-Fauquet P, Elhajouji A, Lavia P, et al. p53-independent apoptosis and p53-dependent block of DNA rereplication following mitotic spindle inhibition in human cells. Experimental cell research. 1999;250(2).
67. Vakifahmetoglu H, Olsson M, Zhivotovsky B. Death through a tragedy: mitotic catastrophe. Cell death and differentiation. 2008;15(7).
68. Cheng B, Crasta K. Consequences of mitotic slippage for antimicrotubule drug therapy. Endocrine-related cancer. 2017;24(9).
69. Marxer M, Ma HT, Man WY, Poon RY. p53 deficiency enhances mitotic arrest and slippage induced by pharmacological inhibition of Aurora kinases. Oncogene. 2014;33(27).
70. Bance B, Seetharaman S, Leduc C, Boëda B, Etienne-Manneville S. Microtubule acetylation but not detyrosination promotes focal adhesion dynamics and astrocyte migration. Journal of cell science. 2019;132(7).
71. Yao S, Meric-Bernstam F, Hong D, Janku F, Naing A, Piha-Paul SA, et al. Clinical characteristics and outcomes of phase I cancer patients with CCNE1 amplification: MD Anderson experiences. Scientific reports. 2022;12(1).